Numerical Simulations Concerning the Propagation of Protostellar Jets

A thesis submitted for the degree of
Doctor of Philosophy

by

Anthony Moraghan

School of Physics

University of Dublin
Trinity College
Dublin 2
Ireland

March 2008

Dedicated to my parents,
Noreen and Freddie

Acknowledgements

Firstly I am very grateful to Prof. Mark Bailey for selecting me as a PhD student and thus allowing me to come and experience the excellent, warm and friendly family-like research institution of Armagh Observatory. Though forever busy keeping the Observatory open and running smoothly, he was always available to provide assistance and support whenever I needed it.

I wish to thank my primary supervisor, Prof. Michael Smith, for his guidance, support, encouragement, long working hours and easy-going attitude during my PhD. I have learned a lot and definitely would never have made it this far without him. The cooking wasn't too bad either!

I also wish to thank my secondary supervisor Prof. Tom Ray in DIAS for his help and support over the last few years.

I am very grateful to Armagh Observatory and DIAS for bestowing me the honour of holding the first Lindsay Scholarship.

I acknowledge Prof. Lunney, Dr. McMurry, Dr. Espey, Dr. Finch and John Kelly for their assistance down in the School of Physics and the School in general for additional financial support.

Very special thanks go to the entire international community of staff and students at Armagh Observatory, both past and present, who have influenced my life, some more than others, but still in some way nonetheless. It is only fair to proceed in alphabetical order so as to not to hold one persons friendship over another. Thanks Abhishek, Aileen, Alex, Alison, Amir, Ana, Barry, Bebe, Bernard, Caroline, Chia-Hsien, Chris, Colin, David A, David M, David P-S, Dipanker, Eamon, Eoghan, Gavin, Geoff, Georgi, Gerry, Ignacio, Igor, John B, John McF, Jonathan, Jorick, Lawarence, Margaret, Martin, Miruna, Natalie, Olena, Pat, Prakash, Ram, Rhona, Shane, Simon, Sri, Timur, Toby, Tolis, Tony, Tom, and Youra. I have made some very good friends in that list and hope that we will be able to keep in touch in the future.

I was lucky enough to spend a short time at other institutions and wish to thank the people there. At DIAS there was Andy, Eileen, Emma, Deirdre, Gareth, Fabio, Jonathan, Jóse, Paul and Philippe. At CAPS in Canterbury there was Dirk and Jonathan.

My only regret is that my time at Armagh went by so fast. One thing is for certain, whatever the future holds, I will always have fond memories of Armagh Observatory.

Summary

A protostellar jet is a highly supersonic stream of material which heralds the birth of a star while it is still deeply embedded, out-of-sight within a molecular cloud core. The jet entrains and accelerates ambient cloud material to form an outflow which emits profusely in molecular lines. These regions of emission were first detected in the 1950s and catalogued as Herbig-Haro objects. Today, the study of jets from young stars is a maturing subject with modern detectors regularly revealing magnificent manifestations of jets and bipolar outflows.

Observational and numerical studies have revealed that jets and outflows play a crucial role in the star formation process. In order to regulate the rotating collapse of a star forming cloud into a young star, an outflow of material is required to expel excess angular momentum from the system. The outflow may also play a double role of controlling star formation rates on the larger molecular cloud scales through the supply of turbulent energy.

Numerical simulations combine the physics of hydrodynamics, magnetohydrodynamics and molecular chemistry and can effectively create and evolve protostellar jets and outflows over thousands of years compared to the brief snapshots in time provided by observations.

The properties of bipolar outflows depend on the nature of the jet and the structure of the ambient environment. In this thesis we perform a study of both aspects via numerical simulations using the prominent fixed–grid Eulerian astrophysical fluid dynamics code, ZEUS-3D, which has been expanded upon to incorporate robust molecular cooling and chemistry routines. Links to observations are made through the plotting of mass-velocity relationships from our simulated data.

Firstly, the scene will be set through a brief review of the physics and principles behind the star formation process and the protostellar jet phenomenon, before moving on to a description of numerical aspects, including the general operation of hydrodynamical codes and the algorithms employed by ZEUS-3D for the investigations to follow.

We then proceed to look at the nature of the jet and ask if the outflow properties may be related to the speed of the jets. To test this, we build upon previous studies by injecting molecular and atomic jets with a wide range of speeds, between 50 and 300 km s^{-1}, into both molecular and atomic media. We show that the high collimation of outflows driven by molecular jets holds for all jet speeds. At the higher speeds, we find that the jet Mach number is the critical parameter which determines the shape of the cavity and the cavity is filled with atomic gas. However, at low speeds the jet material is the key factor with atomic jets producing much wider cavities while molecular jets produce narrow cool molecular sheaths. A Mach disk is associated with the leading edge of the atomic simulations while oblique shocks, which refocus the jet, are found in molecular flows. By examining the mass spectra of these simulations, we generally find quite shallow relationships for all jet speeds (i.e. the γ index is typically 1–2). Steep molecular mass spectra are, however, associated with the atomic–jet/molecular–medium combination. We conclude that the properties of bipolar outflows possess signatures related to the jet speed but are probably more sensitive to other factors.

Finally, we investigate the ambient environment and progress from simulations which typically model only a uniform ambient medium by creating more realistic ambient environments for the jet to propagate through. Axisymmetric hydrodynamic simulations are are then performed by injecting continuous atomic jets into molecular media with density gradients (protostellar cores) and density discontinuities (thick swept-up sheets). Again, the approach is quantified using mass spectra for comparison with observationally determined values. We uncover a sequence from clump entrainment in the flanks to bow shock sweeping as the density profile steepens. We also find that the dense, highly supersonic outflows remain collimated but can become turbulent after passing through a shell. The mass spectra vary substantially in time, especially at radial speeds exceeding 15 km s^{-1}. The mass spectra also vary according to the conditions in that both envelope-type density distributions and the passage through dense sheets generate considerably steeper mass spectra than a uniform medium. The simulations suggest that observed outflows penetrate highly non-uniform media.

Overall, although we wish to learn about the forming protostar at the source, outflows are strongly influenced by their environment, rendering a precise interpretation quite difficult. However, the dynamical relationships uncovered here suggests that one can employ outflows to constrain the nature of both the protostar and the environment.

Contents

List of Tables

List of Figures

Publications

A list of publications resulting from work presented in this thesis is given below.

Refereed Publications

Moraghan, A. and Smith, M. D. and Rosen, A. Velocity study of axisymmetric protostellar jets with molecular cooling.
Monthly Notices of the Royal Astronomical Society, 2006, Volume 371, pp. 1448-1458
(Based on Chapter 3 of this thesis)

Moraghan, A. and Smith, M. D. and Rosen, A. The influence of the environment on the propagation of protostellar outflows.
Monthly Notices of the Royal Astronomical Society, 2008, Volume 386, pp. 2091-2100
(Based on Chapter 4 of this thesis)

In Preparation

Moraghan, A. and Smith, M. D. A new analysis of Spitzer IRAC data relating to protostellar outflows.

Chapter 1

Star Formation and Protostellar Jets: An introduction

1.1 Overview of star formation

This chapter will begin by briefly describing the processes involved during star formation with the view to identifying the conditions that lead to protostellar jets and outflows. Some observational examples of jets and outflows will be introduced before interpreting the physical principles at work there. As we shall see, protostellar jets and outflows are intrinsically linked to star formation and they have proved to be a valuable aid in understanding key stages of the star formation process.

Star formation is a very complex process, one which astronomers have worked towards understanding for centuries. Today, thanks to the combination of observations, theories and numerical simulations we have a broad understanding of the general overall process, yet there are still many questions in the fine details that need to be addressed.

It is human nature to bring order to chaos and hence Figure 1.1 is an attempt to simplify and divide the low-mass star formation process into seven distinct stages. (High mass stars with $M_\star > 8M_\odot$ are believed to form in a fundamentally different

manner, see Section1.5).

The initial stage is the Molecular Cloud, the reservoir containing all the raw material for the star, (Section 1.1.1). Turbulence disrupts the cloud into progressively smaller units. The smallest unit, the prestellar core, slowly contracts under its own gravity, (Section 1.1.2). Molecular chemistry is important to lower the thermal energy in the system. The buildup of material onto the central object is then carefully regulated by magnetic fields, differential rotation and protostellar outflows. If it were not for these mechanisms, the increase of angular momentum as the system contracts would reach too high a value for a compact central object to form, (Section 1.1.3 to 1.1.6). The final stage is a young star at the Zero Age Main Sequence stage where nuclear fusion ignites in its core, (Section 1.1.7).

The timescale from stage 1 to 7 is of the order of 10^7 years. This is only a fraction of a star's Main Sequence lifetime. A 1 $M_\odot$ star, like our Sun, is believed to have a Main Sequence lifetime of 10^{10} years.

1.1.1 Stage 1: Molecular Clouds

Stars form within massive clouds of gas and dust known as Molecular Clouds. Figure 1.2 displays a typical star forming cloud. Star formation is ongoing within the cloud but hidden from optical view by the presence of the dust and gas. The apparent cloud surface is only visible by the illumination of nearby stars which are actively 'eroding' the surface layers away by photo-ionisation.

Molecular clouds exist in a hierarchical manner ranging from the largest Giant Molecular Clouds with masses of the order $10^6 M_\odot$ and diameters up to $\sim$250 pc, down to the smallest star forming clouds popularly referred to as 'Bok Globules' (Bok & Reilly, 1947). Bok Globules have typical masses on the order of 0.1 – 50$M_\odot$, diameters a few tenths of a parsec and average temperatures about 10K (Nelson & Langer, 1999).

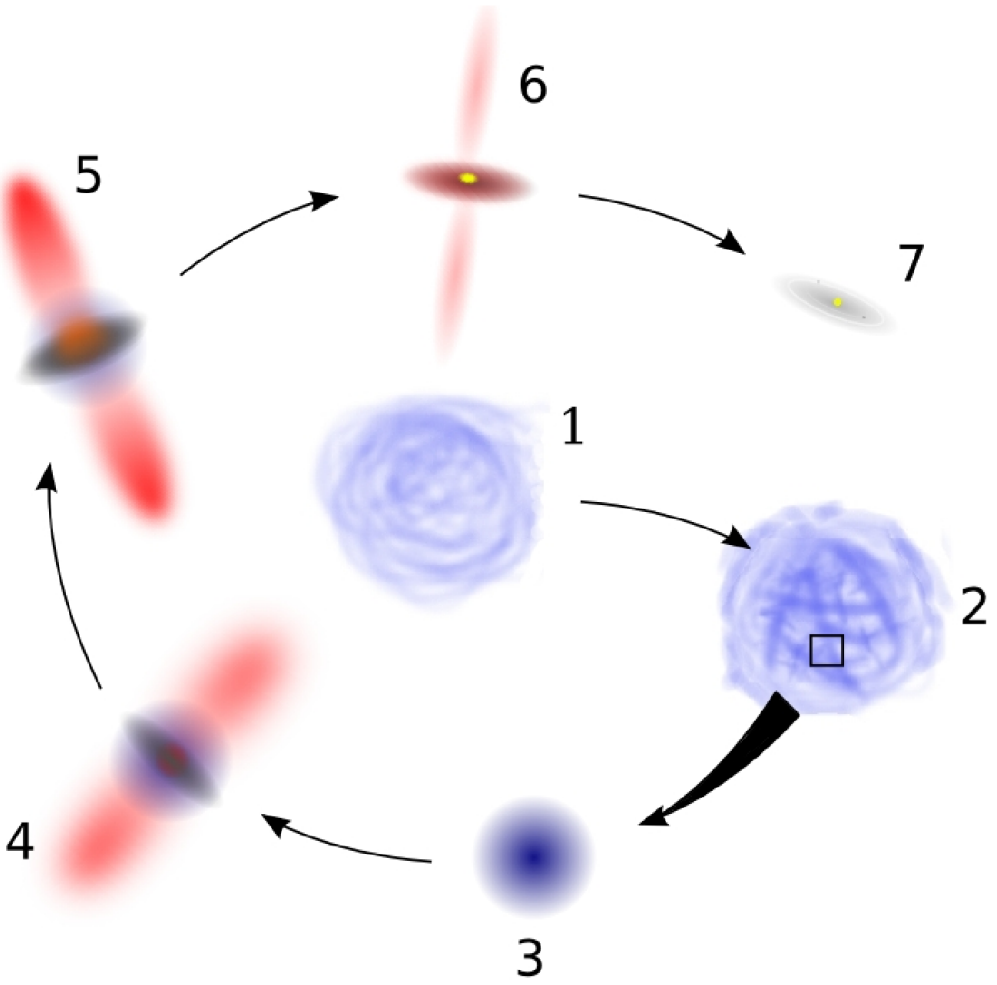

Figure 1.1: A pictorial representation of star formation divided into seven stages. 1. Molecular Cloud, 2. Fragmentation, 3. Prestellar core, 4. Class 0, 5. Class I, 6. Class II, 7. Class III.

The average density of molecular clouds is 10^{-18} kg m^{-3}. This is extremely tenuous compared to average density of the Earth's atmosphere ($\sim$1.2 kg m^{-3}), yet it is still denser than the average Interstellar Medium (ISM) by a factor of 1,000.

The development of sensitive infrared and mm detectors have revealed a host of complex molecular chemistry occurring in these regions. Although molecular hydrogen is the most abundant molecule, it is difficult to detect at the low temperatures at which molecular clouds typically exist. Molecular clouds are usually discovered at the 2.6 mm wavelength transitions of the $^{12}C^{16}O$ molecule (2.6 mm corresponds to a frequency of 115 GHz). As $^{12}C^{16}O$ is often optically thick, the $^{13}C^{16}O$ isomer is frequently used

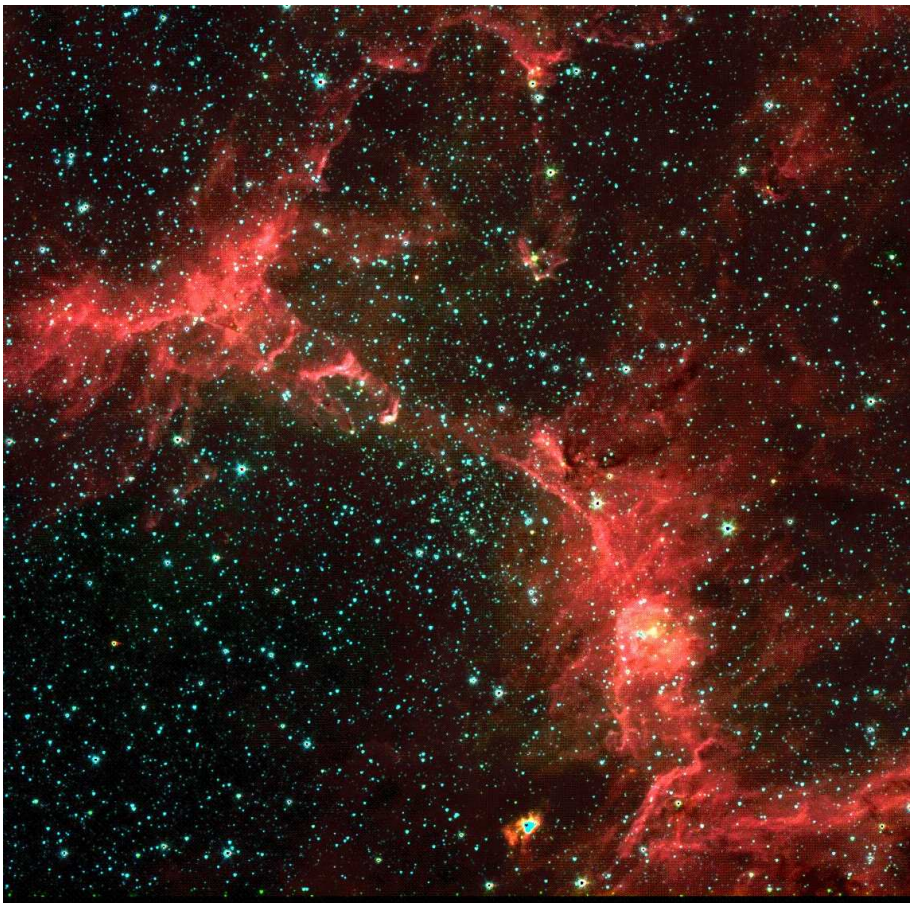

Figure 1.2: An infrared image of M16 molecular cloud or the 'Eagle Nebula'. The colour image was created by combining three publicly available IRAC band images from the Spitzer Space Telescope archive. 8.0μm emission is presented as red, 4.5μm as green and 3.6μm as blue.

instead to probe the cloud's interior. As is it less abundant and hence possesses a lower column density. To estimate the total masses of molecular clouds an abundance ratio fraction between H_2 and CO is typically assumed to be $\frac{[CO]}{[H_2]} \sim 10^{-4}$ (van Dishoeck et al., 1992). Combining observations of multiple molecules can provide a much fuller picture. For example, H_2 emission delineates high temperature regions such as locations of passing shocks while CO emission traces cool gas.

Intricate chemical reactions occur to create molecules of much greater complexity than H_2 and CO. To date, 140 different molecular species have been discovered[1]. The

[1]For an an updated database of new discoveries see `http://www.cdms.de`

longest chain molecule to be discovered is Cyanodecapentayne containing 13 atoms with the chemical composition $HC_{11}N$ (Bell et al., 1997). Some examples of the most recent discoveries are Acetamide, CH_3CONH_2, which possesses a peptide bond that occurs in amino acids (Hollis et al., 2006), Phosphaethyne, HCP (Agúndez et al., 2007), Methyltriacetylene, CH_3C_6H (Remijan et al., 2006) and Propylene, CH_2CHCH_3 (Marcelino et al., 2007).

Theoretical line profiles computed from atomic physics and laboratory experiments have aided astronomers in observing the complex configuration of lines which identify large molecules. The theoretical line profiles are becoming increasingly important as most astrophysical transitions are 'forbidden' (see Section 1.4.6) meaning they can occur but only at extremely low densities which can not be replicated in even the best artificial vacuum on Earth.

The reaction probability in such low densities is increased by 'dust' which behaves as a catalyst and consists of solid particles, mainly silicon and carbon compounds. In the early Universe (redshifts greater than 6) the majority of the dust is believed to have been formed from condensations of Type II Super Novae (SNe) explosions (Dwek et al., 2007). In the present day Universe, the main generator is believed to be the cool expanding atmospheres of asymptotic giant branch (AGB) stars. AGB stars can expel up to 80% of their initial mass during their lifetime at rates of up $10^{-4}M_{\odot}$ yr^{-1} (Lagadec et al., 2008).

Probing emission from dust grains in the millimeter and sub-millimeter wavelengths has been another method of mapping molecular cloud structure. As an example, Mitchell et al. (2001) obtained 850μm maps of the Orion B molecular cloud with the Sub-Millimeter Common-User Bolometer Array (SCUBA) instrument on the James Clerke Maxwell Telescope (JCMT). Studying the alignment or polarisation of the dust grains can also provide information about the global magnetic field structures of the clouds (Bethell et al., 2007).

An important condition for the formation of molecules is for sufficient shielding from

ionising photons to be present. Such ionising photons actively dissociate and destroy molecules and are usually emitted at ultraviolet wavelengths from nearby massive O and B stars. Molecular clouds are naturally self shielding by optical depth effects. The outer layers of the cloud, known as the Photo-Dissociation Region (PDR), progressively absorb the radiation from the highest dissociative extreme ultraviolet (EUV) radiation from hot O and B stars which creates a photoionised *atomic* hydrogen boundary layer. Slightly longer wavelength far-UV radiation with energy of 5–13.6 eV can propagate further into the cloud and dissociate molecular hydrogen, molecules such as CO, and can ionise carbon atoms. Further in, molecules are completely shielded and can survive (Smith, 2004).

How do molecular clouds form? Large scale galactic maps show that molecular clouds appear to be distributed along the spiral arms of the Galaxy. This supports the theory of differentially rotating density waves traveling through the galactic disk. The waves sweep up material, mainly atomic hydrogen, in the galactic disk where it is collected and compressed into molecular clouds.

How old are molecular clouds? A straightforward method is to assume the cloud is of similar age to the estimated ages of the young stellar populations within it. This would imply cloud age estimations of 10^7 years for GMC's and less for smaller clouds, matching the sound dynamical crossing time for clouds (Larson, 2003). Another method is by measuring molecular abundances and noting that molecules are not yet frozen onto dust grains. These studies suggest clouds are no older than 10^6 years (Larson, 2003). Overall the data suggests that clouds gather, immediately form a generation of stars, and then disperse.

1.1.2 Stage 2: Fragments

It is believed that turbulence disrupts Molecular Clouds into random filamentary structures, ultimately leading to the creation of prestellar cores on the smallest scales (Mac

Low & Klessen, 2004). Turbulence is a form of energy. It transports kinetic energy from a large scale to a small scale in three dimensions. Turbulence is supersonic due to the low sound speed (typically 0.2 kms^{-1} in dense clouds) with Mach numbers between 3–5 (Larson, 2003) (see Section 1.4.4).

Recent observations have revealed direct proof of supersonic turbulence in molecular clouds (Heyer & Brunt, 2007). This has previously been supported by 3D numerical simulations showing the importance of supersonic turbulence in the star formation process. For example, simulations performed by Pavlovski et al. (2002) and Pavlovski et al. (2006) found supersonic turbulence leads to the creation of filaments, clumps and diffuse regions in the cloud. Additionally the compressions and expansions also aid the formation and distribution of molecular species. The end result is that turbulence can sweep up the gas into thin flocculent layers leading to local density enhancements.

Supersonic turbulence is believed to arise from several sources such as galactic shear, gravitational instabilities, winds from massive O and B stars, protostellar outflows and supernova explosions (Mac Low & Klessen, 2004). Of these possibilities, it is supernovae which are believed to deliver the most sustainable amount of energy to the ISM in order to drive the turbulence. Based on the assumption of an estimated average of 50 supernovae per year in our Galaxy and a total energy output of 10^{51} erg per explosion, the energy dissipation rate, $\dot{e}$, is estimated to be $\dot{e} = 3 \times 10^{-26}$ erg cm^{-3} s^{-1} (Mac Low & Klessen, 2004). The next most abundant source of driving energy are the jets and outflows from within the molecular clouds. A current topic of study is the efficiency of protostellar outflows at transferring energy and momentum to the ambient medium (see Chapter 4). An estimate of the energy dissipation rate for jets and outflows is $\dot{e} = 2 \times 10^{-28}$ erg cm^{-3} s^{-1} (Mac Low & Klessen, 2004).

On the smallest scales, small dense gravitationally bound clumps of diameters a few tenths of a parsec may remain. Due to their high density, these clumps exist below the threshold to be disrupted by the cloud-wide effects of supersonic turbulence. Now a different physical process in the following stages will transform the clump into a young

star.

1.1.3 Stage 3: Prestellar Phase

How does a clump undergo a change in density of 18 orders of magnitude from a typical clump density of $10^{-17}\mathrm{kg\,m^{-3}}$ to $10^{3}\mathrm{kg\,m^{-3}}$ (the average density of the Sun) and decrease its spatial volume by a factor of roughly one million to become a star? Here, mathematical theories and computer models have played a crucial role in gaining an understanding of the complicated physics involved.

The most basic assumption is to imagine an undisturbed and stable spherical cloud of gas and dust of radius, R, and a uniform density. Any slight instability will disturb the equilibrium and lead to the onset of gravitational contraction. The instability may arise from factors such as ambipolar diffusion creating a slightly higher density in the cloud centre or an external impact increasing the external pressure on the cloud.

Collapsing material would move under the gravitational influence at the free-fall velocity, v_{ff}

$$v_{ff} \sim \sqrt{\frac{GM}{R}} \tag{1.1}$$

The dynamical timescale, or free-fall timescale, t_{ff}, would be similar to the sound speed, c_s, of the cloud thus the timescale for the collapse would be

$$t_{ff} \sim \frac{R}{c_s} \tag{1.2}$$

By replacing c_s with v_{ff} from Equation 1.1, we obtain the following expression for the free-fall timescale in terms of mass, M, and radius, R

$$t_{ff} \sim \frac{R^{\frac{3}{2}}}{\sqrt{GM}} \tag{1.3}$$

Of course, the above view is overly simplified. Many other factors should be taken

into account such as effects of cloud rotation, non-uniformities, magnetic fields and ambipolar diffusion.

As the clump slowly contracts under its own gravity, gravitational energy is converted to thermal energy which is freely radiated away into space by the dust and molecular material so that the collapsing fragment remains close to isothermal equilibrium with a radial density distribution of $\rho \propto \frac{1}{R^2}$. The core, having a higher density, has collapsed faster than the rest of the clump leaving a core-halo like structure. The core continues to contract slowly, trapping most of its own thermal energy. The surrounding material slowly infalls towards the higher density of the core.

When the central core density reaches a value about 10^{11}cm^{-3}, the core becomes opaque to the escaping radiation. The temperature begins to rise and thus so does the gas pressure. The core now behaves adiabatically. The gravitational contraction halts and is balanced by the thermal pressure when the core reaches a density between 10^{13}– 10^{14}cm^{-3}. This temporary stability is referred to as the 'first hydrostatic core'. The temperature continues to rise and when it reaches 2,000K, the molecular hydrogen dissociates. This allows for a second collapse phase as the dissociative cooling disturbs the core equilibrium. The temperature continues to rise slowly until all the hydrogen atoms become ionised. This occurs when the density reaches about 10^{23}cm^{-3} with a temperature of 10^4K. The contraction is halted again at what is known as the 'second hydrostatic core' with a mass of only $0.001\text{M}_\odot$ and radius of $1\text{R}_\odot$. The protostar has formed and will now gather 99% of its final mass from the surrounding envelope through accretion (Smith, 2004).

Rotation and magnetic fields will now begin to play an important role in further development. The rotation and angular momentum of the system tends to direct material into a thick disk perpendicular to the rotation axis, the 'accretion disk' (see Section 1.5). Magnetic fields will have influence over the entire system but will dominate in the densest regions, namely the protostar and the disk. It is now believed that

the magnetic field regulates the transfer of angular momentum in the disk. It channels material from the disk onto the star and also removes excess angular momentum by channeling material away from the system through open magnetic field lines along the rotation axis. This leads to the phenomenon of jets and outflows (see Section 1.7).

1.1.4 Stage 4: Class 0

The 'Class' definitions were an attempt to classify young protostars in terms of their evolutionary stage. Historically, Class I, II and III were first defined. The addition of a preceding 'Class 0' classification was proposed by Andre et al. (1993) when advances in sub-millimeter telescope technology allowed for the discovery of previously undetectable cool and low-luminosity cores. Class 0 protostars were initially only detectable at sub-millimeter wavelengths as the radiation from the central source is absorbed and attenuated by the large amount of dust and gas in the surrounding cloud. Today, some of the brighter Class 0 objects can be detected in Infrared by the Spitzer Space Telescope, such as the Class 0 object, IRAS 23011+6126 detectable at 3.5μm (Noriega-Crespo et al., 2005) (see Figure 1.3).

In order to classify such deeply embedded objects, the 'spectral energy distribution' (SED) is used. It is defined as the radiated power over a wavelength range, $\lambda \times S_\lambda$, the infrared wavelength range (2 – 20 μm) in this case. After the SED is obtained, the 'Bolometric temperature', T_{bol}, is measured. Bolometric temperature is defined by Chen et al. (1995) as the temperature of a blackbody having the same mean frequency as the observed continuum spectrum and where the 'mean frequency' is the ratio of the first and zeroth order moments of the source spectra. It can be quantified by the following equation,

$$T_{bol} = 1.25\frac{<\nu>}{100GHz} \tag{1.4}$$

where $<\nu>$ is the mean frequency of the observed spectrum (Smith, 2004). Figure 1.4 shows the progression of the SED through the four Class stages and a simplified

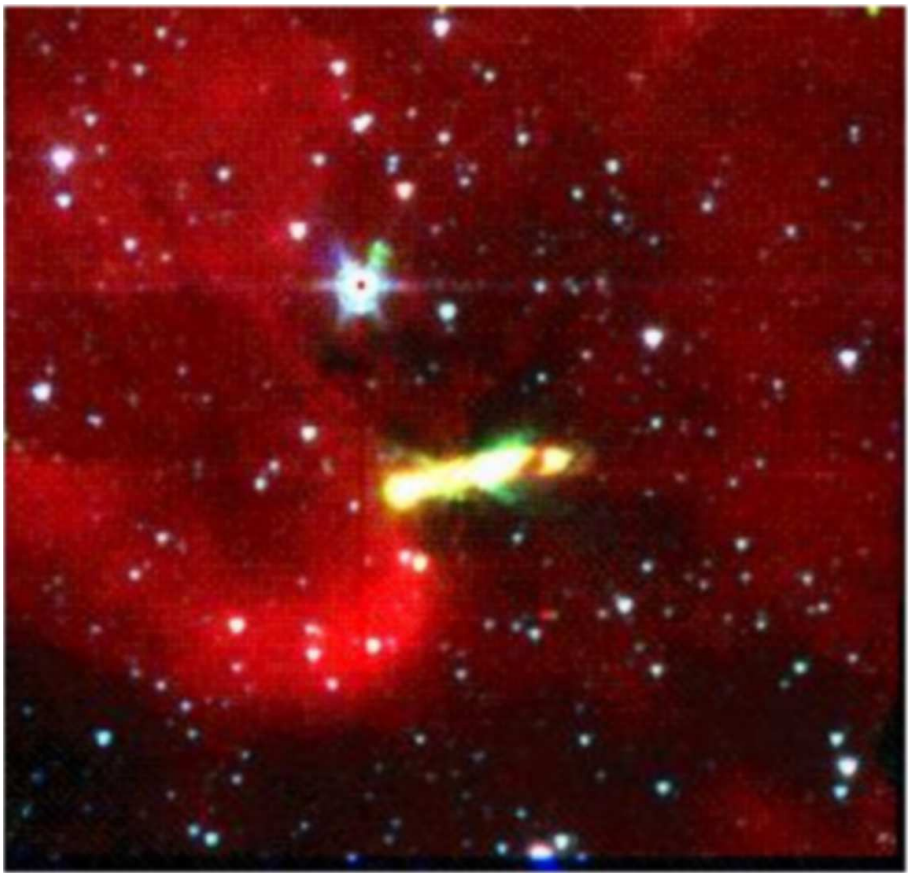

Figure 1.3: An infrared image of the IRAS 23011+6216 created by combining three publicly available IRAC band images from the Spitzer Space Telescope archive. 8μm emission is presented as red, 4.5μm as green and 5.8μm as blue. The 'green' nebulosity is believed to be from Carbon Monoxide molecules excited by outflows. The data was originally published by Noriega-Crespo et al. (2005).

illustration of how the system appears at each stage.

Using the SED method, Class 0 objects are defined as having a bolometric temperature less than 70K ($T_{bol} < 70K$). The low temperature is consistent with Class 0 systems possessing a greater amount of mass in their disks and envelopes than in the central protostar ($M_{env} > M_{star} + M_{disk}$). This explains the low T_{bol}, as the central core is deeply embedded and radiation is greatly redistributed through absorption and scattering before escaping.

Despite their extremely low luminosity, the presence of Class 0 objects is revealed by powerful bipolar outflows and dense molecular jets emanating from their vicinity.

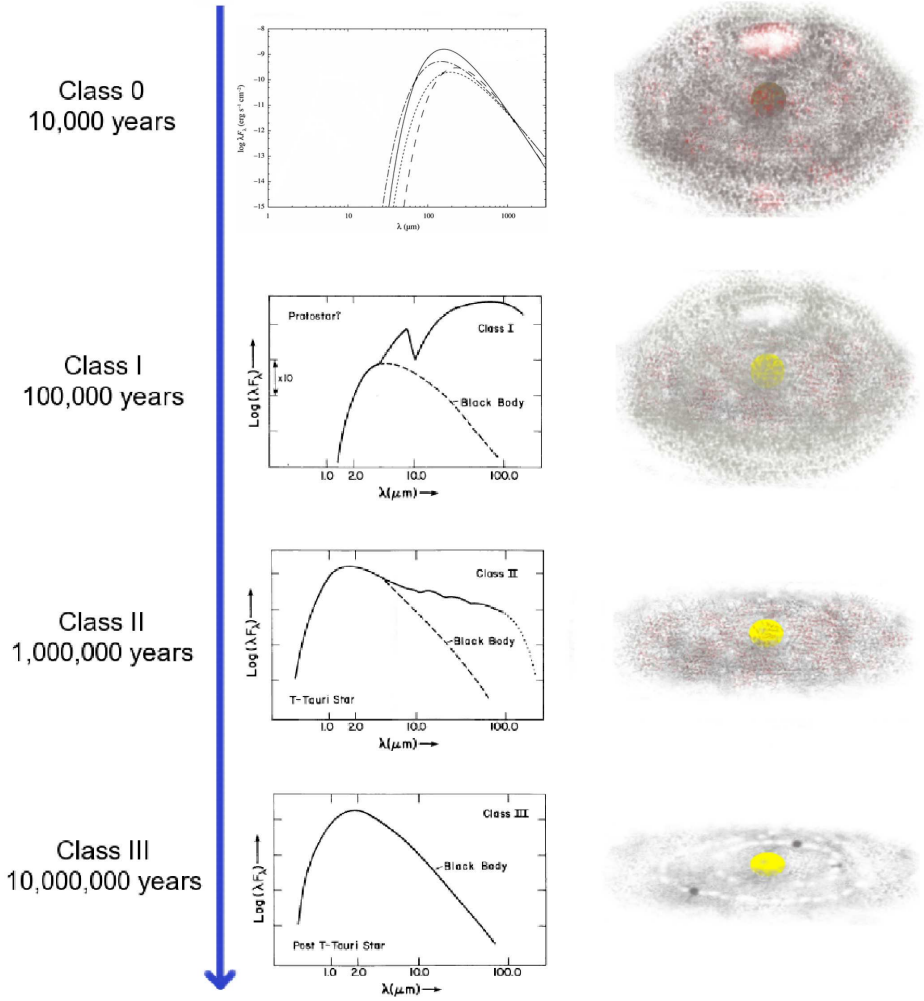

Figure 1.4: A pictorial representation of Spectral Energy Distribution (SED) evolution of a typical protostar from Class 0 to Class III. Initially the surrounding dust scatters light from the protostar leading to spectra with a strong infrared excess. As the system evolves, the volume of obscuring dust decreases and the visibility of the central protostar increases. The spectrum hence moves to shorter (hotter) wavelengths as it approaches that of a black body. SED plots adapted from figures of Lada (1987) and Tachihara et al. (2007).

These are believed to play a crucial role by removing excess angular momentum from the system to enable the cloud to collapse into a star (see Section 1.7). Close examination reveals evidence of infalling envelopes (e.g. Myers et al., 1995). Both the inflow and outflow are clear signs of a high rate of accretion onto the obscured central object. The high accretion rate suggests a short lifetime during this stage on the order of 10^4 years

and may in turn account for their rarity when compared to the abundance of the next evolutionary stage, Class I.

1.1.5 Stage 5: Class I

As the protostar's surrounding envelope thins by accretion onto the disc and through dispersal by the outflows, it may become optically visible if viewed close to pole on. There is still a substantial circumstellar disk present and accretion and outflows continue to remove excess spin angular momentum from the system.

Class I can be technically defined as having a bolometric luminosity between 70K and 650K ($70\text{K} < \text{T}_{bol} < 650\text{K}$). Similarly, we can say that the mass of the surrounding envelope is less than the mass of the central protostar, $\text{M}_{env} < \text{M}_{star}$. From Figure 1.4, we see that the blackbody curve has shifted to a shorter wavelength (higher temperature), yet there is an additional large infrared excess present from heating of the surrounding dust. The prominent absorption peak is believed to be due to silicate dust absorption at 10μm (Smith, 2004).

Molecular bipolar outflows persist but are less powerful with accretion rates of 10^{-5} $\text{M}_{\odot}\text{yr}^{-1}$. These accretion rates suggest the Class I stage can last on the order of 10^5 years.

1.1.6 Stage 6: Class II

After further development, the surrounding envelope completely disperses (but not the circumstellar disk) and the star becomes optically visible. Accretion continues but at a slower rate from a starved accretion disk, which may also be actively forming a planetary system. The disk still has a slight infrared excess on the back of the stellar blackbody spectrum (see Figure 1.4). The total mass of the accretion disk is now about 10^3 $\text{M}_{\odot}$. The lack of molecular gas present in the remainder of the surrounding envelope

for entrainment by the jets may make the outflow appear more atomic. The bolometric temperature range for this class is defined as between 650K to 2880K (650K $< T_{bol} <$ 2880K). The estimated age at this stage is 1–4$\times 10^6$ years. In addition, an ultraviolet excess may be visible which is believed to be where the material is accreting onto the now exposed stellar surface (Smith, 2004).

Class II objects also fall into an older category known as a 'Classical T Tauri Stars' (CTTS). This is another classification system based on the optical spectrum of the prototype star T Tauri (Joy, 1945). These stars had unusual spectra with strong Hα emission lines which are now believed to be from either circumstellar disks, accretion columns or outflows.

1.1.7 Stage 7: Class III

The circumstellar disk has all but dispersed leaving the spectrum as that of a stellar blackbody (see Figure 1.4). The bolometric temperature is now about 2880K (T_{bol} $>$ 2880K). A slight near-infrared excess compared to similar main sequence stars may sometimes be detectable suggesting the remains of debris in the system (Gullbring et al., 1998).

This class falls into a category known as 'Weak T Tauri Stars' (WTTS). Initially they were not thought to be young stars due to their lack of infrared excess emission. Later it was understood that they are associated with star forming regions, slightly more advanced that CTTS, yet no older than 20$\times 10^6$ years.

Accretion and outflows have now ceased and the star has reached its final mass. WTTS stars are typically faster rotators than CTTS as there is no longer a braking effect from the circumstellar disk and the rotation rate can increase. CTTS may typically have a rotation period of 10 days whereas WTTS may may have on average a rotation period of 1-2 days (Marilli et al., 2005). The rotation periods of CTTS and WTTS can generally be easily measured as both stages possess 'starspots'. These may

be cold spots due to high level of surface magnetic activity on the young protostars or hot spots at the base of accretion flows (Herbst et al., 1994). They can cover 3–20% of the stellar surface. Observations of the light curves of such stars can be seen to possess periodic oscillations directly providing the rotation period after assuming a $v \sin i$ orientation to our line of sight.

1.2 The HR diagram

What is now referred to as the Hertzsprung-Russell diagram was first created by astronomers Ejnar Hertzsprung and Henry Russell around 1910. They found that by plotting the spectral type against absolute magnitude of many stars, clearly defined regions emerged. These regions were later realised to be tracks that trace the general evolution of stars. Today, Hertzsprung-Russell diagrams are usually plotted as luminosity against effective temperature. These scales are similar to the original scales as it is now known that spectral type is directly related to effective temperature and luminosity is proportional to the absolute magnitude. Pre-main sequence stars can now be plotted on Hertzsprung-Russell diagrams, revealing information on protostellar evolution.

On the Hertzsprung-Russell diagram, pre-main sequence stars occupy a region to the lower right signifying low effective temperatures and luminosities.

Fully developed stars on the Main Sequence operate partially or entirely by radiative diffusion. Energy released in the nuclear fusion core is transferred by radiative means through their interior and, in the case of low mass stars, by convection from the radiative core to the surface. Young protostars are believed to transfer heat from their interior to their surface by convection processes alone as they contract on the Kelvin–Helmholtz timescale. Convection processes are more efficient in these cases as young stars possess large internal temperature gradients that easily carry the convection currents and their high level of opaqueness limits radiative diffusion.

As the young star contracts, the surface temperature remains roughly constant but the luminosity drops as L $\propto$ R^2 causing the evolution on the downward section of the tracks known as Hayashi Tracks (Hayashi (1966)) (see Figure 1.5). The decrease in luminosity means the temperature gradient and opacity fall, and radiative diffusion becomes the dominant process (Smith, 2004). A young star becomes a Main Sequence star at the Zero Age Main Sequence (ZAMS) track which defines the stage where nuclear fusion in the core becomes the primary power source.

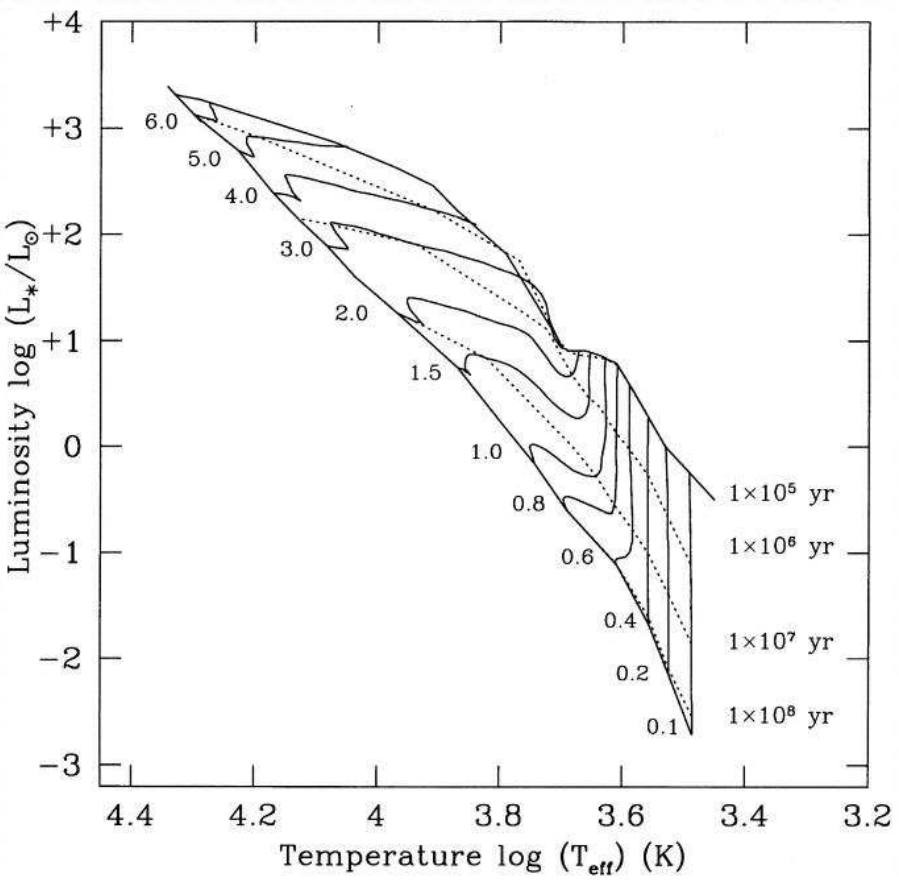

Figure 1.5: A pre-main sequence Hurtzsprung–Russell diagram displaying the evolutionary tracks of model stars between 6.0M$_\odot$ to 0.1M$_\odot$ The evolution begins from the upper diagonal line (1×10^5 yr) and evolves to the lower diagonal line (1×10^5 yr) signifying the ZAMS. The dotted lines represent isochrones. (Figure reproduced from Palla & Stahler (1999))

From Figure 1.5 we see that low mass pre-main sequence stars (M$_{star}$ $<$ 0.5 M$_\odot$) descend vertically along the convective Hayashi Tracks and initiate hydrogen fusion at

the ZAMS track without previously obtaining a radiative core. Intermediate mass stars ($0.5 < M_{star} < 2\ M_{\odot}$) possess convective cores which turn radiative before the onset of hydrogen burning. Higher mass stars ($M_{star} > 2\ M_{\odot}$), have little or no convective evolution and evolve horizontally to the ZAMS via radiative tracks referred to as Henyey Tracks (Henyey et al., 1955). Very low mass stars ($M_{star} < 0.08\ M_{\odot}$) will never reach the stage of hydrogen burning and become part of the population of objects known as 'Brown Dwarfs'.

The region before the $1{\times}10^5$yr isochrone in Figure 1.5 is known as the 'forbidden zone'. Objects located here would be either very young collapsing protostars not yet possessing a hydrostatic equilibrium, or stars heavily embedded in gas and dust thus masking their true temperature and magnitude.

1.3 Jet observations

We have discussed the process that leads to the creation of protostellar jets. Now we shall look at some observational data of well-known protostellar outflows before examining the key physical principles at work.

1.3.1 HH 1/2

The first jets and outflows were indirectly discovered by two astronomers, George Herbig and Guillermo Haro, who around 1950 independently catalogued mysterious small nebulous-like patches radiating Hα emission within the Orion Molecular cloud (Herbig, 1951, 1950; Haro, 1952, 1953). Initially, the patches were thought to be the actual sites of star formation. Only much later, in 1975, were they understood to be bow shocks - molecular/atomic cloud material excited by passing shock fronts driven by stellar winds (Schwartz, 1975).

HH 1 and 2 lie in the Orion A molecular cloud at a distance of 460pc. The distance

between the two bow shocks covers 0.34pc. Figure 1.6 displays an image of HH 1 and 2 taken by the Hubble Space Telescope. Hα emission at 6563Å is depicted as green and [SII] emission at 6716 and 6731Å is depicted as red.

The driving source of these outflows is the protostar known as VLA1. It is heavily obscured and hence not optically visible but has been located by extrapolating the outflow's proper motion back towards a central source, and also detected at centimeter wavelengths. Insufficient observational data exists on VLA1 in order to provide a full classification (Froebrich, 2005). Another source has been found close by known as VLA2, possibly a binary companion of VLA1 with a projected separation of 1380AU. It is believed to be driving the nearby HH 144/145 outflow (Reipurth et al., 1993).

Proper motions studies have found that parts of the HH1 bow shock are moving at over 400 km s^{-1} (Hester et al., 1998). The HH2 bow shock is moving slower with velocities under 100 km s^{-1}. The HH1 jet velocities range from 255–355 km s^{-1} which are on the order of 100 km s^{-1} less than the HH1 bow shock's peak-velocity suggesting the driving source is now ejecting material at a slower rate. With these values, the dynamical age of HH1 and HH2 is estimated to be about 450±100yr (Bally et al., 2002).

An image of HH1 is displayed in the upper left of Figure 1.6 with a close-up of the bow shock in the top right inset. The point of bright emission visible in the top inset is a Cohen-Schwartz (CS) star, unrelated with the outflow.

HH2 lies southeast of VLA1 and is displayed in the lower left of Figure 1.6 with a close-up of its bow shock in the bottom right inset. Unlike HH1, this bow shock appears to have fragmented into a cluster of 'mini-bows' or 'bullets'. The various components possess a range of velocities between 130–390 km s^{-1} (Bally et al., 2002). Numerical simulations have shown that it is possible for bow shocks to break up in such a way due to instabilities such as the Rayleigh-Taylor instability (Blondin et al., 1990). Recent 3D numerical simulations have also shown that both jet beam pulsation with fast precession and rotating jets can lead to broad unstable bow shocks which develop

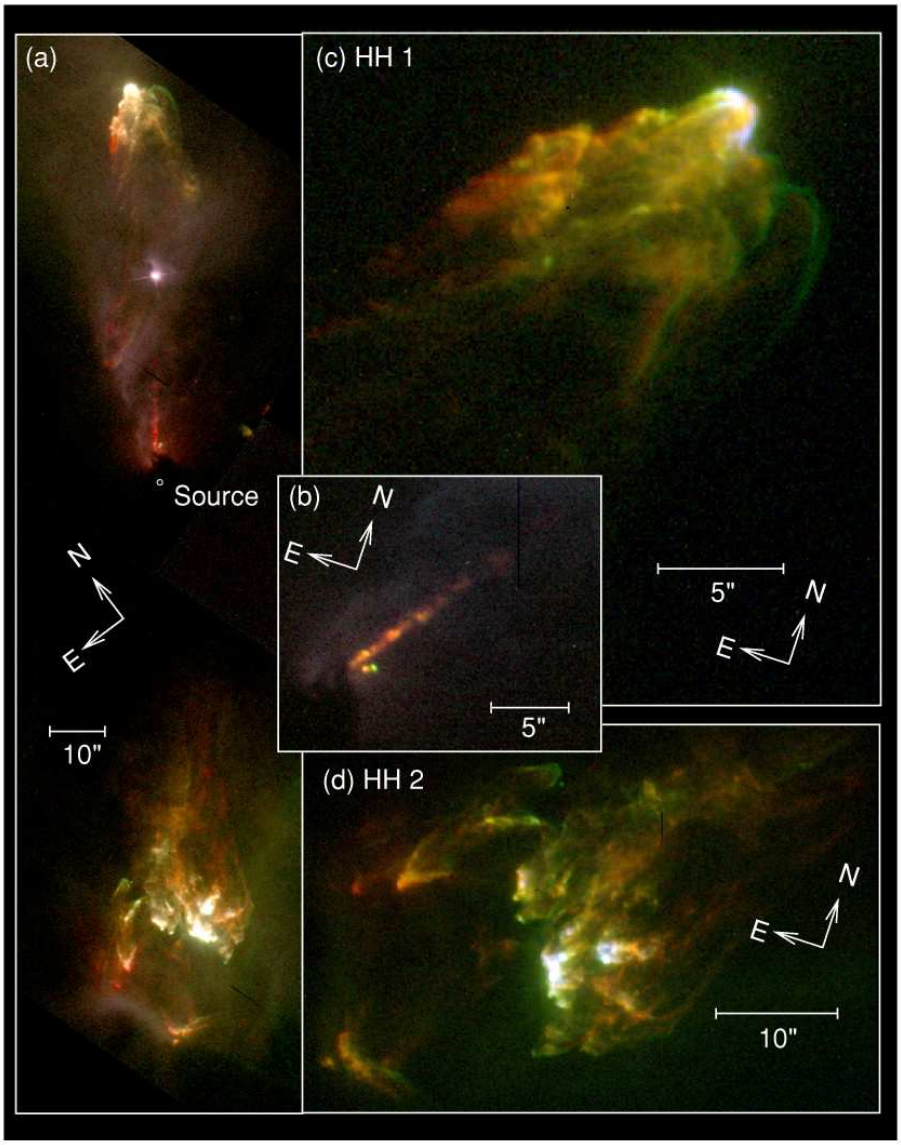

Figure 1.6: False colour composite image of HH1 and HH2 taken by the Hubble Space Telescope. [S II] emission is represented as red, Hα emission as green. The left hand-side image, (a), is a spatial view of HH1 and HH2 system with the location of the driving source highlighted. The inset image, (b), shows a close-up of the VLA1 jet. Image (c) shows a close-up of the HH1 bow shock and (d) shows a close-up of the HH2 bow shock. (Image reproduced from Hester et al. (1998).)

into smaller bow features (Rosen & Smith, 2004a; Smith & Rosen, 2007). The different morphologies between HH1 and HH2 may be due to different ambient environment properties on the two sides of the driving source.

The key to HH objects is supersonic motion. Material traveling supersonically suddenly heats or 'shocks' the nearby non- or slowly-moving material. The energy from the sudden heating causes electron transitions within the atoms and molecules present which creates the emission that is detectable at Earth. The shocks occur either within the supersonic jet (internal working surfaces) or the end of the outflow where it ploughs into undisturbed ambient medium (terminal working surface).

The central inset of Figure 1.6 shows the VLA1 jet, driving source of HH1. Despite both components of the bipolar outflow being visible, only this single blueshifted jet is visible. It is conceivable that the red shifted counterpart is too obscured behind cloud material to be detectable.

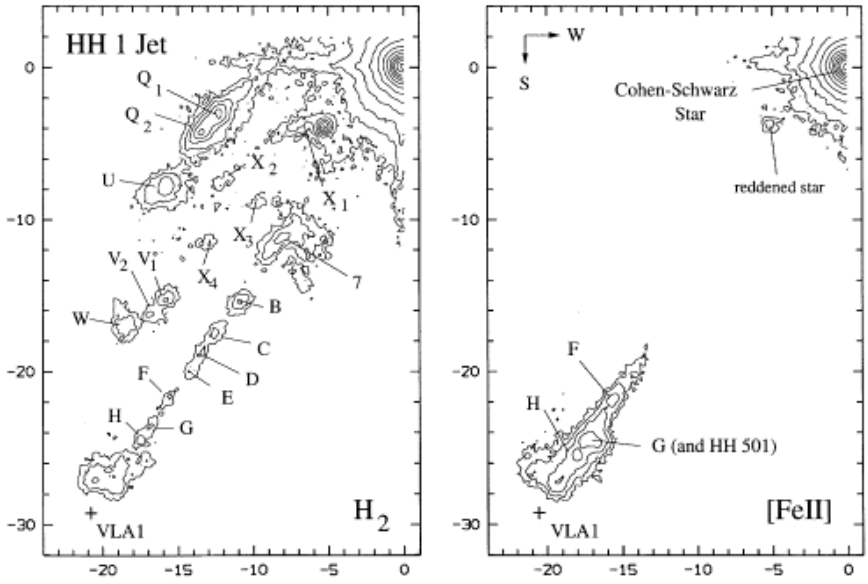

Figure 1.7: Contour plots of the HH1 jet clearly showing the 'knotty' structure. The co-ordinates are centered on the Cohen-Schwartz star in the top right of the plot at position RA $05^h36^m21.5^s$ and Dec.-06°45′36″ (2000). The contours display powers of two times the standard deviation of the mean background level. Reproduced from Figure 2 of Davis et al. (2000).

Figure 1.7 shows a contour plot of H_2 emission reproduced from Davis et al. (2000) who took high-resolution H_2 and [FeII] images of the HH1 jet and bow shock. As seen in Figure 1.6, the H_2 map shows the 'knotty' structure of the jet beam. Knots are a commonly observed feature of protostellar jets and are believed to be created by velocity variations in the jet beam caused by a variable or episodic jet launching mechanism (Raga et al., 1990). High velocity pulses overtake previously ejected slower moving material leading to a string of shockwaves.

There are two emission regions north of the presumed jet beam axis. The area labelled U, Q_2 and Q_1 in Figure 1.7 is believed to be part of the HH1 bowshock and area W, V_2, V_1 is likely to be part of a younger bowshock connecting to the emission knot labelled 7. The apparent one-sided eastern emission in regions labelled as W, V_2, V_1 and U, Q_2, Q_1 are believed to be where bow shocks are colliding with a denser ambient medium than on the western side (Davis et al., 2000).

1.3.2 HH 211

HH 211 is an ideal example of a highly collimated bipolar molecular outflow showing the phenomena of re-collimation, knots and entrainment. It was discovered in the Perseus Dark Cloud by McCaughrean et al. (1994) in the 2.122μm line of H_2 and found to be highly collimated with an aspect ratio of 15:1. The high level of collimation and the fact that it is deeply embedded suggests it is a very young outflow, on the order of 1,000 years old. The outflow covers 106″ on the sky and, assuming a distance of 315 pc to the Perseus Dark Cloud complex, the outflow has been measured to be 0.16 pc in length (O'Connell et al., 2005). The driving protostar has been categorised as Class 0 by Froebrich (2005) with the following parameters; $T_{bol} < 33$K, $L_{bol} = 3.6L_{\odot}$, submillimeter to bolometric luminosity ratio, $L_{smm}/L_{bol} = 0.046$, and $M_{env} = 0.80M_{\odot}$.

A detection of near-infrared continuum emission was made by O'Connell et al. (2005). The authors believe the continuum emission is created by light from the proto-

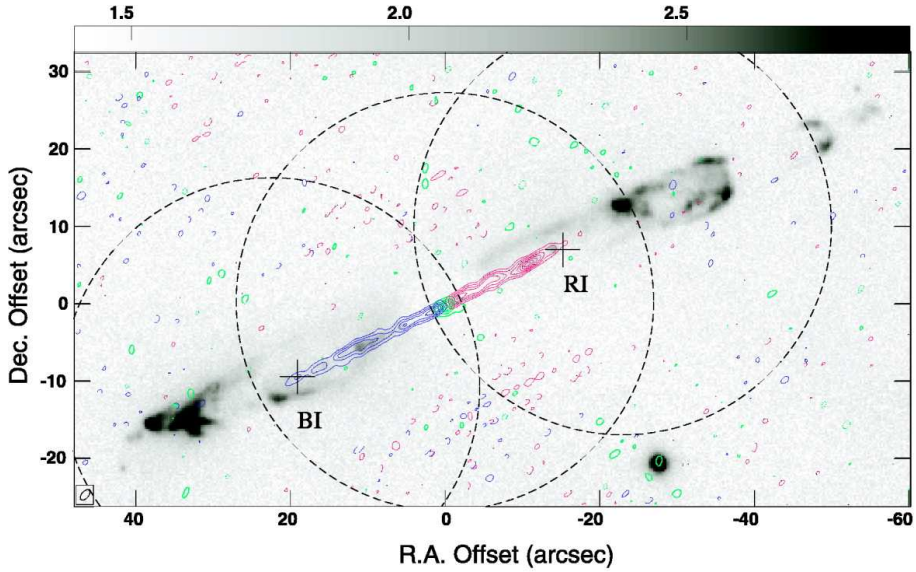

Figure 1.8: A composite figure of the HH211 outflow showing contours of the red and blue-shifted jet in SiO J = 5–4 emission taken by the Sub-Millimeter Array (SMA), superimposed on H_2 1–0 S(1) 2.122μm emission taken by the Very Large Telescope (VLT). Figure reproduced from Hirano et al. (2006).

star escaping through the jet beam cavity and scattering off denser material both along the cavity wall and from other denser clumps of material.

SiO J=5–4 observations made by Hirano et al. (2006), and displayed in Figure 1.8, revealed the blueshifted and redshifted jet components. They found the blueshifted velocities to range between -24 and -4 km s^{-1} and the redshifted velocities to range between +4 and +32 km s^{-1} relative to V_{LSR}= 9.2 km s^{-1}. The emission was found to trace a narrow jet of width 0.8″ (∼250 AU) with the jet consisting of a series of knots 3–4″ (∼1,000 AU) apart. The SiO emission does not trace as far as the lobes seen in H_2 emission. Either the density has become too low to excite the SiO, or all SiO has become completely dissociated. The observed discrepancy between the high density, high velocity gas along the axis, and lower density away from the axis is consistent with an X-Wind launching model (see Section 1.17) with a wide wind opening angle (Hirano et al., 2006).

Recent work by Lee et al. (2007) obtained estimates for the jet inclination angle, i,

with the formula $i = \sin^{-1}(v_m/v_j)$, where v_m is the mean velocity of the SiO emission, and v_j is the assumed jet velocity between 100–200 km s^{-1}. The inclination estimates were -8.6° to -4.3° for the redshifted jet and -11.4° to 5.7° for the blueshifted component. They also estimated the pulsation period from the inter-knot spacing. It was estimated to be between 44–15 years assuming a jet velocity of 100–200 km s^{-1}. A slight precession was also detectable by Lee et al. (2007).

We shall now look closely at the physics behind supersonic jets and outflows and show that a combination of physical theories with simulations can lead to an explanation of the observational features seen above.

1.4 The physics of jets and outflows

The output of a typical numerical jet simulation is displayed in Figure 1.9. It depicts the front section of an adiabatic axisymmetric (2.5D) simulation. The displayed parameter is the density on a logarithmic scale where lighter shading represents higher density and darker shading, lower density. The main jet features have been labelled and will be described below.

1.4.1 Jet beam

The jet beam is a supersonic flow of material which maintains high collimation over large distances. It is assumed to consist of excess accretion material channeled from the vicinity of the central source and accretion disk, then collimated and accelerated away by a certain mechanism (see Section 1.7). Jets related to accretion disks, be they protostellar or extragalactic, are generally bi-polar, emanating from both poles of the spin axis.

The difference between jets and outflows should be noted. The jet is composed

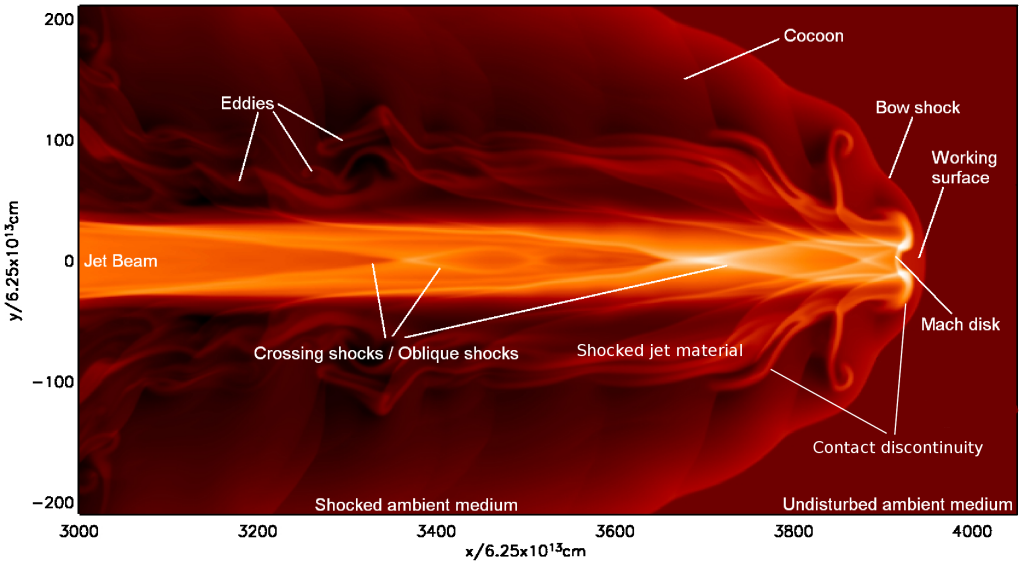

Figure 1.9: The front section of a high resolution, 2.5D axisymmetric adiabatic jet simulation with the characteristic jet features labelled. The simulation was performed with the ZEUS-3D hydrodynamic code and the diagram depicts density in units of gm/cm^{-3} displayed as a log scale where the brighter shading is higher density and darker shading is lower density. The jet beam is initially 10 times denser than the ambient medium and traveling at 200 km s^{-1} into a stationary uniform ambient medium. In axisymmetric simulations, only half the jet beam is simulated, making use of the assumption that most jets are cylindrical. In order to visualise them in two dimensions, the other half is simply mirrored through the axis of symmetry.

exclusively of excess accretion material ejected directly from the protostellar system. The outflow consists of both jet material surrounded by ambient material that has been entrained by the jet. The entrainment mechanism can occur either through bow shocks (see Section 1.4.3) or along the jet beam by mixing through the Kelvin-Helmholtz instability (see Section 1.4.2).

Numerical protostellar jet simulations typically come in two forms; jet launching simulations and jet propagation simulations. The former only concentrate on the region close to the protostar by modeling an accretion disk, a central object, and magnetic field. The high resolution required limits the size of the computational domain to a few AU around the star (e.g. Zanni et al. (2007) modeled a region of 3.6×10^{14}cm by 1.2×10^{14}cm by 1.2×10^{14}cm). On the other hand, jet propagation simulations (the

type presented in this thesis) assume the jet has already been launched and collimated somewhere off the grid by a certain process and only model the propagation of the collimated jet beam and its interaction with the ambient environment. Such an assumption allows for much larger domains to be simulated (e.g. Keegan & Downes (2005) modeled a region of 9.257×10^{17}cm by 9.257×10^{16}cm).

Various jet beam properties can be quantified as presented by Smith (2004). In the most basic form, two cylindrical jet beams would have a mass outflow rate, M_j, of

$$\dot{M}_j = 2\pi r_j^2 \rho_j v_j \tag{1.5}$$

where r_j, ρ_j and v_j are the jet beams radius, density and velocity respectively. Applying observationally constrained parameters, Class 0 mass outflow rates can be expressed as

$$\dot{M}_{j\ (Class\ 0)} = 1.3 \times 10^{-5} \left(\frac{r_j}{500AU}\right)^2 \left(\frac{n_j}{10^5 cm^{-3}}\right) \left(\frac{v_j}{100\ km\ s^{-1}}\right) M_\odot yr^{-1} \tag{1.6}$$

where n_j is the hydrogen nucleon density, assuming a 10% helium abundance.

Outflows from the more evolved Class II sources differ as they are associated with higher velocities and lower densities

$$\dot{M}_{j\ (Class\ II)} = 1.6 \times 10^{-8} \left(\frac{r_j}{100AU}\right)^2 \left(\frac{n_j}{10^3 cm^{-3}}\right) \left(\frac{v_j}{300\ km\ s^{-1}}\right) M_\odot yr^{-1} \tag{1.7}$$

Equations for the jet thrust, F_{jet}, and power or luminosity, L_{jet}, for Class 0 objects can similarly be written as

$$F_{j\ (Class\ 0)} = 5 \times 10^{-4} \left(\frac{\dot{M}_{jet}}{10^{-5} M_\odot yr^{-1}}\right) \left(\frac{v_j}{100\ km\ s^{-1}}\right) M_\odot\ km\ s^{-1} yr^{-1} \tag{1.8}$$

and

$$L_{j\ (Class\ 0)} = 8.2 \left(\frac{\dot{M}_{jet}}{10^{-5} M_\odot yr^{-1}}\right) \left(\frac{v_j}{100 kms^{-1}}\right)^2 L_\odot \tag{1.9}$$

These equations show that jets from Class 0 sources are quite powerful and can contain

a large fraction of the total radiative power of the protostar, 0.1–0.5 L_{bol} (Smith, 2004).

1.4.2 Kelvin-Helmholtz discontinuity

The Kelvin-Helmholtz instability arises on considering the centrifugal force at the contact region, or 'slip surface' between two fluids of different densities and velocities, but with a pressure equilibrium across the interface. Small instabilities can grow exponentially leading to turbulent entrainment. It can destabilise the collimation of the jet beam over length scales of 10–20 $M_j R_j$ where M_j is the Mach number of the jet and R_j is the radius of the jet (Smith, 2004).

In the case of protostellar jets, slip surfaces exist between the jet beam and the processed cocoon material. This region is also known as the 'contact discontinuity', and labelled in Figure 1.9. The jet beam acts a resonant cavity for transverse sub-sonic acoustic waves confined within the interior of the beam. The acoustic waves must be sub-sonic otherwise they would create disruptive shock waves. Certain frequencies or modes become amplified and can grow into Kelvin-Helmholtz instabilities (Stone, 1997).

1.4.3 Bow shock – Working surface – Mach disk

As mentioned previously, shocks and molecular emission are the key to how outflows reveal themselves to observers on Earth. The bow shock occurs at the end of the jet beam where the supersonic jet collides directly with the subsonic ambient medium. These collisions create the Herbig-Haro objects of Section 1.3.1. Smaller internal shocks along the jet beam have been noted from observations of the jet 'knots' (Section 1.3.2) and have been successfully modeled in simulations through jet beam velocity variations e.g. Rosen & Smith (2003).

We shall now look at the basis of the physics behind shocks and molecular emission.

1.4.4 Shocks

At the front of any supersonic jet are two interfaces known by various names. They are the 'Bow shock' or 'Forward shock' at the front and the 'Mach disk', 'Jet shock' or 'Reverse shock' at the back. The bow shock pushes against and accelerates the undisturbed ambient medium, whereas the mach disk decelerates supersonic jet beam material. Observations and simulations suggest that in some situations material that has been highly collimated from the reverse shock is capable of overtaking the forward shock leading to streams of bright emission (Smith et al., 2007).

In Figure 1.10, a simplified depiction of the basic double shock structure is presented. Region 1 of the diagram consists of jet material of density ρ_1, moving at velocity

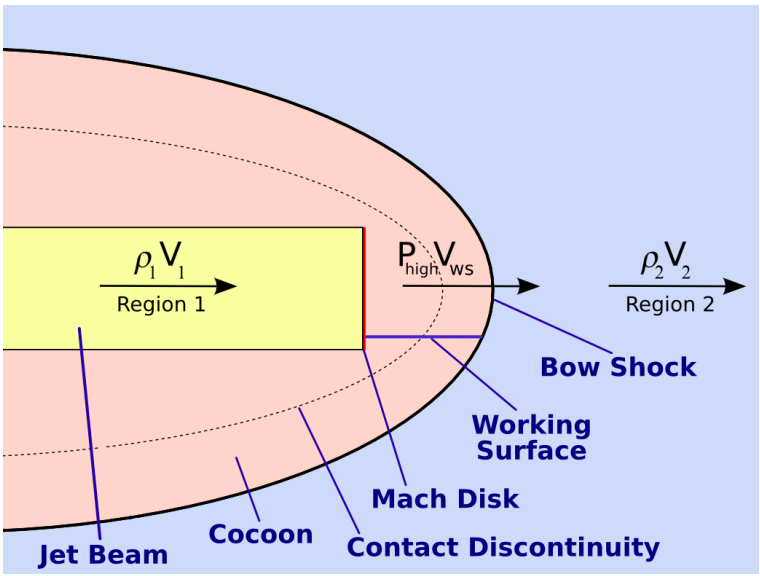

Figure 1.10: A simple schematic diagram showing the densities and velocities in the three regions of the double shock structure.

V_1. It propagates into an ambient medium, Region 2, of density ρ_2, and velocity V_2. The formation of the interface region between the two shocks is a consequence of any supersonic flow. The 'Working surface' is a high pressure region of P_{high} in the diagram and moving at velocity ,V_{ws}, which is subsonic if viewed in the frame of reference of the jet beam motion. The 'Contact discontinuity' separates shocked jet beam material,

which has passed through the Mach Disk, from shocked ambient material, which has passed through the bowshock. Although the temperature and densities differ on each side of the contact discontinuity, the pressure is the same. This pressure equilibrium prevents the material on each side of the discontinuity from mixing initially. It may later mix through the Kelvin-Helmholtz instability.

In numerical simulations, it is common to define the input parameters in a dimensionless form. The ratio of the densities of the jet, ρ_{jet}, and ambient medium, ρ_{amb}, is typically defined as the parameter η, ($\eta = \rho_{jet}$ / ρ_{amb}). Similarly, the ratio of the pressures of the jet, p_{jet}, to ambient medium, p_{amb}, is defined by the parameter κ, ($\kappa = p_{jet}$ / p_{amb}).

Assuming the ambient medium is stationary ($V_2 = 0$), the velocity of the working surface, V_{ws}, can be expressed in terms of the jet beam velocity, V_1, and the density ratio, η, as

$$V_{ws} = \frac{\sqrt{\eta}\ V_1}{1 + \sqrt{\eta}} \tag{1.10}$$

(Norman & Winkler, 1985). The above equation shows that if we have a 'light' jet, meaning the jet density is less than that of the ambient medium ($\eta < 1$), then $V_1 < V_{ws}$. This leads to a pronounced working surface which easily sweeps up material from the ambient medium (Region 2) leading to a large expanded cocoon. Such 'light' jets are typically associated with extragalactic jets, e.g. Sutherland & Bicknell (2007). Conversely, in the case of a 'heavy' jet, $\eta > 1$ then $V_1 > V_{ws}$. The jet beam ploughs ahead preventing the working surface from dominating and little ambient material is entrained leading to sharp diminished bow shocks. Heavy jets are usually associated with protostellar outflows. HH211 was estimated to have a maximum η of $\sim$20 (O'Connell et al., 2005). In our simulations we fix the initial value of η to 10.

What is the physical principle behind shock creation? Shocks are a natural consequence of supersonic motion which is defined as the transmission of information by sound waves moving through a medium faster than the local sound speed of the medium.

Shock waves were first investigated experimentally around 1886 by Ernst Mach who derived the Mach angle equation,

$$\sin(a) = \frac{c_s}{v} \tag{1.11}$$

where v is the velocity of the object, c_s is the ambient medium sound speed, and a is the opening angle of the resulting bowshock (if $v > c$).

A comprehensible understanding of shock waves is presented by Norman & Winkler (1985) and depicted in their Fig. A and Fig. B, reproduced here as the combined Figure 1.11.

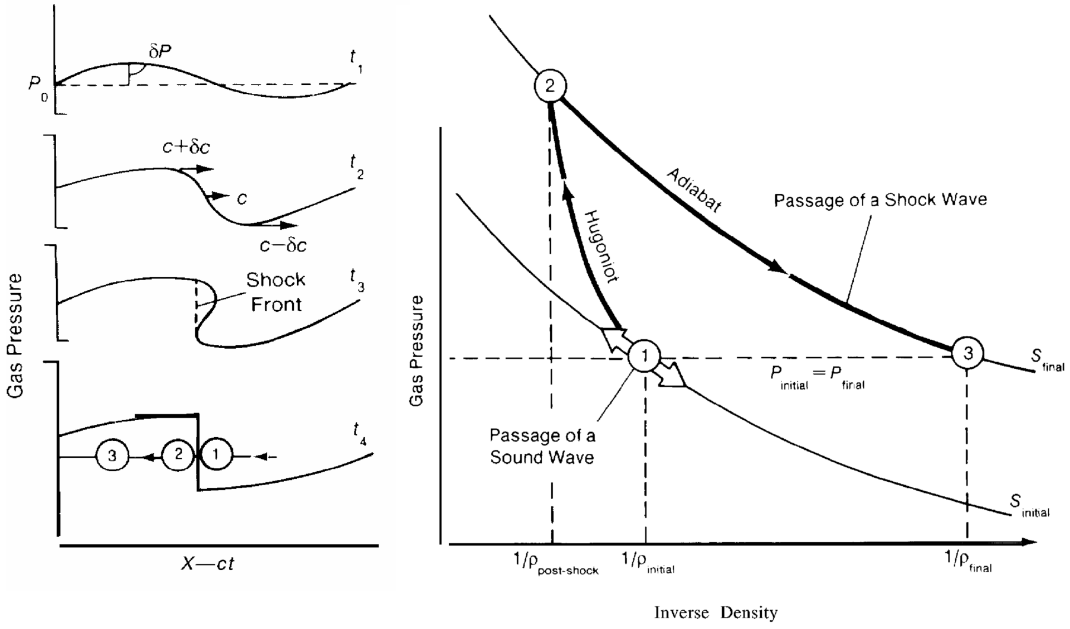

Figure 1.11: Left: Diagram showing the creation of a shock-wave. Regions labelled 1, 2 and 3 correspond to the labelled positions on the Pressure versus $1/\rho$ plot, Right. (Figure reproduced from Fig. A and Fig. B of Norman & Winkler, 1985.)

Figure 1.11(left), depicts an oscillating sound wave of amplitude $2\delta P$. If the wave were to move faster than the sound speed, the simple sinusoidal wave pattern would be destroyed leading to the creation of a discontinuity or a shockwave. Approaching waves from the downstream direction are unaware of the sudden change as information of the

shock properties can not be transmitted downstream in time. An analogous situation can be seen with ocean waves. As the depth of the water decreases approaching the shore, the energy is confined to a narrower region. The amplitude increases leading to the 'breaking' phenomenon depicted in Figure 1.11(left).

Figure 1.11(right), shows a plot of pressure versus the inverse of density. The inverse density is also proportional to the volume. Sound waves propagating through the fluid or gas cause the properties of the medium to move back and forth along the lower line signifying an adiabat (an isentropic process). As the pressure increases, the volume of the gas decreases. Similarly, as the pressure decreases, the volume increases keeping temperature constant. With the passage of a shock front, the particles suddenly receive thermal energy. This heating causes the system to rise to an adiabat of higher energy. Although the gas can relax again to the previous pre-shock pressure, the temperature and volume are irreversibly changed, i.e. the entropy has increased (Norman & Winkler, 1985).

Two types of interstellar shocks have been identified: Jump-Shocks, or 'J-Shocks', and Continuous shocks, or 'C-Shocks'. J-Shocks are characterised by two components, a sharp increase in temperature followed by a long cooling region. C-Shocks display a wide weak excitation zone, with ambipolar diffusion softening the shock (Smith, 2004).

1.4.5 Molecular chemistry

Molecules are a crucial component of star formation. They act as coolants which allow core collapse to occur by allowing the released gravitational energy to be radiated away. The emitted radiation is at low-energy (infra-red to radio wavelengths) allowing observers to probe the relatively cool molecular clouds.

The most abundant molecule is the simplest, namely molecular hydrogen, H_2, consisting of two protons and two electrons. To form H_2, two hydrogen atoms must collide and combine through the negative energy anti-parallel electron spin singlet state, $^1\Sigma$.

The usual formation method of molecules on Earth is through a three-body collision where two atoms combine in the presence of a third atom to carry away excess binding energy in the form of kinetic energy. This reaction mechanism only has a high probability in high densities of 10^{12}cm^{-3} so does not occur in molecular clouds. Another possible mechanism, through a radiative transition from the $^3\Sigma$ to the $^1\Sigma$ state, can not occur through the quantum mechanical selection rules due to the symmetry of the H_2 molecule. In molecular clouds, H_2 forms through grain surface reactions where the dust grains behave as a catalyst (Hollenbach et al., 1971). Hydrogen atoms effectively stick to the grains and the grains behave as the third body in the three-body reaction scenario.

$$\begin{aligned} \mathsf{H} + \mathsf{H} + \mathsf{grain} &\rightarrow \mathsf{H_2} + \mathsf{grain} \\ \mathsf{H_2} + \mathsf{H} &\rightarrow 3\mathsf{H} \\ \mathsf{H_2} + \mathsf{H_2} &\rightarrow 2\mathsf{H} + \mathsf{H_2} \end{aligned} \tag{1.12}$$

Once H_2 forms, it is the building block of heavier molecules such as CO and H_2O, which can dynamically form and be destroyed with the passage of shockwaves. For example, the reaction path for the creation of H_2O through ion-molecule reactions is as follows,

$$\begin{aligned} \mathsf{H_2} + \mathsf{c.r.} &\rightarrow \mathsf{H_2^+} + \mathsf{e^-} \\ \mathsf{H_2^+} + \mathsf{H_2} &\rightarrow \mathsf{H_3^+} + \mathsf{H} \\ \mathsf{H_3^+} + \mathsf{O} &\rightarrow \mathsf{H_2} + \mathsf{OH^+} \\ \mathsf{OH^+} + \mathsf{H_2} &\rightarrow \mathsf{OH_2^+} + \mathsf{H} \\ \mathsf{OH_2^+} + \mathsf{H_2} &\rightarrow \mathsf{H_3O^+} + \mathsf{H} \\ \mathsf{H_3O^+} + e^- &\rightarrow \mathsf{H_2O} + \mathsf{H} \end{aligned} \tag{1.13}$$

where, c.r. represents a cosmic ray, $\mathsf{e^-}$ is an electron, species superscripted with '+' represent intermediate positive ions (Stahler & Palla, 2005).

1.4.6 Molecular emission

Here we shall take a closer look at the physics behind molecular emission. Molecular emission is similar to the process of atomic emission. Atomic emission occurs when bound electrons make transitions between quantised energy levels through the absorption and emission of photons at certain wavelengths as determined by the quantum mechanical selection effects. The formation of a molecule introduces rotational and vibrational transitions, which are of lower energy than atomic transitions, but still controlled by quantum mechanical selection effects.

The simplest molecules are diatomic and we can imagine two bound nuclei orbiting each other about their common centre of mass. The total energy can be calculated from the angular momentum, $J = I\ \omega$, and the kinetic energy, $K = \frac{1}{2}\ I\ \omega^2$. When combined, they give the total energy of the system as

$$E = \frac{J^2}{2I} \tag{1.14}$$

where J is the angular momentum and I is the moment of inertia.

Angular momentum is quantised so that $J^2 = j(j+1)\hbar^2$ where j is the rotational quantum number, $j = 0, 1, 2, 3 \ldots$, and $\hbar$ is the Dirac Constant based on the Planck Constant, h, through the relation $\hbar = \frac{h}{2\pi}$.

The final equation for the rotational energy levels is

$$E_{rot} = j(j+1)\frac{\hbar^2}{2I} \tag{1.15}$$

Rotational levels have been assigned the following labelling scheme. ΔJ = -2, -1, 0, +1, +2 corresponds to O, P, Q, R and S branches respectively.

In addition, the two nuclei may oscillate or vibrate as if connected by a spring. The

resulting vibrational energy is given as

$$E = (v + \frac{1}{2})\hbar\omega \tag{1.16}$$

where v is the vibrational quantum number, $v = 0, 1, 2, 3 \ldots$ (Stahler & Palla, 2005).

The ratio between two levels of a two-level system can be quantified through the Boltzmann Distribution equation

$$\frac{N_1}{N_0} = \frac{g_1}{g_0} exp\left(\frac{-\Delta E_{10}}{k_B T}\right) \tag{1.17}$$

where N_1 and N_0 are the number densities in the upper and lower levels respectively, g_1 and g_0 are the degeneracies of the levels, ΔE_{10} is the energy difference between the two levels, k_B is the Boltzmann constant, and T is the excitation temperature (Stahler & Palla, 2005).

Carbon monoxide, CO, is an important molecular tracer. The $^{12}C^{16}O$ isotope is the most abundant, but $^{13}C^{16}O$ and other forms are also present and detectable at lower abundances. The main transition for CO is due to its permanent electric dipole moment. This transition is from the J = 1 → 0 rotational level. The energy released is δE = 4.8×10^{-4}eV which is equivalent to a photon of wavelength 2.60 mm in the radio regime and a cooling of 5.5 K. Excitation to invoke the transition is believed to occur through collisions with H_2.

Unlike CO, molecular hydrogen does not possess a permanent dipole moment due to the symmetry of the molecule. It does however have a permanent quadrupole moment so J is allowed to change by two units (ΔJ = ±2, an O, Q or S branch). The common 1–0 S(1) line at 2.12μm is a ro–vibrational transition where Δv = 1 → 0 and ΔJ = 3 → 1. A similar line of slightly higher energy is the 2 → 1 S(1) line at 2.24μm. Pure rotational transitions can occur in the vibrational ground state. The ΔJ = 3 → 1 transition occurs at 17.04 μm and the ΔJ = 2 → 0 transition occurs at 28.22 μm.

Table 1.1: Main tracer wavelengths. Species in the square brackets represent forbidden transitions. Forbidden transitions have an extremely low probability of occurring in even the best laboratory vacuum on Earth, but may occur in the low densities of interstellar space and molecular clouds.

Molecule	Wavelength λ	Transition type	Gas Temperature	Shock velocity
H_2	2.121 μm	$1 \rightarrow 0$ S(1) vibrational	6,600K	30–50 km s^{-1}
	2.248 μm	$2 \rightarrow 1$ S(1) vibrational	12,500K	
CO	2.6 mm	$J = 1 \rightarrow 0$ rotational	5.5K	
[O I]	63 μm	$^3P_1 \rightarrow ^3P_2$	230K	
[C II]	158 μm	$^3P_{3/2} \rightarrow ^2P_{1/2}$	92K	
[Fe II]	1.64 μm	$^4D_{7/2} \rightarrow ^4F_{9/2}$	10,000K	>50 km s^{-1}

The modeling of the actual electron transitions in atoms and molecules during a simulation would be very computationally intensive. Molecular cooling is usually represented on the macroscopic scale by using pre-calculated cooling functions which plot temperature as a function of cooling. This significantly reduces the computational requirements. See Section 2.5 for a description on how the molecular cooling module for ZEUS-3D operates.

Table 1.1 shows some information on the main molecular tracer species including the wavelengths at which the emission occurs and the temperatures required for such emission.

1.5 Disk formation

A long standing puzzle in star formation has been how a protostar can form from a collapsing rotating cloud without the angular momentum of the system increasing to a critical value. As seen in Section 1.1.3, the angular momentum is carefully regulated by the system where excess angular momentum is removed by jets. Here we shall look at how material propagates inward from the gravitationally bound clump of Stage 3 in Figure 1.1 onto the central protostar.

The theory can explain the formation of *low* mass stars. High mass stars of masses

$>$ 8–10 $M_{\odot}$ are thought to form in a fundamentally different way due to the fact that when such high masses are reached, the radiation pressure from the centre would be strong enough to halt the momentum of further in-flowing accretion columns. Massive stars do however exist in the form of O and B stars with massess over 100 $M_{\odot}$ possible e.g. Massey et al. (2000). A model for massive star formation through the mergers of lower mass stars or cores in dense stellar clusters was first suggested by Bonnell et al. (1998). However, observations have shown that circumstellar disks are a common occurrence around high mass stars suggesting they do form through the collapse/accretion mechanism reminiscent of low mass stars (Jiang et al., 2008). Recent models of the gravitational collapse of massive magnetised molecular cloud cores were performed by Banerjee & Pudritz (2007) who succeeded in simulating the creation of massive stars which formed through high accretion rates of $10^{-3}M_{\odot}yr^{-1}$. They found that angular momentum was efficiently transferred through bars/spirals and magnetic torques. They also found that the bipolar outflows which formed in their magnetized simulations produced cavities which aided the release of radiation pressure thus allowing accretion to continue and again showing the importance of jets.

Returning to low-mass stars, observations show that some stars maintain a constant angular velocity over several million years as they contract while evolving along their Hayashi tracks. This in itself suggests a strong braking effect is present over timescales of 2–10 Myr (Herbst et al., 2007). In order to achieve this, models have shown that roughly one third of the total stellar angular momentum must be removed from the system per Myr. This implies that magnetic disk braking must not only positively balance the torque of the shrinking protostar but also increase with time. Statistically, observations suggest that a magnetic star-disk interaction does resist and brake the spin-up of pre-main sequence stars (Herbst et al., 2007).

In the rotating collapse theory, material in the surrounding envelope first settles onto an equatorial mid-plane disk then propagates through the disk to smaller radii, before finally spiraling onto the stellar surface of the central protostellar core. It is

based on the physical principle of any system tending towards a lowest energy state.

A simple mathematical analysis of rotating collapse was presented by Hartmann (2001) and Stahler & Palla (2005) as follows: We have a central protostar of mass $M_\star$, surrounded by a low density circumstellar cloud or envelope of material. We imagine a small element of the circumstellar material possessing an eccentric parabolic orbit about the central protostar (see Figure 1.12). The highest velocity, V_{max}, of the element in its orbit is reached at the point of closest approach, r_{min}, to the central object (where the element would need to have moved through the mid-plane disk depicted in Figure 1.12). Based on Newton's Law of Gravitation the maximum velocity, V_{max}, is given as

$$V_{max}^2 = \frac{2GM_\star}{r_{min}} \tag{1.18}$$

where G is the gravitational constant.

We now introduce the specific angular momentum vector, h, where $h = \mathbf{r}\times\mathbf{v}$, the cross product of the orbital position vector, $\mathbf{r}$, and the orbital velocity vector, $\mathbf{v}$. The specific angular momentum can be written in terms of G and M with the use of Equation 1.18 as follows

$$h^2 = r_{min}^2 V_{max}^2 = 2\ G\ M_\star\ r_{min} \tag{1.19}$$

A parabolic trajectory can be defined as $r = \frac{r_{eq}}{1+cos\phi}$ where r is the distance of the moving element to the central object (the focus point of the parabola), r_{eq} is the distance to the central object while in the orbital plane (see Figure 1.12), and ϕ is the phase angle of the orbit between periastron and the current location of the moving element. Clearly $r_{min} = \frac{r_{eq}}{2}$ (when $\phi = 0°$), thus $\mathrm{r}_{eq} = 2\ \mathrm{r}_{min}$. Therefore the orbital distance is related to the specific angular momentum by

$$r_{eq} = \frac{h^2}{GM_\star} \tag{1.20}$$

The specific angular momentum is related to the total angular momentum, Ω, in the

following way. Material in the plane perpendicular to the rotation axis has a higher angular momentum than material with more inclined orbits or trajectories. It varies as

$$h = \Omega r_0^2 \; sin\theta \tag{1.21}$$

where θ is the angle from the rotation axis (see Figure 1.12). Inspection of Equation 1.21

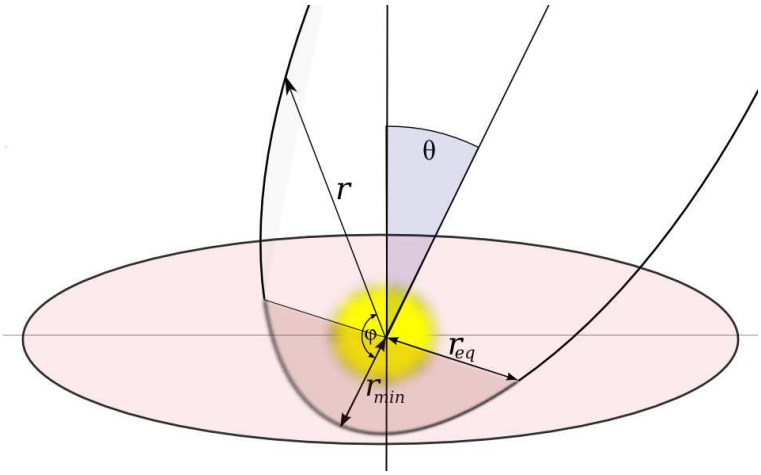

Figure 1.12: Schematic diagram to aid the disk formation explanation. Shown are the disk plane and a highly eccentric orbit at angle θ to the rotation axis.

implies that for material moving near the rotation axis, $\theta \sim 0°$, and so the angular momentum is low and the material can easily fall onto the central protostar. If θ is $\sim$ 90°, the material has high angular momentum with a highest centrifugal radius, r_c, of

$$r_c = \frac{r_o^4 \Omega^2}{GM} \tag{1.22}$$

Material with a high specific angular momentum collects into a mid-plane disk. When material falls onto the mid-plane disk it collides with material already there and loses its normal velocity component yet keeps its in disk velocity component (Hartmann, 2001).

The existence of circumstellar disks have now been proved by direct observational evidence such as the HST Wide Field Planetary Camera 2 (WFPC2) images of the Orion Nebula by Bally et al. (1998) with an example displayed in Figure 1.13. The

disks are seen in silhouette against the background nebulosity.

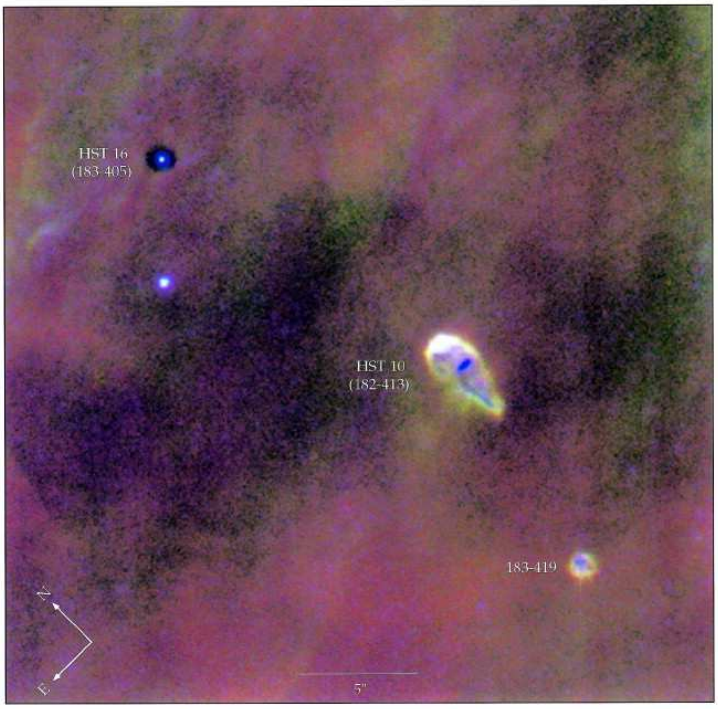

Figure 1.13: Reproduction of Fig.5 from Bally et al. (1998) showing some silhouetted disks around young stars in the Orion Nebula. In this composite image, red is represented as [N II] emission, green as Hα, and blue as [O I].

Possibly the most studied protostar possessing a disk is HH30 where we view a flared disk edge-on and see a bipolar jet emerging perpendicular to the plane of the disk (see Figure 1.14). Recent 0.3″ resolution observations of the system by Guilloteau et al. (2008) suggest the inclination angle of the disk to our line of sight is 81 ± 3° with an outer disk radius of 128 ± 3 AU and an inner radius truncation at 37 ± 4 AU surrounding a binary system at the center. Systems with circumstellar disks have been given the popular name 'Proplyds' after Proto-planetary Disks. Disk masses in the Trapezium cluster are estimated to have an average mass of 0.005 $M_{\odot}$ (Eisner & Carpenter, 2006).

1.6 Accretion

Now the material from the surrounding envelope is settling onto a rotating circumstellar disk. In order for the material to spiral inwards towards the protostar at the centre of the disk, more gravitational energy and angular momentum must be lost.

The simplest model to explain accretion is that of a Keplerian disk in differential rotation as explained by Hartmann (2001). The physics of a Keplerian disk is exclusively defined by gravity. The angular velocity, Ω, of a rotating Keplerian disk is given as

$$\Omega = \sqrt{\frac{GM}{r^3}} \tag{1.23}$$

We can imagine the disk to consist of a series of annuli or orbits of increasing radii from the center. Furthermore, we imagine two bodies of masses m_1 and m_2 lying in adjacent annuli both orbiting the central protostar at radii r_1 and r_2 respectively. The energy of this simplified system is thus

$$E = -\frac{1}{2}GM\left(\frac{m_1}{r_1} + \frac{m_2}{r_2}\right) \tag{1.24}$$

and the angular momentum, L, is

$$L = \sqrt{GM}(\sqrt{r_1}m_1 + m_2\sqrt{r_2}m_2) \tag{1.25}$$

As the two masses orbit in adjacent annuli, they travel at different velocities (from Equation 1.23) and interact through frictional and viscous forces. The perturbation relationship can be written as

$$\frac{m_1}{\sqrt{r_1}}\delta r_1 = -\frac{m_2}{\sqrt{r_2}}\delta r_2 \tag{1.26}$$

where δr_1 and δr_2 are extents of the perturbations. This relationship ensures that the total angular momentum, J, remains conserved.

The change in energy invoked on the first body is given as

$$\Delta E = -GMm_1 \frac{\delta r_1}{2r_1^2} \left(\left(\frac{r_1}{r_2} \right)^{\frac{3}{2}} - 1 \right) \tag{1.27}$$

The above equation shows that if m_1 were to be initially closer to the center ($r_1 < r_2$), the energy can be reduced by decreasing Δr_1, or moving to a lower orbit. On the other hand, if $\mathrm{m_1}$ were to initially lie at a greater radius ($\mathrm{r_1} > \mathrm{r_2}$), the energy of the system can be reduced by increasing Δr_1, or moving it to a higher orbit. Physically, as the material in the disk is a gas, the masses from adjacent annuli will mix. From the frictional effects alone, the higher angular momentum mass in the lower orbit will tend to speed up the mass in the higher orbit and vice versa. The overall result is that angular momentum is effectively transported outward to larger disk radii and material at smaller radii loses angular momentum and propagates closer to the protostar (Hartmann, 2001).

The actual system is much more complex than this simple analysis. Even through magnetic coupling to the disk, the central protostar possesses a significant amount of angular momentum which must be removed. Observations show that T Tauri stars have typical rotation velocities of 10–25 km $\mathrm{s^{-1}}$. Excess angular momentum is removed by an outflow of material perpendicular to the disk. Direct observational evidence of this phenomenon exists such as the HH30 disk and outflow imaged by the HST and shown in Figure 1.14. Both the launching and collimation process of the jet is believed to be a natural consequence of magnetic field interaction between the protostar and the accretion disk.

As noted by Ferreira (2007), the accretion disk that is capable of launching a magnetized jet differs from the ideal understanding of an accretion disk. The Keplerian accretion disk is an ideal case. It has been referred to as the Standard Accretion Disk (SAD) by Ferreira (2007), and possesses an accretion rate of $\dot{M}_a = -2 \int_0^h 2\pi r \rho u_r dz$ which is constant with time and radius. In the realistic case the author describes a Jet Emitting Disk (JED) where the disk losses mass over its surface so that $\dot{M}_a$ is not constant and varies with radius.

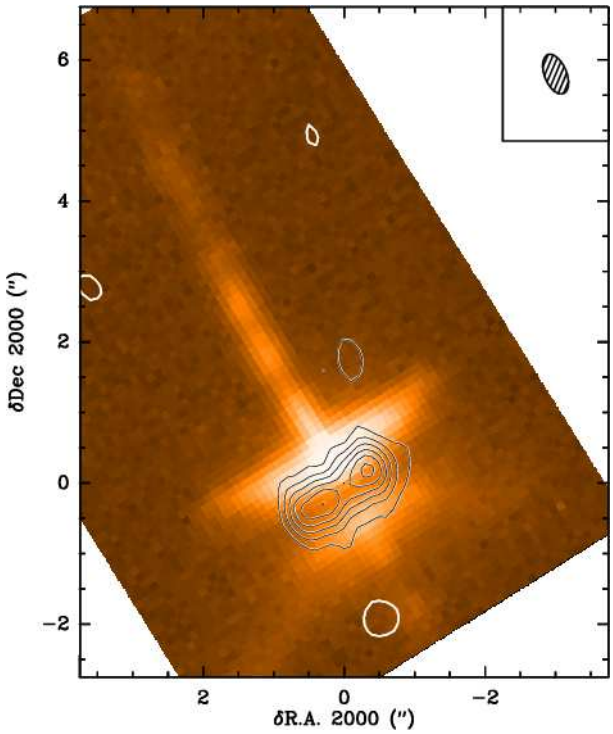

Figure 1.14: Reproduction of Fig.1 from Guilloteau et al. (2008) showing a PdBI 1.30 mm continuum map overlaid on the HST image of the HH30 jets.

Much numerical work has been performed in recent years to simulate accretion processes, most creating impressive visualisations in order to aid understanding. An example visualisation of magnetic accretion model reproduced from Romanova et al. (2006) is shown in Figure 1.15.

We shall now move to a brief discussion of the jet launching mechanism.

1.7 Jet launching

The mechanism which ejects and collimates disk material into a jet beam is yet to be completely understood. Even for the closest sources, the process occurs on a scale too small for the current generation of telescopes to resolve. From the information that observations have gleaned, line profiles show both inflow and outflow in the region around young stars. Hα profiles typically show a double-peaked structure created by

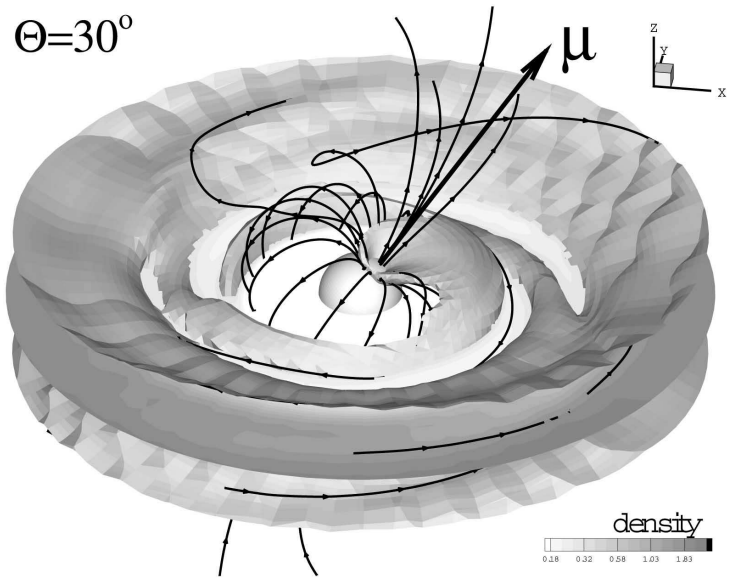

Figure 1.15: Reproduction of Fig.5 from Romanova et al. (2006) showing the stellar magnetic field threading the accretion disk and disk material flowing onto the central protostar through accretion columns.

an absorption dip over the broad profiles. e.g. Hα line profiles observations by Hamilton et al. (2005) of the pre-main sequence eclipsing binary, KH-15D, revealed a 50–60 kms^{-1} redshifted Hα absorption lines interpreted as an accretion flow, in addition to a -350 to +350 kms^{-1} broad emission profile assumed to be an outflow.

Astrophysical jets occur in many forms suggesting the launching mechanism is a robust process. On the smallest scales are the phenomena of solar spicules (e.g. Yamauchi et al., 2004) and on the largest scales are Extra Galactic Radio Jets (e.g. Bagchi et al., 2007). In both cases, these jets are all believed to be launched and collimated by magnetic fields.

The process behind how accretion disk material is directed into collimated jets is still uncertain, mainly due to the existence of several feasible theories. The original theories attempted to explain the launching mechanism by purely hydrodynamic mechanisms. Examples include the creation of a boundary layer shock due to the differences in the velocity between the accreting material with the stellar surface, leading to a disruption

in hydrostatic equilibrium and in turn, an acceleration in the vertical direction perpendicular to the accretion disk (Torbett, 1984). Another model envisaged the collimation of the stellar or disk wind by a dense circumstellar environment through a series of oblique shocks directing a flow perpendicularly from the disk plane. The subsequent cooling of the shocked gas would result in collimated jets (Smith, 1986; Mellema & Frank, 1997).

Today, magnetohydrodynamic models are receiving the most attention. A magneto-centrifugal launch mechanism could be assumed from evidence of jet beam rotation which has been recently detected by Hubble Space Telescope observations with the Space Telescope Imaging Spectrograph (STIS) instrument. The rotation was inferred from asymmetries in the measured Doppler shifts across the jet beam at distances less than 100AU from the source stars. The sources so far studied include the optical DG Tauri outflow (Bacciotti et al., 2002), jets from the T Tauri stars TH28, RW Aur, and LkHα (Coffey et al., 2004) and DG Tau, CW Tau, TH28 (Coffey et al., 2007). In the later study, optical radial velocity shifts of (10–25)$\pm$5 km s^{-1} and lower velocity shifts of 10$\pm$5 km s^{-1} were found in the near ultra-violet wavelength range. The jet rotation is assumed to be a product of a magneto-centrifugal launching mechanism which is is based on the disk-wind theory. However, accounting for the jet rotation as due to the magnetocentrifugal acceleration model has yet to be universally accepted. Such rotational signatures could be accounted for by other theories (e.g. Soker, 2005, 2007).

However, due to their current prominence, the two main MHD launch mechanisms, the disk-wind and x-wind models, will be briefly mentioned below.

1.7.1 Disk-wind model

The disk-wind launching model was first proposed by Blandford & Payne (1982) and has been the focus of much development.

In the basic disk-wind model we imagine the entire accretion disk being heated by

the central protostar and thus behaving as a plasma. The stellar magnetic field can then thread directly through the disk. Within the Alfvén distance, a poloidal magnetic field dominates and plasma is dragged by the magnetic field which co-rotates at the Keplerian rotation rate of the disk. From the interplay between the centrifugal force of rotation and the poloidal magnetic field, material may be channeled from the disk out along the poloidal magnetic field lines, as in the beads-on-a-string analogy. A calculation was made by Blandford & Payne (1982) which states that in order for the centrifugal force on a packet of material at a certain point to overcome its gravitational attraction to the protostar, the poloidal magnetic field component must make an angle of at least 30° to the vertical at the point, (see Figure 1.16). It is believed that the critical angle of 30° can be reached near the inner edge of the accretion disk where the material is exposed to the most ionising radiation and possess the fastest rotation rate.

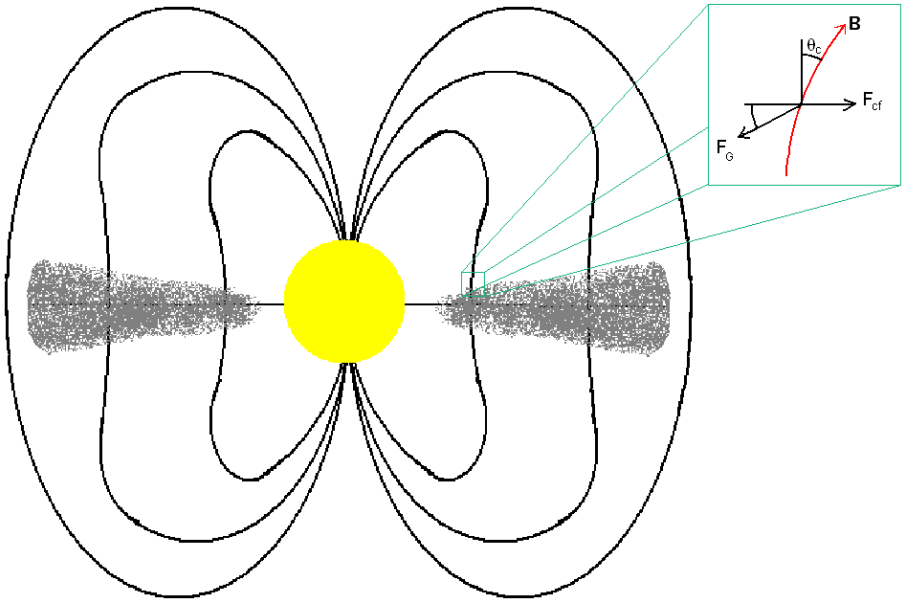

Figure 1.16: A simplified diagram showing the cross section through a protostar and accretion disk. The magnetic field lines from the star are bent as they pass through the accretion disk. The inset shows the components of the gravitational force, F_G, and the outward centrifugal force, F_{cf}, and the critical angle, θ_c. The critical angle, which must be greater than 30°, is measured between the poloidal magnetic field line a line perpendicular to the disk surface.

Figure 1.16 suggests material is ejected away from the rotation axis and not parallel to it as observed. Beyond the Alfvén distance the poloidal field weakens and the inertia of the rotating plasma spiraling around the rotation axis begins to dominate. This motion converts the poloidal field into a strong toroidal field. The resulting magnetic hoops create a helical structure which act as a funnel to channel material along the rotation axis and ultimately create a collimated jet (Smith, 2004).

The disk-wind model may be capable of launching molecular jets if the material is shielded against ionising radiation from the central source.

1.7.2 X-wind

The similar and competing theory to the disk-wind model is the X-wind model which was first proposed by Shu et al. (1988). The fundamental difference with this model compared to the disk-wind model is that the magnetic field does not thread through the accretion disk. The stellar magnetic field is squeezed and forced through the inner edge of the disk. However, this region is subjected to the most intense ionising radiation from the stellar photosphere so that the inner edge behaves as a plasma and gets threaded by the strong magnetic field lines (see Figure 1.17). This helps to anchor the protostar

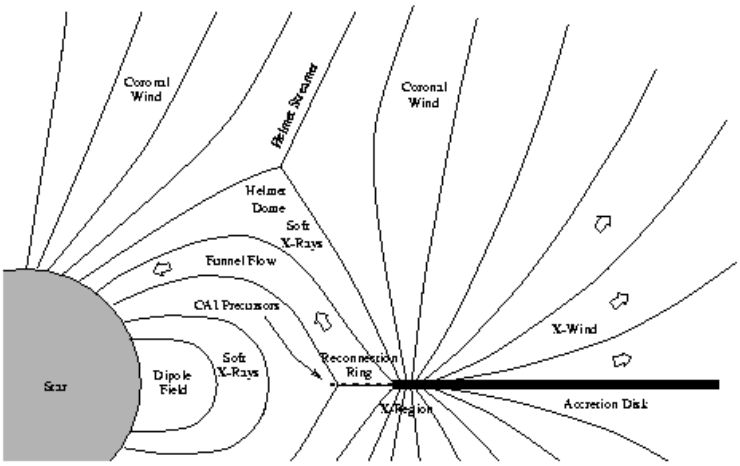

Figure 1.17: A schematic diagram of the X-wind model (Reproduced from Shu et al., 1994)

and prevent a build up of angular momentum taking it to break-up velocities. The anchoring occurs at the so-called 'X-point' where the protostar and the inner edge of the disk co-rotate at an equal angular velocity. Material at the X-point can either be channeled along field lines directly onto the stellar surface or flung outward along the open field lines. In contrast to the disk-wind model, which is capable of removing excess angular momentum over many radii along the disk, the X-wind model can only remove the remaining angular momentum from the co-rotation radius. The strength of the outflowing material increases from the disk towards the stellar poles. The overall effect is that angular momentum is removed from the X-point and channeled into a jet and outflow (Smith, 2004).

The X-Wind model may be expected launch atomic jets as the material originates close to the central source. However, molecular gas could become entrained by the X-Wind jet soon after launching.

For the numerical protostellar jet simulations presented in the following chapters, we will assume a perfectly collimated jet has been created and accelerated somewhere off the computational domain. Such an assumption would tend towards an idealised version of an X-wind jet launching mechanism which directly accounts for a high density collimated flow of material propagating along the rotation axis of the protostellar system. Our simulations ignore the presence of a wider angle, slower moving, and less dense flow which the X-wind model also predicts. We do not expect the presence of this additional component to effect the morphology of the resulting outflow which is mainly created and dominated by the downstream bowshock.

Chapter 2

Numerical Simulations and the ZEUS-3D Code

Numerical simulations have contributed significantly to the understanding of the star formation process and the phenomenon of protostellar jets/outflows. Whereas observers glimpse only a snapshot in time of a system that develops and evolves on timescales of millions of years, numerical simulations can gain access to thousands or tens of thousands of years of evolution in conditions that cannot be emulated in a laboratory. Numerical simulations combine theory in the form of physical equations and observations in the form of input parameters. The computer then evolves the system with time. The resulting simulated data can be post-processed into the form which observers obtain from their telescopes. Matches between simulation and observation suggest the underlying theory of the physical equations is consistent and hence a greater understanding is gleaned of the actual astrophysical processes involved.

The numerical code used for the work presented in this thesis is called ZEUS-3D. In this chapter we shall describe the basic principles used in the code, namely the equations of hydrodynamics and how they are solved using the method of finite differencing. We shall then see how the molecular cooling functions are combined to the basic code,

making ZEUS-3D particularly suitable for performing protostellar jet simulations.

ZEUS-3D is a prominent astrophysical fluid dynamics code. Numerous iterations of what developed into the ZEUS code have existed since 1980 with each new version receiving significant expansions, de-bugging and improvements. A detailed description of the physics within the ZEUS-2D version of the code is contained within three papers: Stone & Norman (1992a), Stone & Norman (1992b) and Stone et al. (1992). ZEUS-3D contains the same basic algorithms as ZEUS-2D but expanded with the capability to perform full three dimensional calculations.

The latest official base version of ZEUS-3D by one of the original authors is version 3.5 which was released in May 2008. It is freely available for use by the scientific community and can be downloaded from the Institute of Computational Astrophysics (ICA) at St. Mary's University, Nova Scotia, Canada [1]. Older versions are available from the Laboratory for Computational Astrophysics (LCA) at the University of California [2]. The version of ZEUS-3D used in this thesis was built around version 3.4.1 and has incorporated various bug fixes over the years and the official update to version 3.4.2. In addition, it has diverged from the official releases by receiving a major in-house developed molecular cooling and chemistry module. The addition of this module makes our version of ZEUS-3D particularly suitable for protostellar jet simulations.

Apart from simulating protostellar jets, the ZEUS family of codes have been used in many areas in astrophysics such as, for example, modelling turbulence in molecular clouds (Pavlovski et al., 2002), modelling the ablation of meteors in the Venusian atmosphere (Korycansky et al., 2000) and the modelling of 3D solar coronae (Abbett & Fisher, 2003).

In summary, ZEUS-3D incorporates the following features:

- Fixed grid, time-explicit Eulerian code for 1D, 2D, 2.5D or 3D simulations.

[1] `http://www.ica.smu.ca/zeus3d/`
[2] `http://lca.ucsd.edu/portal/software/zeus-3d`

- Cartesian, cylindrical and spherical coordinate systems based on a covariant formulism.
- First order donor cell, second order van Leer, and third order piecewise parabolic advection schemes.
- von Neumann Richtmyer artificial viscosity.
- Method of Characteristics Magnetohydrodynamics (MHD) approach with Constrained Transport algorithm (MOC-CT).
- Algorithms for ambipolar diffusion.
- Molecular chemistry and cooling routines with semi-implicit energy equation.

ZEUS-3D is a parallel code meaning it can perform calculations simultaneously on multiple Central Processing Unit's (CPUs) during a single simulation. It was written to be optimised for 'shared memory' systems, the type found in supercomputers. Shared memory systems typically consist of custom designed CPUs and Random Access Memory (RAM) modules combined in such a way that each CPU has access to all the available RAM of the supercomputer. This allows for substantially large simulations to be performed where the problem area is divided between the CPUs which can all simultaneously read and write data to the pooled RAM. The disadvantages of supercomputers are the high running costs and expensive specialised architecture which quickly dates.

With the vast advances in semiconductor technology in recent years and accompanying price decreases, it has been found that 'distributed memory' or 'clusters' have become a very cost effective way to perform large calculations. They are based around standard desktop computer components where motherboards containing RAM and a CPU are referred to as 'nodes' and all nodes are networked together. Each node only has direct access to its local RAM but standardised instruction sets such as Message Passing Interface (MPI) automatically control the sharing of data between nodes and

compile the programs in such a way as to minimise the amount of data sharing required. These developments have led to ZEUS-MP (Norman, 2000), a version optimised for such distributed memory systems. The latest version of ZEUS-MP is Version 2.1.2 and is similarly available from the LCA website.

Today, ZEUS-3D is but one code among many. ZEUS-3D is a fixed grid code meaning every zone in the computational domain is of equal size (though it does allow for ratioed grids and a limited grid tracking ability, see Section 2.4). Simulations performed on fixed grids may not be considered the most efficient as an equal amount of computational time must be spent over every zone during each timestep. This gives equal precedence to zones on the grid where there is little or no flow occurring as to the zones which are tracking important flows and shockwaves. The development of Adaptive Mesh Refinement (AMR) codes have redressed this limitation by employing the capability of applying finer grid 'meshes' only where needed and so effectively providing large resolution increases without requiring significant additional resources. Examples of AMR codes include the FLASH code (Plewa, 2003), which also differs from ZEUS-3D by using finite *volume* method rather than the finite difference method, and the Pluto code (Mignone et al., 2007), which is also finite volume but written exclusively in C rather than Fortran, and AstroBEAR (Cunningham et al., 2007), a code focusing on high resolution shock capturing MHD.

Fundamentally different types of fluid dynamics code are Smoothed Particle Hydrodynamics (SPH) codes. Instead of calculating the changing quantities within grid zones, SPH codes track the movement and evolution on many virtual particles. Like AMR, they effectively apply higher resolution in important regions where dense regions of a simulation would consist of many closely spaced particles and in low density regions, the particles would be sparsely spaced. An example of an SPH code is Gadget-2 (Springel, 2005). Although SPH codes they have been used to successfully simulate protostellar jets (e.g. de Gouveia dal Pino & Benz, 1993), a disadvantage of SPH codes has been the difficulty of implementing MHD and radiative transfer.

Now we shall now look at the core of ZEUS-3D (and that of any computational fluid dynamics code), the equations of hydrodynamics.

2.1 The equations of hydrodynamics and their derivations

The very core of numerical simulations are the equations of hydrodynamics (HD). They state the following three important physical principles:

1. The conservation of mass.
2. The conservation of momentum.
3. The conservations of energy.

The principles are presented as a set of coupled hyperbolic partial differential equations (PDE's). Such equations would be difficult to solve directly by analytical means but are ideal for solving by numerical means (See Section 2.3.1). A commonly expressed form of the equations of hydrodynamics are as follows:
The conservation of mass,

$$\frac{D\rho}{Dt} + \rho\nabla \cdot \mathbf{V} = 0 \tag{2.1}$$

the conservation of momentum,

$$\rho\frac{Dv}{Dt} = -\nabla p \quad (-\rho\nabla\Phi) \tag{2.2}$$

and the conservation of internal energy,

$$\rho\frac{D}{Dt}\left(\frac{e}{\rho}\right) = -p\nabla \cdot v \tag{2.3}$$

where $\frac{D}{Dt}$ is the substantial derivative,

$$\frac{D}{Dt} = \frac{\partial}{\partial t} + \mathbf{V} \cdot \nabla \tag{2.4}$$

and where ρ is the density, v is the velocity, p is the pressure, Φ is the gravitational potential, and e is the internal energy density.

The equations need to be closed by the equation of state which is simply the ideal gas equation,

$$p = (\gamma - 1)\, e \tag{2.5}$$

where γ is the specific heat ratio.

Gravity is not implemented in the simulations of this thesis but may be through the bracketed term of Equation 2.2 and the 'Poisson equation',

$$\nabla^2 \Phi = 4\pi G \rho \tag{2.6}$$

where G is the gravitational constant (Stone & Norman, 1992a).

The form of the above equations are known as the differential and non-conservation form of the Euler equations. The Euler equations are a simplified form of the full equations of hydrodynamics, or Navier-Stokes equations. The Navier-Stokes equations possess additional terms to account for viscosity. In some astrophysical situations we can assume the viscosity is very small so that the Navier-Stokes equations can be approximated as the Euler equations. Both the Navier-Stokes and Euler equations view a fluid on the macroscopic level. They ignore the microscopic level of colliding particles (electrons and atoms) as it assumes the mean free path of the particles is much shorter than the length scale of the entire system.

The following sections will derive the equations of hydrodynamics, based on Anderson (1995), in order to provide a deeper understanding of their physical basis.

2.1.1 Conservation of mass

The conservation of mass, also known as the Continuity Equation, states that mass must be conserved. It can be derived in the following way.

We assume a computational domain which is divided into an array of elements or grid zones. In three dimensions, each zone could be considered an infinitesimally small volume in the shape of a cube. Over the course of a simulation, a fluid 'flows' through the cube. We assign dimensions dx, dy and dz to the cube and imagine flow propagating from left to right so that there is a net inflow of mass into the left hand face of the cube and a net outflow of mass out of the right hand face. (See Figure 2.1 for a basic diagram of the element with the mass flows in the x-direction labelled.)

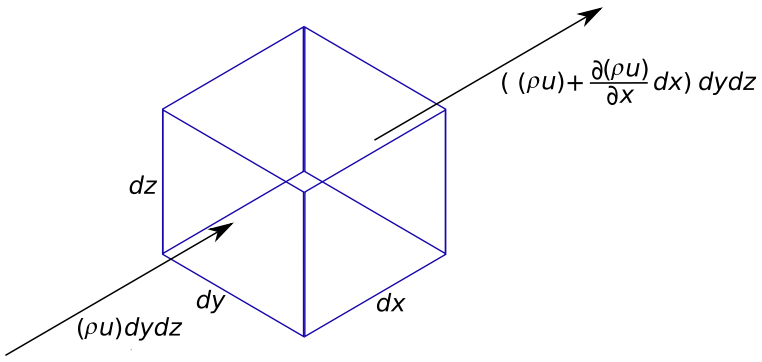

Figure 2.1: A pictorial view of infinitesimally small grid element fixed in space with the x-direction mass flows labelled.

The total mass flowing into the left-hand side through the cube face of area $dydz$ is simply,

$$(\rho u)\, dydz \tag{2.7}$$

where ρ is the density of the fluid and u is component of the fluid's velocity in the x-direction.

After flowing through the volume for a distance dx, the total mass flowing out of

the right-hand face is,

$$\left(\rho u + \left(\frac{\partial(\rho u)}{\partial x}\right) dx\right) dydz \tag{2.8}$$

where $\frac{\partial(\rho u)}{\partial x}dx$ is the change in mass flux between the left face to right face. For mass to be conserved, these two quantities must be equal. Therefore, the net outflow is the difference between Equation 2.8 and Equation 2.7,

$$\begin{aligned}\left(\rho u + \left(\frac{\partial\left(\rho u\right)}{\partial x}\right)\right) dydz - \left(\rho u\right) dydz = 0 \\ \frac{\partial\left(\rho u\right)}{\partial x} dydz = 0\end{aligned} \tag{2.9}$$

In a similar fashion, the net flow in the y-direction through the $dxdz$ faces would be,

$$\frac{\partial\left(\rho v\right)}{\partial x} dxdz = 0 \tag{2.10}$$

and the net flow in the z-direction through the $dxdy$ faces would be,

$$\frac{\partial\left(\rho w\right)}{\partial x} dxdy = 0 \tag{2.11}$$

where v and w are the components of the flow velocity in the y- and z-directions respectively.

The *total* mass flow through the entire cube is then the sum of the contributions from the three directions. Summing Equations 2.9, 2.10 and 2.11 gives,

$$\left(\frac{\partial(\rho u)}{\partial x} + \frac{\partial(\rho v)}{\partial y} + \frac{\partial(\rho w)}{\partial z}\right) dxdydx \tag{2.12}$$

Mass must be conserved, therefore the total mass outflow from the volume, must equal the rate of the decrease of mass inside the volume,

$$-\frac{\partial \rho}{\partial t}\left(dxdydz\right) \tag{2.13}$$

where mass is equal to density times volume.

Equating Equations 2.12 and 2.13 gives,

$$\left(\frac{\partial(\rho u)}{\partial x}+\frac{\partial(\rho v)}{\partial y}+\frac{\partial(\rho w)}{\partial z}\right)dxdydx=-\frac{\partial\rho}{\partial t}(dxdydz) \tag{2.14}$$

which, by canceling the volume terms, simplifies to,

$$\frac{\partial\rho}{\partial t}+\left(\frac{\partial(\rho u)}{\partial x}+\frac{\partial(\rho v)}{\partial y}+\frac{\partial(\rho w)}{\partial z}\right)=0 \tag{2.15}$$

The second group of terms can be simplified by introducing $\nabla\cdot\mathbf{V}$ where $\mathbf{V}$ is the velocity vector in the three dimensions and ∇ is the vector operator ($\nabla=\mathbf{i}\frac{\partial}{\partial x}+\mathbf{j}\frac{\partial}{\partial y}+\mathbf{k}\frac{\partial}{\partial z}$),

$$\nabla\cdot\mathbf{V}=\frac{\partial u}{\partial x}+\frac{\partial v}{\partial y}+\frac{\partial w}{\partial z} \tag{2.16}$$

After substituting Equation 2.16 into Equation 2.15 we obtain the differential form of the continuity equation in conservation form as used by ZEUS-3D,

$$\frac{\partial\rho}{\partial t}+\nabla\cdot(\rho\mathbf{V})=0 \tag{2.17}$$

The conservation form of Equation 2.17 can be easily interchanged to the non-conservation or Lagrangian form. First we make use of the following vector identity,

$$\nabla\cdot(\rho\mathbf{V})=(\rho\nabla\cdot\mathbf{V})+(\mathbf{V}\cdot\nabla\rho) \tag{2.18}$$

Substituting the second term of Equation 2.17 with the vector identity of Equation 2.18 we obtain,

$$\begin{aligned}\frac{\partial\rho}{\partial t}+(\rho\nabla\cdot\mathbf{V})+(\mathbf{V}\cdot\nabla\rho)&=0\\ \frac{\partial\rho}{\partial t}+(\mathbf{V}\cdot\nabla\rho)+(\rho\nabla\cdot\mathbf{V})&=0\end{aligned} \tag{2.19}$$

Finally, the first two terms of Equation 2.19 can replaced with Equation 2.4, the sub-

stantial derivative, repeated here,

$$\frac{D}{Dt} = \frac{\partial}{\partial t} + (\mathbf{V} \cdot \nabla) \tag{2.20}$$

to obtain the popular *non*-conservation form of the continuity equation,

$$\frac{D\rho}{Dt} = \rho \nabla \cdot \mathbf{V} = 0 \tag{2.21}$$

2.1.2 Conservation of momentum

The momentum conservation equation is based on Newton's 2nd law, $F = ma$, which states, in words, that the force, F, on an object equals its mass, m, times the acceleration, a, imposed upon it. The momentum equation can be derived by following the previous train of thought by considering the effect of Newton's 2nd law upon the small cubic infinitesimal volume.

The total mass of the cube is the density times the volume,

$$m = (\rho) dx dy dz \tag{2.22}$$

Acceleration is defined as the rate of change of velocity. Considering only the x-direction for simplicity, the acceleration in the x-direction, a_x, is given as,

$$a_x = \frac{Du}{Dt} \tag{2.23}$$

where, as before, u is the component of velocity in the x-direction.

By combining Equation 2.22 and 2.23 we have derived the right hand side of the $F = ma$ equation for the x-direction,

$$F_x = \rho \frac{Du}{Dt} dx dy dz \tag{2.24}$$

Now we must consider the forces acting on the infinitesimally small volume, again only considering the x-direction for simplicity.

As we are only deriving the Euler form of the equations for an inviscid flow, there are no viscous inducing stress or strain forces required thus simplifying the derivation. We are also ignoring forces due to gravity. The only forces we need to calculate are due to the pressures acting perpendicular to each cube face in the three spatial dimensions. (See Figure 2.2 for a diagram of the infinitesimal fluid element with the forces acting in the x-direction.)

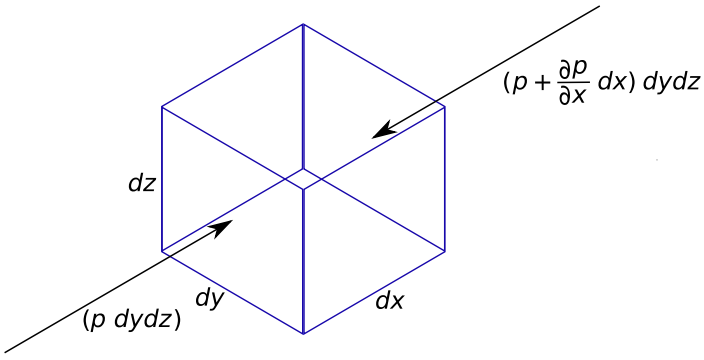

Figure 2.2: A pictorial representation of the infinitesimally small volume with the x-direction momentum flows labeled.

As seen in Figure 2.2 there is a pressure, p, acting on the left hand $dydz$ face of the cube and a pressure of $(\mathrm{p} + \frac{\partial p}{\partial x}dx)$ acting on the right hand $dydz$ face in the negative x-direction. The total force in the x-direction is then the difference of the pressures between the two faces,

$$\begin{aligned}\left(p - \left(p + \frac{\partial p}{\partial x}dx\right)\right) dydz = 0 \\ -\frac{\partial p}{\partial x}dxdydz = 0\end{aligned} \tag{2.25}$$

Now we can now equate the right hand side of Equation 2.24 with Equation 2.25 representing the force, F, while including the terms which would occur in the y- and

z-directions,

$$\rho\left(\frac{Du}{Dt}+\frac{Dv}{Dt}+\frac{Dw}{Dt}\right)dxdydz=-\left(\frac{\partial p}{\partial x}+\frac{\partial p}{\partial y}+\frac{\partial p}{\partial z}\right)dxdydz \tag{2.26}$$

The volume terms cancel on both sides of the equation. On the left hand side we can combine the three separate velocity components into the total velocity vector, $\mathbf{V}$. The terms on the right hand side can be substituted with the vector operator, ∇, $(\nabla = \mathbf{i}\frac{\partial}{\partial x}+\mathbf{j}\frac{\partial}{\partial y}+\mathbf{k}\frac{\partial}{\partial z})$. We have now arrived at the non-conservation form of the momentum equation,

$$\rho\frac{D\mathbf{V}}{Dt}=-\nabla p \tag{2.27}$$

As with the continuity equation, the momentum equation can be interchanged between conservation and non-conservation form using the substantial derivative and a vector identity.

Using the substantial derivative, the left hand side of Equation 2.27 can be expressed as,

$$\rho\frac{D\mathbf{V}}{Dt}=\rho\frac{\partial\mathbf{V}}{\partial t}+\rho\mathbf{V}\cdot\nabla\mathbf{V} \tag{2.28}$$

The partial derivative term of Equation 2.28 can be expanded using the following law,

$$\begin{aligned}\frac{\partial(\rho\mathbf{V})}{\partial t}&=\rho\frac{\partial\mathbf{V}}{\partial t}+\mathbf{V}\frac{\partial\rho}{\partial t}\\ \rho\frac{\partial\mathbf{V}}{\partial t}&=\frac{\partial(\rho\mathbf{V})}{\partial t}-\mathbf{V}\frac{\partial\rho}{\partial t}\end{aligned} \tag{2.29}$$

The second term on the right hand side of Equation 2.28 can be modified using the following vector identity,

$$\begin{aligned}\nabla\cdot(\rho\mathbf{V}\ \mathbf{V})&=\mathbf{V}\nabla\cdot(\rho\mathbf{V})+\rho\mathbf{V}\cdot\nabla\mathbf{V}\\ \rho\mathbf{V}\cdot\nabla\mathbf{V}&=\nabla\cdot(\rho\mathbf{V}\ \mathbf{V})-\mathbf{V}\nabla\cdot(\rho\mathbf{V})\end{aligned} \tag{2.30}$$

By substituting the alternative terms of Equation 2.29 and 2.30 into the right side of

Equation 2.28 we obtain,

$$\begin{aligned}
&\frac{\partial(\rho\mathbf{V})}{\partial t} - \mathbf{V}\frac{\partial \rho}{\partial t} + \nabla \cdot (\rho\mathbf{V}\ \mathbf{V}) - \mathbf{V}\nabla \cdot \rho\mathbf{V} \\
&\frac{\partial(\rho\mathbf{V})}{\partial t} - \mathbf{V}\left[\frac{\partial \rho}{\partial t} + \nabla \cdot (\rho\mathbf{V})\right] + \nabla \cdot (\rho\mathbf{V}\ \mathbf{V}) \\
&\frac{\partial(\rho\mathbf{V})}{\partial t} + \nabla \cdot ((\rho\mathbf{V})\mathbf{V})
\end{aligned} \tag{2.31}$$

where the terms placed in the square brackets was the continuity equation and thus could be set to zero.

The final form of the momentum equation in conservation form is obtained by substituting Equation 2.31 as the left hand side of Equation 2.27,

$$\frac{\partial(\rho\mathbf{V})}{\partial t} = -\nabla \cdot ((\rho\mathbf{V})\mathbf{V} - \nabla p \tag{2.32}$$

2.1.3 Conservation of energy

To derive the conservation of energy equation we again consider the infinitesimal cubic fluid element. The total rate of change of energy inside the element equals the rate of work done on the element plus the total flow of heat through the element. A graphical representation of the energy related terms required for our derivation are displayed in Figure 2.3.

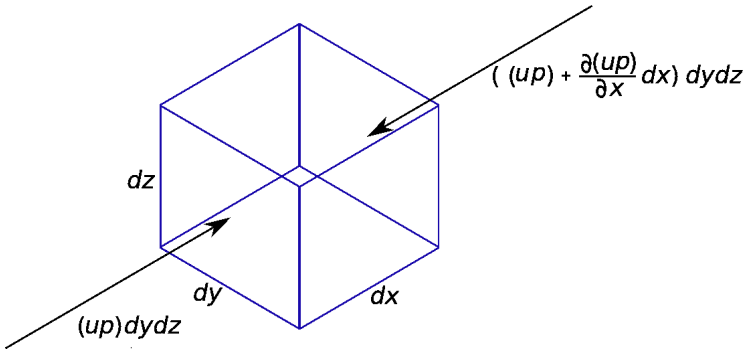

Figure 2.3: A pictorial representation of the infinitesimally small volume with the x-direction energy flows labeled.

An internal energy arises from the motion of the atoms and molecules within the fluid element and is related to the First Law of Thermodynamics. Considering the internal energy, e, the rate of change of energy inside the fluid elements volume can be written as,

$$\frac{D}{Dt}(e)\ \ \rho\ dxdydz \tag{2.33}$$

For the simulations we perform in ZEUS-3D, we need only consider the work done by the external pressure in acting upon the cubic volume. Work equals force (or equivalently pressure) by distance. The work done by pressure in the x-direction can be expressed, analogous to the previous derivations, as,

$$\begin{aligned}\left(up - \left(up + \frac{\partial(up)}{\partial x}dx\right)\right)dydz = 0\\ -\frac{\partial(up)}{\partial x}dxdydz = 0\end{aligned} \tag{2.34}$$

Again we can expand the above equation to include all three spatial directions,

$$-\left(\frac{\partial(up)}{\partial x} + \frac{\partial(vp)}{\partial y} + \frac{\partial(wp)}{\partial z}\right)dxdydz \tag{2.35}$$

This can simplified as was seen in the continuity equation derivation by replacing the three velocity components with the vector operator shown in Equation 2.16 to obtain,

$$-p\nabla \cdot V dxdydz \tag{2.36}$$

Equating Equation 2.33 with Equation 2.36 we obtain the expression for the energy equation in *non*-conservation form,

$$\rho\frac{D}{Dt}e = -p\nabla \cdot V \tag{2.37}$$

Once again, the *non*-conservation form can be manipulated to conservative form following the same method as in the momentum equation derivation. Using the sub-

stantial derivative, the left hand side of Equation 2.37 can be written as,

$$\rho\frac{De}{Dt} = \rho\frac{\partial e}{\partial t} + \rho\mathbf{V}\cdot\nabla e \tag{2.38}$$

The partial derivative term of Equation 2.38 can be expanded as and written as,

$$\rho\frac{\partial e}{\partial t} = \frac{\partial(\rho e)}{\partial t} - e\frac{\partial \rho}{\partial t} \tag{2.39}$$

The second term on the right hand side of Equation 2.38 can be modified using the following vector identity,

$$\nabla\cdot(\rho e\mathbf{V}) = e\nabla\cdot(\rho\mathbf{V}) + \rho\mathbf{V}\cdot\nabla e \tag{2.40}$$

re-arranged to,

$$\rho\mathbf{V}\cdot\nabla e = \nabla\cdot(\rho e\mathbf{V}) - e\nabla\cdot(\rho\mathbf{V}) \tag{2.41}$$

By substituting the alternative terms of Equation 2.41 into Equation 2.38 we get,

$$\begin{aligned}
\rho\frac{De}{Dt} &= \frac{\partial e}{\partial t} - e\nabla\cdot(\rho\mathbf{V}) + \nabla\cdot(\rho e\mathbf{V}) \\
\rho\frac{De}{Dt} &= \frac{\partial(\rho e)}{\partial t} - e\left[\frac{\partial \rho}{\partial t} + \nabla\cdot(\rho\mathbf{V})\right] + \nabla\cdot(\rho e\mathbf{V}) \\
\rho\frac{De}{Dt} &= \frac{\partial(\rho e)}{\partial t} + \nabla\cdot(\rho e\mathbf{V})
\end{aligned} \tag{2.42}$$

where, again, the terms within the square brackets was the continuity equation an thus could be set to zero.

Finally, the conservation form of the Euler internal energy conservation equation is obtained by substituting Equation 2.42 into Equation 2.37,

$$\frac{\partial(\rho e)}{\partial t} + \nabla\cdot(\rho e\mathbf{V}) = -p\nabla\cdot\mathbf{V} \tag{2.43}$$

(Anderson, 1995). This completes the derivation of the equations of hydrodynamics.

2.2 Specific heat ratio

The specific heat ratio, γ, is an important input parameter of ZEUS-3D. It determines the behaviour of the 'fluids' in our simulations. In its most basic form it can be defined as,

$$\gamma = \frac{c_p}{c_v} \tag{2.44}$$

or the ratio of the specific heat at constant pressure, c_p, to the specific heat at constant volume, c_v.

We can formulate the specific heat ratio to be in terms of one variable which allows the straightforward set-up of various compositions of stellar gas. The calculation is based around the most abundant element, hydrogen. The total number of hydrogen *nuclei* present per unit volume equals twice the number of hydrogen molecules plus the number of hydrogen atoms,

$$n(H_{nuclei}) = 2 \times n(H_2) + n(H_{atoms}) \tag{2.45}$$

In terms of $n(H_{nuclei})$, the number density of hydrogen *molecules* is,

$$n\left(H_2\right) = fn(H_{nuclei}) \tag{2.46}$$

where f is the fraction of the molecular hydrogen abundance (it ranges from 0 for fully dissociated to 0.5 for fully molecular). Substituting this into Equation 2.45, we get,

$$n(H_{nuclei}) = 2 \times fn(H_{nuclei}) + n(H_{atoms}) \tag{2.47}$$

We re-arrange so as to be in terms of H atoms,

$$\begin{aligned} n(H_{atoms}) &= n(H_{nuclei}) - 2 \times fn(H_{nuclei}) \\ n(H_{atoms}) &= (1 - 2f)\, n(H_{nuclei}) \end{aligned} \tag{2.48}$$

and simplify the notation to,

$$n(H) = (1 - 2f)\, n \tag{2.49}$$

Helium, He, is the second most abundant element after Hydrogen. It constitutes about 10% of the ISM compared to 90% hydrogen and thus we include its contribution as,

$$n(He) = 0.1n \tag{2.50}$$

Heavier elements occur only in trace amounts compared to the number of hydrogen and helium atoms so further additions would have negligible effects upon the specific heat ratio. (The heavier elements of Carbon and Oxygen and the most important molecules which they occur in are considered in the code through the molecular chemistry and cooling routines (see Section 2.5) as they are important tracers and provide useful diagnostic lines.)

We now sum the components as the total number of particles per unit volume, $< n >$,

$$\begin{aligned} < n > &= n(H) + n(H_2) + (He) \\ &= (1 - 2f)n + fn + 0.1n \\ &= (1.1 - f)n \end{aligned} \tag{2.51}$$

The total specific heat, c_v, of the system will be given as the sum of the specific heats of the individual components,

$$c_v = c_v\,(H) + c_v\,(H_2) + c_v\,(He) \tag{2.52}$$

Hydrogen atoms and Helium posses three degrees of freedom; translational degrees in the three spatial dimensions. Molecular hydrogen possesses five degrees of freedom; three translational plus two rotational. (Two additional vibrational degrees are ignored as they occur at high temperatures greater than 6,000K where molecular hydrogen

would already be fully dissociated.)

Equation 2.52 can be re-written as,

$$c_v = \frac{3}{2}k_B\frac{n\left(H\right)}{\langle n\rangle} + \frac{5}{2}k_B\frac{n\left(H_2\right)}{\langle n\rangle} + \frac{3}{2}k_B\frac{n\left(He\right)}{\langle n\rangle} \tag{2.53}$$

where k_B is the Boltzmann constant.

To obtain the specific heat at constant volume in terms of the molecular fraction we substitute Equations 2.46, 2.49, 2.50 and 2.51 into Equation 2.53 and after some algebraic manipulation we obtain the following equation,

$$c_v = \frac{3.3 - f}{2.2 - 2f}k_B \tag{2.54}$$

It can be expressed to be in terms of the specific heat ratio, γ, through further algebraic manipulation and using the fact that $c_p = c_v + k_B$,

$$\begin{aligned}\gamma &= \frac{c_p}{c_v} \\ &= \frac{c_v + k_B}{c_v} \\ &= \frac{5.5 - 3f}{3.3 - f}\end{aligned} \tag{2.55}$$

From Equation 2.55 we see that if $f = 0$ (an atomic medium), then $\gamma = \frac{5}{3}$ and if $f = 0.5$ (fully molecular), $\gamma = \frac{10}{7}$. These are the values we use in our simulations for the molecular and atomic gas compositions respectively.

2.3 Solving the hydrodynamic equations numerically

In order to solve Equations 2.1 to 2.4 numerically, ZEUS-3D uses the method of finite-differencing with time-explicit multi-step operator-splitting. Finite-differencing is a popular method to solve differential equations numerically. The equations of hydrodynamics are simplified into algebraic equations and solved over a fixed reference array of

grid points. Time-explicit means that during each time step, new values are calculated for the next step using only existing information from the current time step. Operator-splitting means that the solutions to the PDEs are broken into parts with each 'part' being a single term from the equations.

2.3.1 Finite-differencing

The basics of finite-differencing is based on the mathematical Taylor series expansion. A Taylor series provides an approximation of a function from an infinite series of derivatives from a single point. An example of a Taylor series is as follows,

$$u_{i+1,j} = u_{i,j} + \left(\frac{\partial u}{\partial x}\right)_{i,j} \Delta x + \left(\frac{\partial^2 u}{\partial x^2}\right)_{i,j} \frac{(\Delta x)^2}{2} + \left(\frac{\partial^3 u}{\partial x^3}\right)_{i,j} \frac{(\Delta x)^3}{3!} + \left(\frac{\partial^4 u}{\partial x^4}\right)_{i,j} \frac{(\Delta x)^4}{4!} \dots \tag{2.56}$$

where, if $u_{i,j}$ is, for example, the velocity at the point (i, j) of a function $f(x)$, then the velocity at point $u_{i+1,j}$ can be found from the sum of successively higher order partial derivatives of the function at the known point.

When re-arranged, the above equation can give direct solutions to the first partial derivative at the point (i, j), if the value of the neighbouring point $i + 1$ is known,

$$\left(\frac{\partial u}{\partial x}\right)_{i,j} = \frac{u_{i+1,j} - u_{i,j}}{\Delta x} - \left(\frac{\partial^2 u}{\partial x^2}\right)_{i,j} \frac{(\Delta x)}{2} - \left(\frac{\partial^3 u}{\partial x^3}\right)_{i,j} \frac{(\Delta x)^2}{3!} \dots \tag{2.57}$$

In practice, calculating an infinite series is not necessary and approximations of suitable precision may be obtained by using only powers to the first order, i.e.*first order accurate*,

$$\left(\frac{\partial u}{\partial x}\right)_{i,j} = \frac{u_{i+1,j} - u_{i,j}}{\Delta x} + O(\Delta x) \tag{2.58}$$

where $O(\Delta x)$ is known as the truncation error which consists of the higher order partial derivative terms. Without the inclusion of the truncation error, the equation is an approximation to the true answer. Equation 2.58 is also referred to as a first order

accurate *forward* difference equation as it makes use of the proceeding $i+1$ value for its solution. In an analogous fashion, a first order accurate *rearward* difference equation makes use of the preceding $i-1$ value,

$$\left(\frac{\partial u}{\partial x}\right)_{i,j} = \frac{u_{i,j} - u_{i-1,j}}{\Delta x} + O(\Delta x) \tag{2.59}$$

For a better approximation, powers to the second order may be used to obtain a *second order accurate* difference equation. A second order accurate expression can be calculated by subtracting the Taylor series expansion for point $u_{i+1,j}$ in Equation 2.56 from one expanded for point $u_{i-1,j}$. After some algebraic manipulation we get,

$$\left(\frac{\partial u}{\partial x}\right)_{i,j} = \frac{u_{i+1,j} - u_{i-1,j}}{\Delta x} + O(\Delta x)^2 \tag{2.60}$$

where the truncation error is now $O(\Delta x)^2$, implying second order terms are being used to calculate the solution.

We see that Equation 2.60 is an example of a *central* difference equation as it requires information from points $u_{i+1,j}$ and $u_{i-1,j}$. Combinations of forward, rearward and central differencing in both first or second order accuracy lead to six possible equations, though many more could be created if combinations of the j and i directions are used.

For a practical example of the operation of finite-differencing we can consider a basic one-dimensional advection equation,

$$\frac{\partial q}{\partial t} + v\frac{\partial q}{\partial x} = 0 \tag{2.61}$$

which, here, governs the motion of a flux, q, with time, t, and at velocity, v, along direction, x.

As the fluid is flowing in the positive direction ($v > 0$), it is appropriate to use the *rearward* equation (Equation 2.59) for the spatial derivative term which uses the known preceding values along the propagation direction. A *forward* difference approx-

imation (based on Equation 2.58) would be suitable for the time derivative term as we wish to find the solution at the later time. The resulting first order finite difference approximation thus becomes,

$$\frac{q_i^{n+1} - q_i^n}{\Delta t} + v\left(\frac{q_i^n - q_{i-1}^n}{\Delta x}\right) = 0 \tag{2.62}$$

and re-arranged as,

$$q_i^{n+1} = q_i^n - \frac{\Delta t}{\Delta x}\left(q_i^n - q_{i-1}^n\right) \tag{2.63}$$

where the superscript, n, and subscript, i, terms represent time-steps and positions respectively on the x-t plane (see Figure 2.4 and caption for explanation) with point spacings measured by Δt and Δx.

As long as the values of all points at timestep n are initially known, then successive application of Equation 2.63 will calculate the values of all points at the next timestep $n+1$ and so on. This is referred to as a *time marching* solution. The form shown here is first-order *upwind* and is the type used in the operator split source steps of ZEUS-3D.

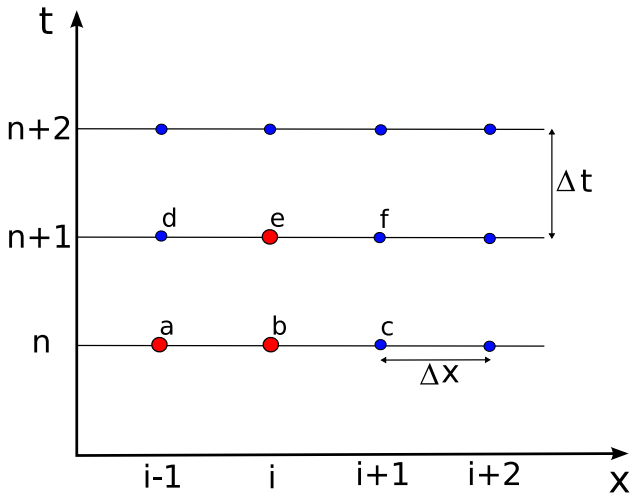

Figure 2.4: An x-t plane displaying a simple 1D spatial depiction of zone points, i, separated by distance Δx along the x-direction and time steps, n, of length Δt along the y-axis. Equation 2.63 *marches* the solution forward in time by one timestep through successive calculations using the known points at the current timestep, i.e.point e is calculated from points a and b, point f is calculated from points b and c etc.

2.3.2 Implicit and Explicit methods

The finite-difference example shown in Equation 2.63 is a time *explicit* equation meaning the value of individual points at the next timestep, $n+1$, can be obtained directly from all the known values of the current timestep, n.

An alternative finite-differencing method is *implicit*. An implicit approach differs in that multiple points must be calculated simultaneously at time step $n+1$ (e.g. in the example of Figure 2.4, points d, e and f may need to be simultaneously calculated from points a, b and c). This shows that, in contrast to the explicit approach, the implicit approach should be very stable thus allow larger time steps, Δt, to be safely performed and leading to fewer overall time steps in the simulation. However, the equations are much more complex to code and the resultant calculations would take longer to solve. In addition, the large timesteps of the implicit approach are not suitable for simulating short time-scale dynamical flows (Stone & Norman, 1992a).

Although the explicit approach is not as computationally intensive, smaller timesteps are required to maintain stable solutions whose size is controlled by the Courant number.

The molecular chemistry and cooling module of ZEUS-3D uses a semi-implicit approach. Here, the old $n-1$ time step values for the temperature and molecular fraction are combined with the current n time step value of density obtained from the ordinary ZEUS-3D routine. For each timestep, a Newton-Raphson method is used repeatedly, re-iterating the temperature and molecular fraction values until they have converged to sufficient accuracy. A limit of a 30% variation to the energy density is imposed between iterations to ensure that the Newton-Raphson method has suitable starting values on which to iterate due to the fact that although it possess good local convergence rates, it is known to have poor global convergence (Pavlovski, 2004).

2.3.3 The Courant condition

An important concept related to time-explicit numerical codes is that of the Courant-Friedrichs-Lewy (CFL) stability condition. The condition places a limit on the size of a computational timestep so that the information may not travel more than one grid zone per timestep. In more general terms, it could be defined so that the numerical domain of dependence must contain the true or physical domain of dependence.

Domains of dependence can be understood from Figure 2.4. The physical domain of dependence of point e in Figure 2.4 would be a triangle containing the red points (points e, a and b) because the solution to be obtained from point e depends solely on points a and b. The numerical domain of dependence must also cover these points. If the numerical domain of dependence was not large enough to cover the values contained at points a and b then insufficient information would exist to compute the solution. The boundaries of the imaginary triangle are known as the *characteristics*.

Another way of understanding the Courant condition is in terms of wave speeds. If the Courant condition was not obeyed, then the sound speed may transmit information over multiple zones in a single timestep, important information such as shock fronts may be skipped and the solution may become progressively incorrect or unstable.

The Courant condition can be defined, in one dimension, as

$$C < \frac{(u + c_s)\Delta t}{\Delta x} \tag{2.64}$$

where C is the Courant number, u is the maximum flow velocity, c_s is the sound speed, Δt is the timestep, and Δx is the zone size. For numerical stability, and thus physically meaningful results, the Courant number, C, is conventionally set as 0.5. It has been shown that for $C < 0.5$, numerical errors can not be further reduced by decreasing the time-step, Δt (e.g. Wrobel & Brebbia, 1991).

In ZEUS-3D, the size of the timestep, Δt, is calculated before each cycle from an

equation based on Equation 2.64. We fix the Courant number as 0.5 in our simulations.

Figure 2.5 is a demonstration to show how the runtime for the code significantly increases for Courant numbers less than 0.5. The test simulations were of low resolution 1000×200 axisymmetric runs with molecular cooling and were run for a simulation time of 1100 years. For $C = 0.5$ the runtime, or 'CPU time', was roughly 31 minutes. For $C = 0.1$ the runtime was over 2 hours to obtain the same result.

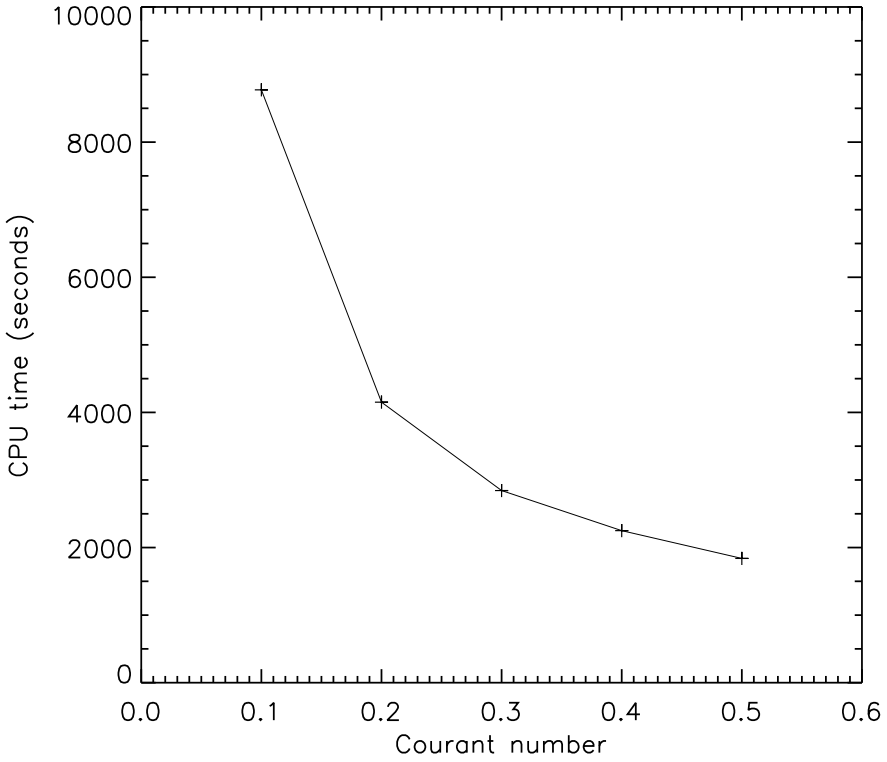

Figure 2.5: An example of how the run-time increases as the Courant number decreases. These results are from a series of 1000×200 zone axisymmetric simulations with molecular cooling routines activated and run for a simulation time of 1100 years. For the standard Courant number of 0.5, the runtime is roughly 30 minutes. When reduced to 0.1, the runtime increases to over 2 hours.

2.3.4 Operator-splitting

The principle of the operator-splitting method is as follows. We consider a partial differential equation,

$$\frac{dx}{dt} = f(x) \tag{2.65}$$

whose operator, $f(x)$, can be split into parts,

$$f(x) = F_1(x) + F_2(x) + F_3(x) + ... \tag{2.66}$$

Each part may be approximated using the term preceding it,

$$\begin{aligned} \frac{x^1 - x^0}{dt} &= F_1\left(x^0\right) \\ \frac{x^2 - x^1}{dt} &= F_2\left(x^1\right) \\ \frac{x^3 - x^2}{dt} &= F_3\left(x^2\right) ... \end{aligned} \tag{2.67}$$

where F_i are the finite difference equations of the operators x_i (Stone & Norman, 1992a).

In ZEUS-3D the 'parts' are divided into two steps, the 'source step' and 'transport step'.

Source step The source step deals with the parts of the differential equations which represent the source terms such as density and energy. The following finite difference approximations are solved,

$$\rho\frac{\partial v}{\partial t} = -\nabla p - \rho\nabla\Phi - \nabla\cdot Q \tag{2.68}$$

and

$$\frac{\partial e}{\partial t} = -p\nabla\cdot v - Q\nabla v \tag{2.69}$$

where Q represents an artificial viscosity (see Section 2.3.6).

Transport step The transport step deals with the fluid advection by effectively moving the density, momentum and internal energy across zone boundaries.

It uses an integral form of the equations which maintain the conservation of the variables,

$$\frac{d}{dt}\int_V \rho dV = -\int_d v\rho\left(v - v_g\right)) \cdot ds \tag{2.70}$$

$$\frac{d}{dt}\int_V \rho v dV = -\int_d v\rho v\left(v - v_g\right)) \cdot ds \tag{2.71}$$

$$\frac{d}{dt}\int_V e dV = -\int_d ve\left(v - v_g\right)) \cdot ds \tag{2.72}$$

where v_g is the grid velocity if a moving grid was implemented.

The integral form is second order accurate and uses a piecewise linear function to represent the distribution of flux in a zone. After the interpolation, advection is performed using finite-difference approximations to the advection equations. The advection is performed independently in each spatial direction starting with the x-direction (Stone & Norman, 1992a).

ZEUS-3D uses a 'consistent transport' method. This transports the following quantities; the mass density, ρ, the specific internal energy, $\frac{e}{\rho}$ and the specific momenta, $\frac{s_1}{\rho}$, $\frac{s_2}{\rho}$ and $\frac{s_3}{\rho}$. This method reduces the effects of numerical diffusion on the local conservation of the variables by making them *consistent* with the mass density. Due to the fact that momentum rather than velocity is transported, velocity and density occupy different cell locations on the staggered grid so the density is averaged to create the momentum values (Stone & Norman, 1992a).

2.3.5 Advection schemes

ZEUS-3D uses a staggered-grid meaning some variables are situated in the zone center while others are on the zone sides (e.g. see Figure 2.16). The rate of change of a quantity or flux, q, within the zone centered area or volume is equal to the divergence

of the variable q through the zone surfaces.

Operator-split methods are most prone to errors during the advection step. The difficulty is in creating an accurate interpolation algorithm to calculate the interpolated value of q at the control volume faces. There are three rules for the interpolation to ensure stability and accuracy:

1. Needs to be monotonic. This means it will not introduce extrema into the flow.

2. Must be up-winded to preserve positivity.

3. Must be time centered to reduce diffusion and preserve accuracy.

(Stone & Norman, 1992a).

ZEUS-3D has been written with the capability of implementing three finite difference schemes. These include a basic first order Donor Cell scheme, a second order van Leer method and a third order Piecewise Parabolic Advection (PPA) scheme. The second order van Leer method (van Leer, 1977) has been found to give comparable results to the more computationally intensive third order scheme and thus is the scheme used as standard.

2.3.6 Artificial viscosity

In Section 2.1, it was noted that the Euler equations do not include viscosity terms. However, an inherent effect known as *numerical* viscosity is created due to the numerical character of the solutions.

The finite difference approach uses only approximations which leads to a natural numerical dissipation. It is most noticeable through a 'smoothing' or 'softening' across contact discontinuities which define shock fronts. Ideally, the contact discontinuities should remain one zone wide while propagating through the grid.

To counteract the problem of numerical viscosity, an artificial viscosity, Q, is implemented using the von Neumann & Richtmyer approach. This approach works by smoothing shocks slightly by a couple of zones while holding the entropy change and propagation velocities across the shock correct (Stone & Norman, 1992a). Also, the viscosity must only effect the regions near the shocks and is made negligible elsewhere in the flow field. In our simulations, we fix the artificial viscosity, controlled by the parameter `qcon` in the input file, to a value of 2. This fixes shocks to be two zones in width.

ZEUS-3D also possesses the ability to implement a linear artificial viscosity for dampening oscillations which may occur in static regions of the flow (Stone & Norman, 1992a). It is controlled by the `qlin` parameter but we leave it deactivated.

2.3.7 Boundary conditions

It is necessary for the exterior of the computational domain to be surrounded by a layer of additional zones known as *ghost* zones. These ensure accurate values can be computed for the normal *active* zones around the edge of the visible grid. ZEUS-3D applies two layers of ghost zones and can define five types of boundary conditions which can be implemented along any part of the grid boundary:

- **Reflecting:** Zone centered values in the ghost zones are set equal to those of the neighbouring active zones but the normal velocity component is reduced to zero along the boundary and reflected in the second ghost zone.

- **Symmetry:** Here the the velocities of the ghost zones are set to the negative of those in the active zones to create a velocity of zero along the boundary. In our axisymmetric runs, the lower x-boundary along which the jet beam propagates is set to the symmetry boundary condition.

- **Inflow:** The ghost zones are assigned a fixed or variable set of values from the input file. This boundary condition behaves as the input nozzle for our jets.
- **Outflow:** The ghost zone values are simply set to those of the neighbouring active zones. This allows flows to effectively leave the grid. We have the remainder of the grid boundaries set for outflow conditions.
- **Periodic:** Here the ghost zone values are taken as those from the active zones at the boundary on the opposite side of the grid.

(Stone & Norman, 1992a).

2.3.8 ZEUS-3D program flow chart

Before running a simulation with ZEUS-3D, an executable must first be configured and compiled. These initial configurations define the coordinate system to use, the grid dimensions, and which physics modules to be included. After compiling and obtaining the executable, further configuration is possible without re-compilation through the main input file, the `inzeus` file. This file assigns values to all the variables, sets the total running time for the code and the intervals to output the data. Re-compilation is only required if the grid dimensions are to be modified and if the physics modules are to be changed.

When the code is executed, ZEUS-3D follows the steps displayed in the schematic flow-chart of Figure 2.6 and summarised as follows:

- The initial grid and variables are set with information read from the input file before the main loop begins to cycle. The task of the main loop through each cycle is to integrate the partial differential equations forward in time by one time step.
- The Poisson equation, used to calculate gravitational potential, is solved if grav-

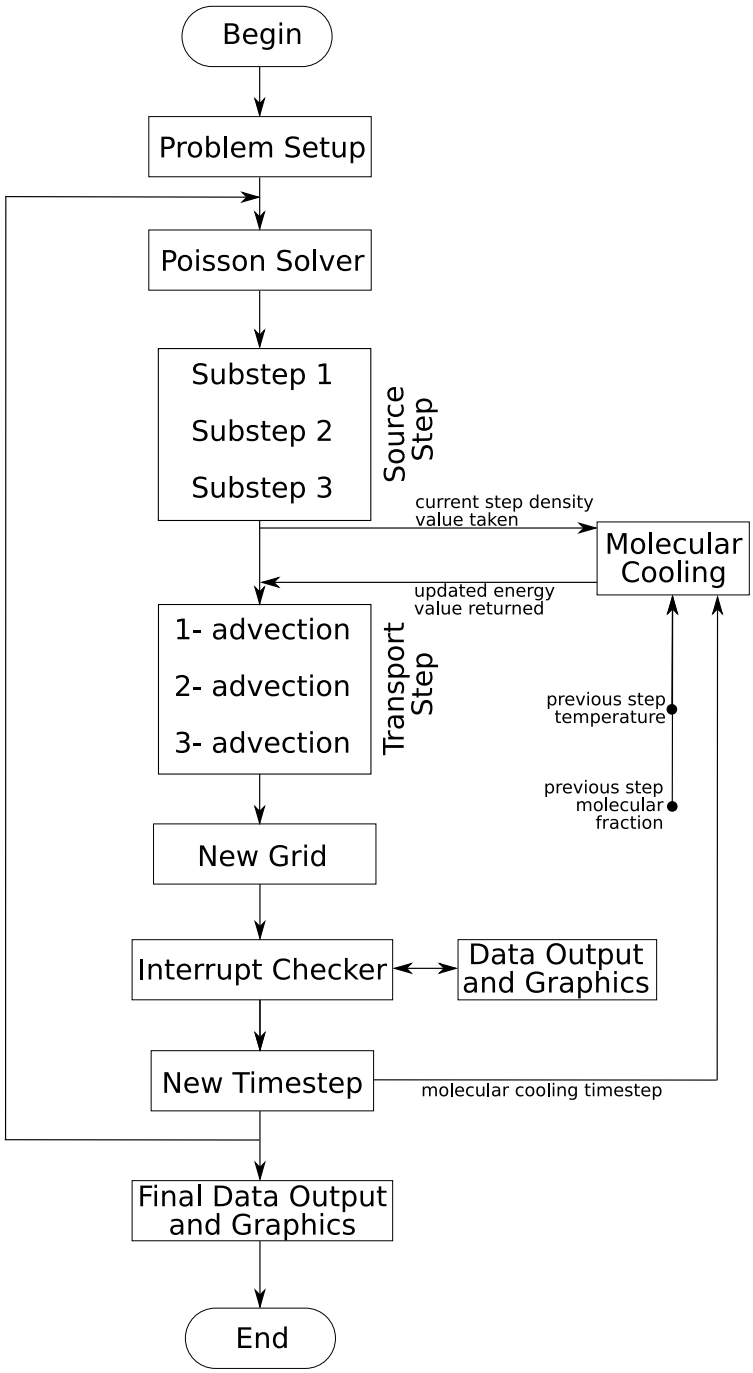

Figure 2.6: A schematic flow chart displaying the steps which the ZEUS-3D program runs through for each time step. Figure based on Fig.7 of Stone & Norman (1992b).

itation has been activated.

- The 'source step' is entered which is divided into three sub-steps described in

Section 2.3.4.

  - Velocities generated by pressure gradients, gravitational forces and curvature terms are calculated.
  - The partially updated velocities are used to add artificial viscous stress and heating terms.
  - Compressional heating terms are added using a two step predictor-corrector method.

- The molecular chemistry routines are calculated using a semi-implicit method (see Section 2.5).

- The 'transport step' solves the advection equations, shown in Section 2.3.4, to transport the density, momentum and internal energy across the grid cells. It uses an integral form of the equations in order to maintain the conservation of the variables.

- If a moving grid has been activated, new grid velocities are calculated.

- The Interrupt Checker looks for optional user input at the console. These can invoke functions such as the saving of the output data or the pausing, restarting and quiting of the code execution. Without intervention, the output data is automatically saved at fixed times as set by the user in the main input file.

- A new timestep is calculated for the next cycle based on the Courant condition, see Section 2.3.3.

- The above sequence of stages are repeatedly cycled until a total time limit defined in the input file has been reached.

2.4 Various ZEUS-3D subroutines

ZEUS-3D was written with high adaptability in mind, ensuring it could be used to simulate a wide range of fluid dynamics problems. The computational domain can be set to either 1D, 2D, 2.5D axisymmetry or full 3D as the hydrodynamic equations and their finite-difference forms are implemented in a co-ordinate independent fashion (Stone & Norman, 1992a).

A 'moving-grid' can also be used where the grid zones may be assigned a certain velocity. This could allow for a limited tracking ability where, for example, the front of a jet could be effectively held on the grid indefinitely to study the effects of molecular destruction and reformation in the bow shock.

The use of a ratioed grid, where the grid zones vary in size, is also available (see Section 2.4.1).

For jet simulations, the input boundary conditions are very versatile allowing for precession and pulsations in the form of sinusoidal velocity variations.

The version of ZEUS-3D used for the work in this thesis includes a molecular chemistry module, an essential element for the simulation of protostellar jets and outflows (see Section 2.5).

Additionally, a new module has been created to calculate the instantaneous mass-velocity (see Section 2.8) at regular intervals during a simulation. This helps to link simulations with observations. It also allows one to track how the mass-velocity values vary dynamically during a simulation (see Section 4.1).

2.4.1 Ratioed grid

ZEUS-3D is coded with the option for implementing a ratioed grid. This initialises the grid domain with grid zones of varying size. This may be advantageous in certain

situations. For example, the setting of finer zones towards the end of the grid in order to resolve the important physics of a jet head and bowshock in greater detail, or the setting of finer zones near the beginning of the grid to better resolve an accretion disk structure. The ratioed grid is fixed and defined at the beginning of the simulation and thus is not adaptable like SPH codes. A basic example of how a 2D grid would appear if ratioed in both the x- and y-direction is shown in Figure 2.7.

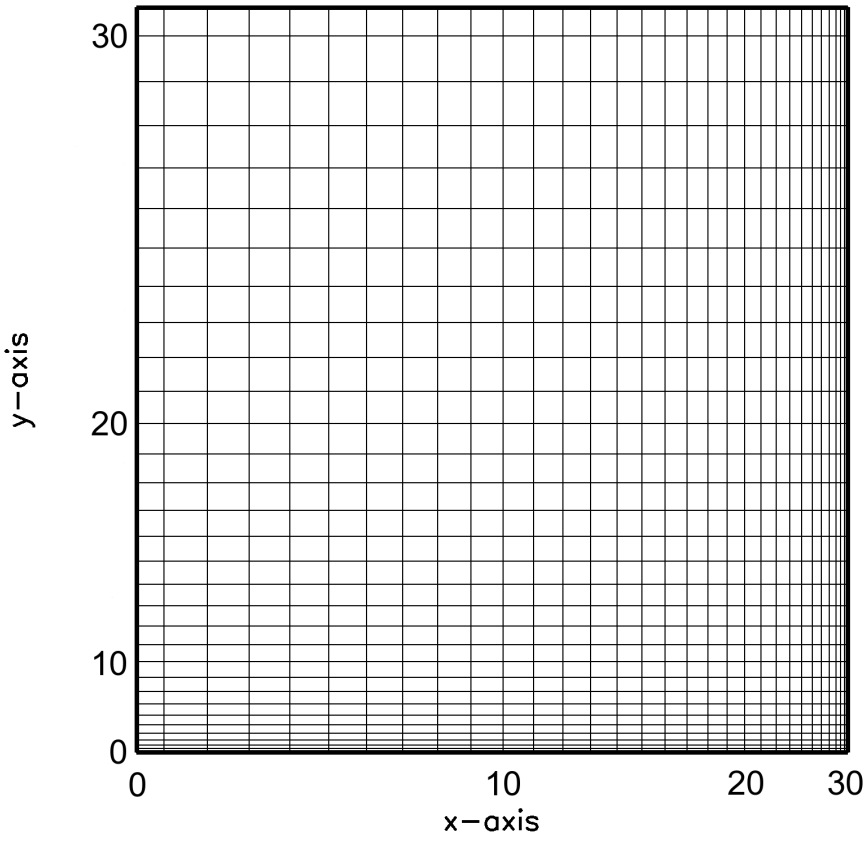

Figure 2.7: An example of how a ratioed grid would appear in 2D if both the x- and y-directions were ratioed.

ZEUS-3D calculates the ratioed grid in the following way. The desired ratio (for the x-direction in this case), is controlled by the `x1rat` parameter from the main input file which is defined as the ratio of the size of two adjacent zones,

$$\texttt{x1rat} = \frac{\texttt{dx1a(i+1)}}{\texttt{dx1a(i)}} \tag{2.73}$$

where `dx1a` is the zone size and `i` is the zone position.

ZEUS-3D then scales the zones on the grid using the following formula (shown for the x-direction),

$$\texttt{x1a(i)} = \texttt{x1min} + \texttt{dx1min} * \left(\left(\texttt{x1rat}^{\texttt{i}} - 1\right) / \left(\texttt{x1rat} - 1\right)\right) \tag{2.74}$$

where array `x1a` defines the positions of the zone boundaries, `x1min` is the smallest zone size on the grid, `dx1min` is the difference in size between two adjacent zones, and `i` is the zone positional number.

As an example, if we were to set `x1rat` to a value of 1.001, then for a 3,000 zone length grid, the resulting ratio would lead to grid points which are, $1.001^{3000} - 1 = 20$ times better resolved at the end of the grid compared to the beginning.

We performed a test of the ratioed grid whose result is presented in Figure 2.8a. A further adjustable parameter in the main input file is `igrid` which defines the direction of the ratio. For the jet simulation we want the smallest zones towards the end of the x-direction so `igrid` was set to 1. For the y-direction, we wanted the smallest zones close to the jet axis then `igrid` was inverted by setting it to -1. In order to correctly visualise the results from a ratioed grid simulation, the plotting program must incorporate the same ratios in order to re-size the zones accordingly as the output data from ZEUS-3D consists only of data arrays.

The ratioed grid plot in Figure 2.8a can be compared directly to Figure 2.8b which differs only in that it was performed on a uniform grid. Immediately we the see the additional fine detail obtained by the ratioed grid, despite the fact that the simulations were both performed on 3,000×600 zone grids. In fact, Figure 2.8a, appears to be comparable to the higher 4,000×800 zone grid resolution run presented in Figure 2.14. Only the overall run-time is effected where the smaller zone sizes on the ratioed grid lead to more calculations due to the smaller timesteps.

We chose to remain with uniform grids in the studies of Chapter 3 and 4. Data from

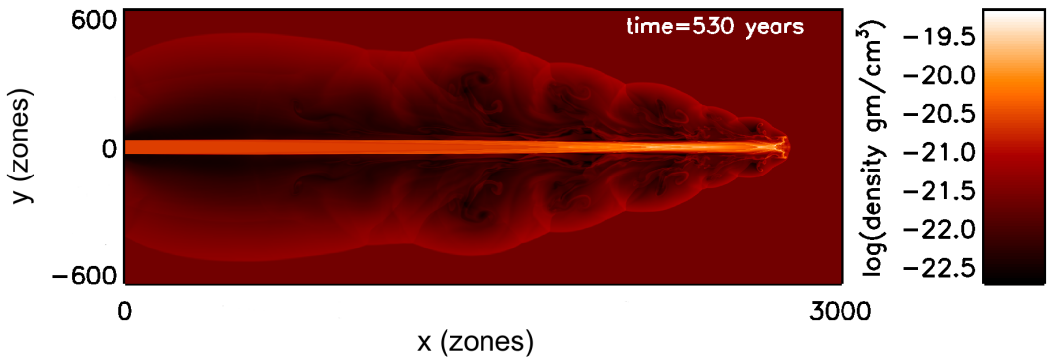

(a) Ratioed grid simulation example

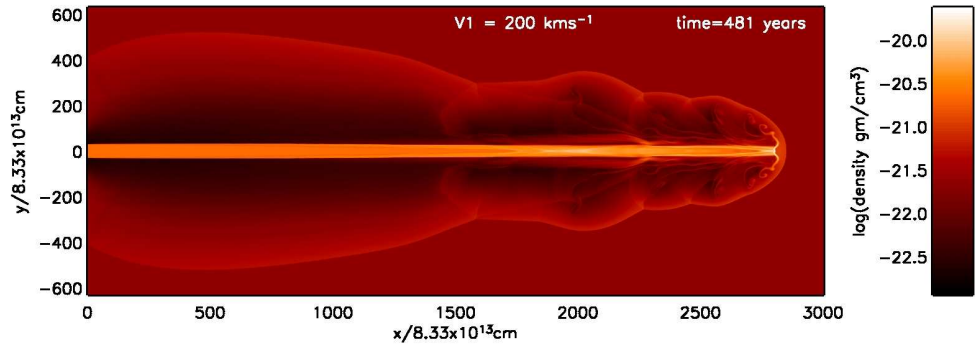

(b) Uniform grid simulation example

Figure 2.8: **a:** A 2.5D simulation performed with a ratioed grid in both directions. The simulation is of an axisymmetric adiabatic jet propagating at 200 km^{-1} on a grid of 3,000×600 zones with `x1rat`=1.001 and `x2rat`=1.005. Note there is a non-linear distance scaling along both axes. **b:** A similar 2.5D simulation with the same total number of zones, 3,000×600, but performed using a uniform grid for direct comparison.

uniform grids were easier to analyse with less possibility of errors from post-processing. Also, with uniform grids, we are not introducing additional factors/structures that may make the code more accurate in some zones rather than others. Ideally we wish to have a high resolution everywhere.

2.4.2 3D – Precession – Pulsation

Some full 3D simulations were also performed. For example, Figure 2.9 shows a molecular jet propagating into a slightly over-dense (η=10) molecular ambient medium. It incorporates the pulsation and precession algorithms.

For the pulsation algorithm, the pulsations are controlled by the `fpulse` parameter. It can be set between 0.0 and 1.0, where 1.0 implies a 100% velocity variation of the initial input velocity. In the simulation presented here, the initial jet velocity was set to 100 km^{-1} and `fpulse` set to 1.0. This implies the actual velocity ranges from 200 km s^{-1} to 0 km s^{-1} over the duration of each pulse. In ZEUS-3D the pulsation algorithm is defined as,

$$\texttt{x1vel} = \texttt{v1jet} * (1.0 - \texttt{fpulse} * \texttt{dsin}\,(\texttt{ompulse} * \texttt{time})) \tag{2.75}$$

where `x1vel` is the instantaneous input velocity at a given time, `time`, `v1jet` is the initially defined input velocity, and `ompulse` $= c_s/$`rjet`, the sound speed divided by the jet radius. For the jet in Figure 2.9 there is an initial single pulsation of period 800 years after which a repeated pulsation rate of 200 years begins.

The jet beam in the simulation is also precessing. A slight precession angle is useful in 3D simulations to break the self imposed symmetry of a supersonic beam. The adjustable parameters to control the precession rate are `thetaj`, which is the ratio between v2 and v1 at the jet inlet, and `thetak` which is the ratio between v3 and v1 at the jet inlet where v1, v2 and v3 are the components of velocity in the x-, y- and z-directions respectively. Setting `thetaj` = `thetak` creates a circular helical motion. In this case we have `thetaj` = `thetak` = 0.1. Due to the fact that the jet is pulsating, the precession period is varying with time. However, if the jet were at a steady 100 km s^{-1}, the period of a full precession would be 400 years.

The display in Figure 2.9 shows a slice of the outflow in the x-y plane taken through the center of the jet beam in the z-plane. The outflow appears lopsided as the initial pulsation, with a longer precession period, was directed downward towards the bottom x-z plane. The later 200 year period pulses have yet to fill out the upper region.

We see almost complete molecular dissociation in the upper edge of the bowshock. This edge has been impacted by two of the shorter period pulses destroying the molecules

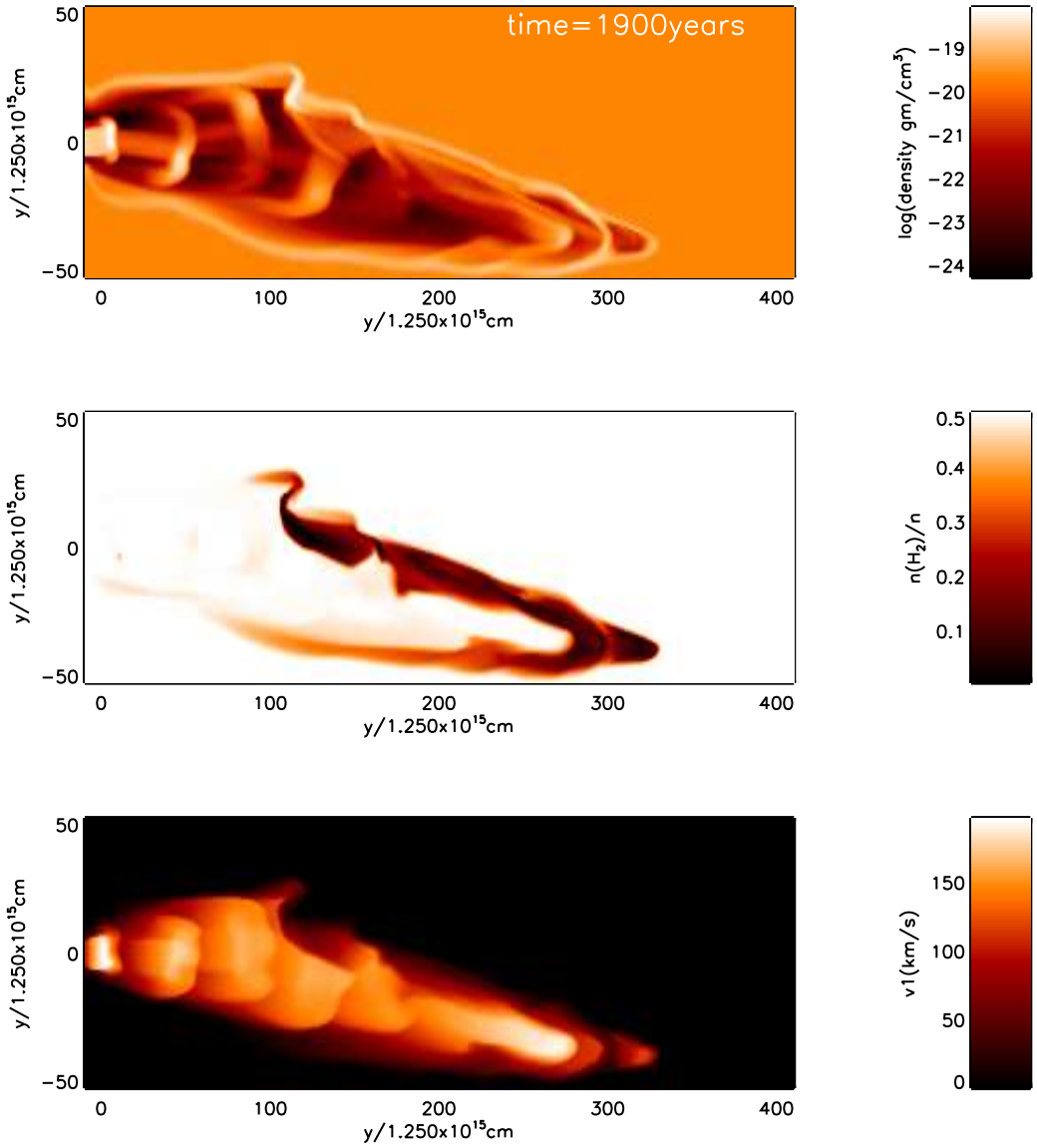

Figure 2.9: An example of a full 3D simulation on a grid of 400×100×100 zones of a jet with an initial single pulsation of period 800 years, followed by a repeating pulsation period of 200 years. The pulsation amplitude is set to 100% so that the velocity ranges from 200 km s^{-1} to 0 km s^{-1} over the duration of each pulse. A precession angle is also implemented by `thetaj` = `thetak` = 0.1

which survived in the initial bowshock. The internal working surfaces of the later pulses show some very slight molecular dissociation. This molecular survival is due to the fact that the pulses are propagating into a medium which is already in motion. This may be similar to the numerical study performed by Lim et al. (2002), who showed that ambient molecular gas may survive the passage through shocks in certain situations if

it has been slowly accelerated from rest to high velocities. The slow acceleration allows the molecular gas to pass through the shock front while the shock is still weak. Our simulation differs in that the molecular material is introduced as a jet beam onto the grid. The moving molecular jet material from a previous ejection event is able to pass through the working surface of the next ejection event without much dissociation due to the small velocity differences.

The size of a zone in this particular 3D simulations is 1.25×10^{15} cm. The jet radius is 2.5×10^{15} cm implying there are only 2 zones per jet radius. The simulation also requires 4,000,000 zones in total. If we wished to perform the axisymmetric simulations presented in Chapter 3 and 4 in full 3D, while maintaining their same high spatial resolution, the computer resources required would be 800 times greater and the run-time would be increase by an order of magnitude (see Section 2.6).

The full 3D simulations may capture the actual appearance of an outflow with the greater level of realism obtained from the extra dimension when compared to 2D or 2.5D axisymmetric simulations, however the computational requirements greatly increase. A higher resolution is more appropriate for our simulations as we wish to resolve important cooling timescales (see end of Section 2.5).

2.5 Molecular cooling

Molecules and molecular reactions play a major role in the physics of star formation and jet dynamics. They have also proved indispensable in understanding the physical conditions present in star forming regions as observing them provides detailed information such as temperatures, densities and velocities through both absorption and emission lines. Therefore, an accurate portrayal of the chemical reactions in a code to model protostellar outflows is imperative.

In its simplest form, molecular cooling can be presented in the following way. A supersonic shock wave passing through a medium provides kinetic energy to the particles

(atoms, molecules and ions) present. The extra kinetic energy leads to an increase in the collision rates between the particles and in turn may lead to an excitation energy. In the case of atoms and ions, the electrons rise from their lowest stable energy states (or atomic orbitals) to higher unstable orbitals. In the case of molecules, there is an increase in the energy associated with the rotational and/or vibrational states of the molecular bonds. Excited states are unstable and after some time the electrons cascade back towards the lowest energy ground states by emitting the excess energy as a photon of energy, $\hbar\omega$. If the photon escapes the medium without being re-absorbed the medium loses kinetic energy and cools. The process is summarised as follows,

$$A + B \rightarrow A + B^* \tag{2.76}$$

$$B^* \rightarrow B + \hbar\omega \tag{2.77}$$

where A and B are two ground state species, B^* is the excited form of species B and $\hbar\omega$ is the emitted photon.

The version of ZEUS-3D used in this thesis builds upon the base version by including molecular cooling functions. They are based upon molecular routines used by Suttner et al. (1997). As will be seen below, the cooling functions would be quite computationally complex when implemented into the code. Their efficiency has been improved by noting that in both the low and high temperature regimes only certain coolants need to be considered as important. This allows the cooling functions to be split into high temperature (T > 3,000K) and low temperature (T < 3,000K) subroutines in order to increase the speed of the code. A sample plot of cooling rates versus temperature is shown in Figure 2.10. Furthermore, the values of the exponents of the cooling functions have been pre-calculated and tabulated in look-up tables, again in order to increase the speed of the code.

The molecular cooling modifies the energy equation from Equation 2.3 with an ad-

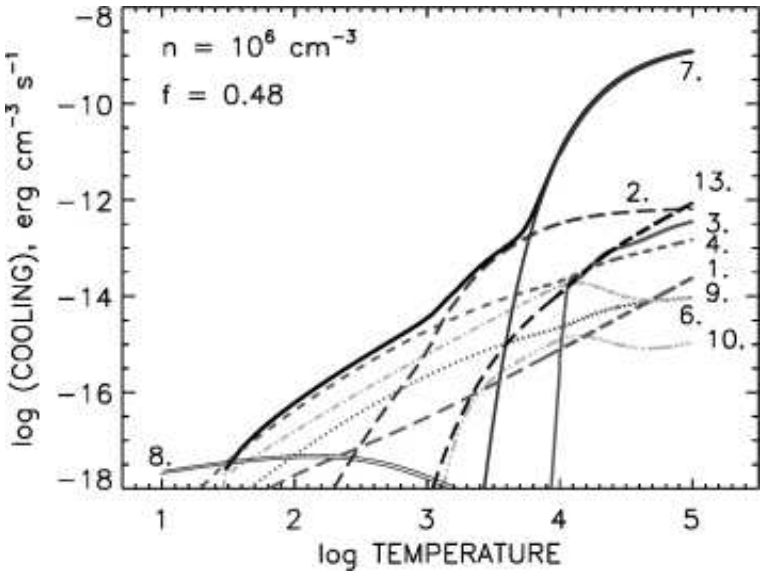

Figure 2.10: A figure displaying the cooling functions at the indicated density, n, and H_2 fraction, f. The cooling rates are strongly dependent on temperature. The numerical labeling is as follows; 1. Gas–Grain cooling, 2. H_2 rotational–vibrational cooling, 3. Atomic cooling, 4. H_2O rotational cooling, 5. H_2O and H vibrational cooling, 6. H_2O and H_2 vibrational cooling, 7. H_2 dissociation cooling, 8. H_2 reformation heating, 9. CO rotational cooling, 10. CO and H_2 vibrational cooling, 11. CO and H vibrational cooling, 12. [OI] 63μm fine structure cooling 13. OH rotational cooling. (Figure reproduced from Smith & Rosen (2003))

ditional term as follows,

$$\rho \frac{D}{Dt}\left(\frac{e}{\rho}\right) = -p\nabla \cdot v - \Lambda\left(T, n, f\right) \tag{2.78}$$

where the new term, $-\Lambda\left(T, n, f\right)$, represents the cooling function and is dependent on a combination of the temperature, T, of the gas, the hydrogen nuclei density, n, and the molecular hydrogen abundance, f.

The complete cooling function currently consists of 13 sub-functions,

$$\Lambda\left(T, n, f\right) = \sum_{i=1}^{13} \Lambda_i \tag{2.79}$$

The sub-functions have been detailed in Appendix A of Smith & Rosen (2003) and summarised below:

- Λ_1: This is dust or gas-grain cooling based on Hollenbach & McKee (1989) (Equation 2.15):

$$\Lambda_1 = n^2 \times L_g \tag{2.80}$$

where L_g is

$$L_g = (3.8 \times 10^{-33})\sqrt{T}(T - T_g)\,(1.0 - 0.8exp(-75/T))\ \ erg\ s^{-1}cm^3 \tag{2.81}$$

with the dust grain temperature, T_g fixed at 20K. It assumes a standard ISM composition. The actual composition of protostellar jets are not yet fully known.

- Λ_2: H_2 vibrational and rotational cooling based on Lepp & Shull (1984) (Equations (7) – (12)):

$$\Lambda_2 = n_{H_2}\left(\frac{L_v^H}{1 + (L_v^H/L_v^H)} + \frac{L_r^H}{1 + (L_r^H/L_r^H)}\right) \tag{2.82}$$

where the vibrational cooling coefficients are subscripted v and the rotational cooling coefficients are subscripted r. The coefficients are also superscripted H to signify high density and L for low density.

- Λ_3: Atomic collisional cooling. It uses the Fe=–0.5 tabulated values in Table 10 of Sutherland & Dopita (1993):

$$\Lambda_3 = n_H^2 L_3 + 1.42 \times 10^{-27}(\sqrt{T}) \tag{2.83}$$

The final $(\sqrt{T})$ term is an additional a thermal Bremsstrahlung term used only when the temperature rises above 10,000K. Atomic cooling assumes an ionisation steady state with the cooling rate. In reality, the ionisation rate would lag behind the cooling rate, but only for high temperatures above 8000K. However, we do not resolve the atomic cooling at such high temperatures so the discrepancy is not an issue.

- Λ_4: Cooling through rotational modes of water:

$$\Lambda_4 = (n_{H_2} + 1.39 n_H) \times n_{H_2O} \times 1.32 \times 10^{-23} \left(\frac{T}{10^3} \right)^{\alpha} \tag{2.84}$$

where the exponent, α, equals 1.35–0.3 $\log(\frac{T}{10^3})$ from Neufeld & Kaufman (1993).

- Λ_5: Cooling through vibrational modes of water with molecular hydrogen collision based on Hollenbach & McKee (1989):

$$\Lambda_5 = 1.03 \times 10^{-26} n_{H_2} n_{H_2O} \times T \; exp\left(\frac{-2,325}{T} \right) exp\left(\frac{-47.5}{T^{\frac{1}{3}}} \right) \tag{2.85}$$

- Λ_6: Cooling through vibrational modes of water with *atomic* hydrogen collision again based on Hollenbach & McKee (1989):

$$\Lambda_6 = 7.40 \times 10^{-27} n_H L_3 n_{H_2O} \times T \; exp\left(\frac{-2325}{T} \right) exp\left(\frac{-34.5}{T^{\frac{1}{3}}} \right) \tag{2.86}$$

- Λ_7: Cooling from collisional dissociation of molecular hydrogen based on Shapiro & Kang (1987):

$$\Lambda_7 = 7.18 \times 10^{-12} \left((n_{H_2}^2)(k_{D,H_2}) + (n_H)(n_{H_2})(k_{D,H}) \right) \tag{2.87}$$

where the first term on the right is the dissociation energy of H_2 (4.48 eV) and

$$k_{D,H} = 1.2 \times 10^{-9} \; exp(-52,400/T)(0.0933 \; exp(-17,950/T))^{\beta} \; cm^{-3} \; s^{-1} \tag{2.88}$$

$$k_{D,H_2} = 1.3 \times 10^{-9} \; exp(-53,300/T)(0.0908 \; exp(-16,200/T))^{\beta} \; cm^{-3} \; s^{-1} \tag{2.89}$$

Some molecular hydrogen cooling cross sections are not well known. We assume an ortho-para ratio of 3. This could lead to errors as high as 20%. However, as we are also considering power-laws over many magnitudes, the potential errors should not influence our results.

- Λ_8: Heating from molecular hydrogen reformation:

$$\Lambda_8 = -L_7 \; nn_H(1-\beta) \; 7.18 \times 10^{-12} \tag{2.90}$$

where β is the fraction of thermally released energy rather than radiated and L_7 is defined as,

$$L_7 = (3 \times 10^{-18} cm^3 s^{-1}) \times \frac{\sqrt{T} f_a}{1 + 0.04\sqrt{T + T_g} + 210^{-3} T + 810^{-6} T^2} \tag{2.91}$$

with f_a as:

$$f_a = [1 + 10,000 \; exp(-600/T_g)]^{-1} \tag{2.92}$$

- Λ_9: Cooling through rotational degrees of freedom of CO from atomic and molecular hydrogen collisions. Based on Equations 5.2–5.5 of McKee et al. (1982):

$$\Lambda_9 = n_{CO} \; n \frac{kT\sigma v_T}{1 + \frac{n_a}{n_{cr}} + 1.5\sqrt{\frac{n_a}{n_{cr}}}} \tag{2.93}$$

where $\mathrm{v}_T = \sqrt{\frac{8kT}{\pi m_{H_2}}}$, n_a=0.5($\mathrm{n}_H + \sqrt{n_{H_2}}$), n_{cr}= $3.3 \times 10^6 \; T_3^{0.75} \; cm^{-3}$, and $\sigma = 3.0 \times 10^{-16} T_3^{-0.25} \; cm^{-2}$ with T_3 = T/1,000K.

- Λ_{10}: Cooling through vibrational modes of CO from atomic and molecular hydrogen collisions taken from Neufeld & Kaufman (1993):

$$\Lambda_{10} = 1.83 \times 10^{-26} \; n_{H_2} \; n_{CO} \; \sqrt{T} \; exp(3080/T) \; exp(\frac{-68}{T^{\frac{1}{3}}}) \tag{2.94}$$

- Λ_{11}: Cooling through vibrational modes of CO from atomic and molecular hydrogen collisions. Also taken from Neufeld & Kaufman (1993):

$$\Lambda_{11} = 1.28 \times 10^{-24} \; n_{H_2} \; n_{CO} \; T^{\frac{1}{2}} \; exp(-3080/T) \; exp(-(2000/T)^{3.43}) \tag{2.95}$$

- Λ_{12}: Fine structure 63μm Oxygen cooling:

$$\Lambda_{12} = 2.82 \times 10^{-18}\ n_O\ \frac{1}{\frac{1}{f_H} + \frac{A_{10}}{r_L}} \tag{2.96}$$

where A_{10} is the spontaneous transition rate of $8.95{\times}10^{-5}\mathrm{s}^{-1}$ and f_H is the fractional occupation of the $^3\mathrm{P}_1$ level, defined as,

$$f_H = \frac{0.6\ exp(-228/T)}{1 + 0.6\ exp(-228/T) + 0.2\ exp(-326/T)} \tag{2.97}$$

and $\mathrm{r}_L = \mathrm{r}_H + \mathrm{r}_{H_2}$ are collisional rates of atomic and molecular hydrogen,

$$r_H = (4.37{\times}10^{-12}T^{0.66}0.6\ exp(-228/T){+}1.06{\times}10^{-12}T^{0.80}0.2\ exp(-326/T)){\times}(n_H{+}0.48n_H) \tag{2.98}$$

$$r_{H_2} = (2.88{\times}10^{-11}T^{0.35}0.6\ exp(-228/T){+}6.68{\times}10^{-11}T^{0.31}0.2\ exp(-326/T)){\times}(n_{H_2}) \tag{2.99}$$

- Λ_{13}: OH cooling taken from Hollenbach & McKee (1989):

$$\Lambda_{13} = 2.84 \times 10^{-28} n^2 T^{\frac{3}{2}} \tag{2.100}$$

2.6 Resolution study

The main limiting factor for any numerical code is that of resolution. Higher resolutions over a certain domain size lead to the capability of resolving additional fine structure, but require greater computational resources. Additionally, supersonic flows are naturally turbulent so a slight change between any two simulations may lead to substantially different structure downstream of the flow. The purpose of this study was to find the optimum resolution to use in our simulations with the above limitations in mind.

The simulations in this section are purely hydrodynamic with no molecular cool-

ing or MHD. The jet flow is exclusively defined by the equations of hydrodynamics supplemented by an adiabatic equation of state.

The calculations are executed on a 2.5D grid. This involves a cylindrical coordinate system where the azimuthal coordinate, ϕ, is ignored. We thus use the z and r coordinates, displayed in the figures as the x and y directions respectively. The jet beam is introduced from $z = 0$ and $r < r_j$, creating a narrow flow adjacent to the central axis. Note that only half of the displayed flow is calculated. Symmetry is assumed and the bottom half of the jet is simply mirrored from the top for display purposes.

After compilation, ZEUS-3D is run from an executable file. The larger the grid, or the more physics included, the more RAM the executable requires. The grid basically consists of data arrays containing the values of the variables in the grid zones. For hydrodynamics there are five arrays for the main variables: density, pressure and three components of velocity. MHD requires three additional arrays for the three components of magnetic field and molecular cooling requires one extra array. In addition, there are eleven 'scratch' arrays used to store intermediate values plus about 5% extra for overheads such as ghost zones at the grid boundaries.

As an example, we can roughly calculate the size of the executable for a basic 4000×800 zone hydrodynamic run noting that every variable requires 8 bytes of memory,

$$(4000 \times 800 \times (3 + 11) \times 8) + 5\% = 376\,\text{Megabytes}$$

When the molecular cooling module is activated, and the automatic mass-velocity calculation routine is added (see Section 2.8), then the executable requires 535 megabytes of RAM. If the MHD module were also to be added, the executable would require 610 megabytes of RAM. At 8000×1200 zones, without MHD, 1573 megabytes of RAM are required.

Storage space for the output files must also be considered. Each array variable requires 4 bytes for storage using the efficient Hierarchical Data Format (HDF) file

format which is used by ZEUS-3D. To output the arrays of four variables – density, pressure and two components of velocity, at 20 time intervals during the 4000×800 run, would require a total storage space of,

$$4000 \times 800 \times 4 \times 20 \times 4 = 1024\text{MB} \sim 1 \text{ Gigabyte}$$

where each HDF file at the 4000×800 zone resolution requires about 13 megabytes. An individual HDF file of a 8000×1200 zone run requires 38 megabytes of disk storage space.

2.6.1 Results

We simulated a 200 km s^{-1} adiabatic hydrodynamic jet at the following grid resolutions:

- 1000×200, 1 zone = 2.5×10^{14} cm (Figure 2.11),
- 2000×400, 1 zone = 12.5×10^{14} cm (Figure 2.12),
- 3000×600, 1 zone = 8.33×10^{13} cm (Figure 2.13) and
- 4000×800, 1 zone = 6.25×10^{13} cm (Figure 2.14).

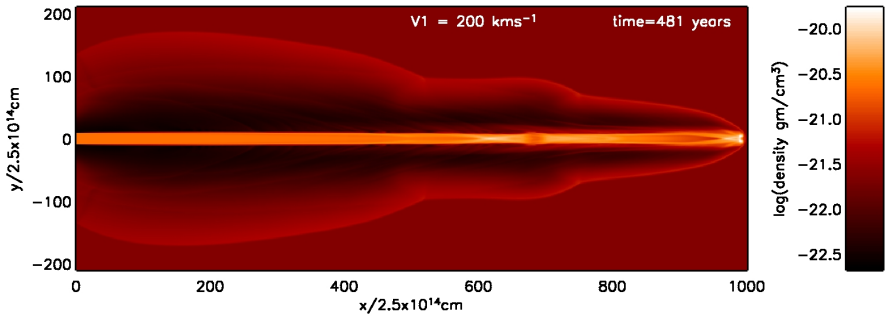

Figure 2.11: Density projection of the 200 km s^{-1} adiabatic hydrodynamic jet in 2.5D at a resolution of 1000×200 zones.

From the results of Figures 2.11 to 2.14 we can see that by increasing the resolution, small structural and eddy details become evident within the flow.

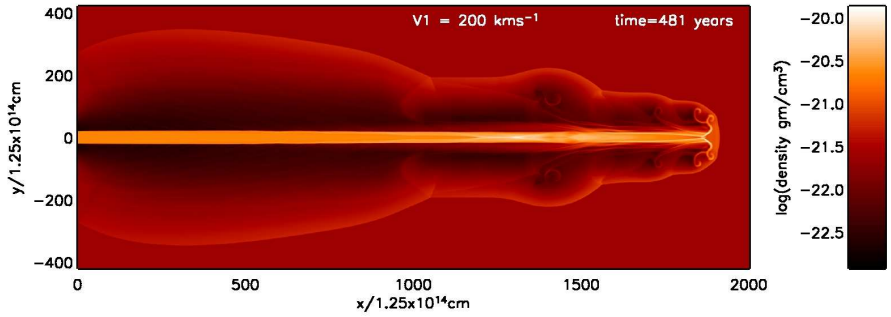

Figure 2.12: Density projection of the 200 km s^{-1} adiabatic hydrodynamic jet in 2.5D at a resolution of 2000×400 zones.

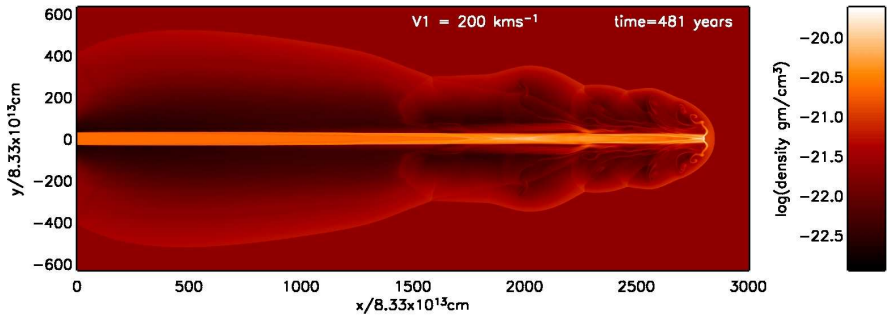

Figure 2.13: Density projection of the 200 km s^{-1} adiabatic hydrodynamic jet in 2.5D at a resolution of 3000×600 zones.

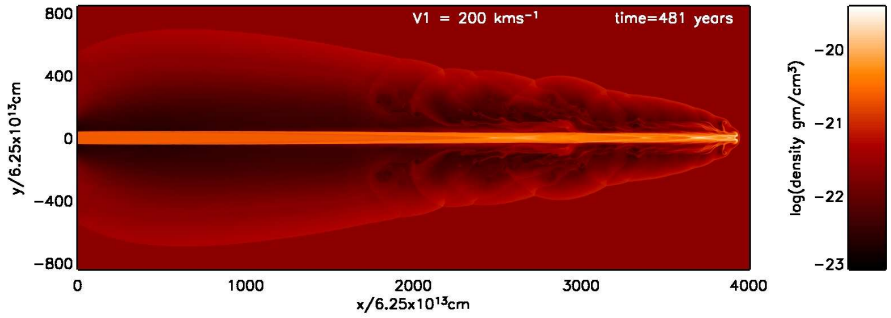

Figure 2.14: Density projection of the 200 km s^{-1} adiabatic hydrodynamic jet in 2.5D at a resolution of 4000×800 zones.

Noticeable morphological differences between the plots are seen in Figures 2.12 and 2.13 where the outflow possesses a blunter nose compared to the outflows of Figures 2.11 and 2.14 which have a sharper nose. A comparison can also be made to the ratioed grid example in Figure 2.8a which also possesses a sharp nose.

Does the resolution effect the overall morphology of the jet? A time sequence animation of the simulations provides a clearer picture of the jet's development over time compared to viewing a static image of a fixed time. An animation allows us to easily follow the development of the cocoon, vortices and other features. Animations of these simulations show that all four jets fluctuate between possessing a sharp and blunt nose. Material tends to collect and build up in the working surface at the jet head leading to a blunt nose. At a certain point the build-up is quickly shed away as a vortex and eventually absorbed into the cocoon. The nose then becomes sharp until the material builds up once again.

Despite the fact that the figures show the jets at the same time, 481 years, the working surface region and cocoon are extremely turbulent places. The turbulent features resolved at the different resolutions would cause slight variations in the temporal evolution and thus the stages where there is a blunt nose or sharp nose.

Despite the random and turbulent nature of jet flows, these simulations seem to suggest that the overall jet morphology is not linked to resolution. Which resolution is the best to take? Higher resolution simulations generate more beautiful and intricate structures and we would imagine them to be more realistic. However, the factor of time and computer limitations must be considered. The general overall structure appears to be independent of resolution and actual observations of real jets can not image them at such high a resolution. However, it is better to convolve a high resolution simulation down to telescope resolution, rather than performing the simulation at telescope resolution. When molecular cooling is implemented, the zone size becomes an important factor as molecular cooling lengths should be resolved. We can circumvent this limitation somewhat by increasing the molecular and atomic gas densities on the grid.

Overall, the optimum resolution to choose is dependent on the limits imposed by the available computer resources and time.

The more zones present, the longer a simulation takes to run. This is due to the fact that a timestep depends on how fast material moves through a zone, related to the

Courant Condition (see Section 2.3.3). If we decrease the zone size, the time resolution increases, leading to an increase in the sound speed, thus making the timestep smaller so that it must perform many more cycles, and finally leading to an increase to the overall run time.

Table 2.1 shows the resolution versus the CPU time of our four test runs. The 'CPU time' is the total time in seconds which the computer was running the simulation for.

The CPU run-time , t, can be described by the following expression,

$$t \propto N_x^{(D+1)} \tag{2.101}$$

where N_x is the number of zones in the propagation direction, D is the number of spatial dimensions in the simulation and the '+1' includes time as a dimension.

Figure 2.15 presents the data of Table 2.1 plotted on a graph which plots the log of CPU time against the log of inverse resolution. In this form, the slope of the line will show at what power the resolution is proportional to the CPU time (From the law of logs: If a=b^c, log(a)=c log(b)).

A slope of 3 is obtained as expected for a 2D simulation (D=2, D+1=3). A small discrepancy may result from the slightly higher sound speed at the higher resolutions.

Table 2.1: The CPU time versus the grid resolution of our 2D axisymmetric hydrodynamic simulations.

Resolution	Zone Size (cm)	CPU time (seconds)
1,000×200	2.5×10^{14}	840.27
2,000×400	1.25×10^{14}	6,983.22
3,000×600	8.33×10^{13}	22,984.36
4,000×800	6.25×10^{13}	60,839.17

To show the ongoing ability to reach greater and greater resolution (for fixed grid codes), it can be noted that Norman et al. (1982) ran 2D axisymmetric jets on a

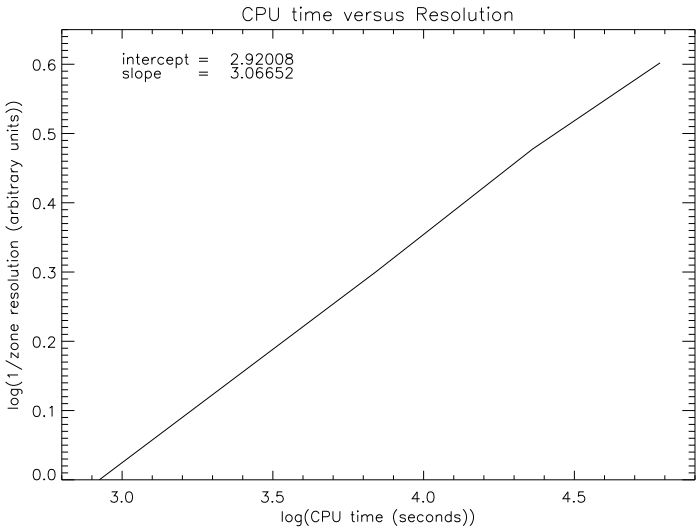

Figure 2.15: A plot of the log of the CPU time against the log of 1/resolution. The slope of 3 implies that for 2D simulations the run time is proportional to 1/zone size cubed.

grid of 60×240 zones with 8 zones per jet radius. Stone & Hardee (2000) ran 2D axisymmetric simulations at 2000×400 zones with 20 zones per jet radius. For the simulations in the following chapters we used grids of 4000×800 zones with 40 zones per jet radius, doubling the Stone & Hardee (2000) setup. We are now capable of doubling this resolution yet again by running 2D axisymmetric simulations at 8000×1400 zones with 80 zones per jet radius (e.g. Figure 4.11). This increase may not be surprising due to the continuous improvement of computer technology and stated in 'Moore's Law' which predicts the number of transistors fitting on an integrated circuit will double every 18 months.

2.6.2 Computer systems

Initially an SGI Origin 2200 supercomputer ('Forge') was available at Armagh Observatory. This was a shared memory system using an S2MP (Scalable Shared-Memory Multiprocessing) architecture with an IRIX operating system. It had 8 'R12000' CPU's which ran at 400 MHz. The total amount of RAM available was 6 gigabytes with a

total of 145 gigabytes of hard drive space.

Despite its advantage as a shared memory system for ZEUS-3D, it was replaced by the current Armagh Observatory local linux distributed memory cluster ('M44'). This consists of 25 dual-processor nodes plus a master server. Each processor operates at 3 GHz. 15 nodes contain 32 bit Intel processors and 10 nodes contain 64 bit Opteron AMD processors. Each node possesses 2 gigabytes of local RAM giving a total of 50 gigabytes of RAM. The total hard disk storage space available is 1 terabyte. It is hoped the system will eventually connect to and share the Grid-Ireland [3] gateway. ZEUS-3D was run on this system in serial on single processors.

Code runtimes can vary a lot from simulation to simulation of the same resolution depending on the existence of hot regions which slow the code execution. Hot regions possess a faster sound which require a shorter time step, which in turn requires more cycles, thus finally leading to a longer runtime.

However, to give rough example of the typical runtimes, a 4000×800 zone, axisymmetric run with molecular cooling functions activated and the automatic mass-velocity calculation routine (see Section 2.8) could take a CPU time of about 100 hours to cover a simulation time of 1000 years. For a run at 8000×1200 zones, the runtime would be roughly 14 days.

Interactive Data Language (IDL) was the software used to visualise the HDF output files and create the other plots seen in this thesis. It is commercial software currently owned by ITT Visual Information Systems [4].

2.7 Magnetohydrodynamic study

ZEUS-3D incorporates MHD algorithms. As seen in Section 1.7, magnetic fields are believed to be a crucial requirement for the launching and collimation of jets. This

[3] `http://www.grid.ie`
[4] *http://www.ittvis.com/idl/*

section will briefly describe the ZEUS-3D MHD algorithms and display some tests performed using different magnetic field configurations. We will see that strong magnetic fields effect the morphology of the jet beam. They are, however, mainly *source* (input) effects rather than environmental effects and thus we do not implement MHD in the chapters to follow as the aim of this thesis is to study the properties of the environment. The simulations in this section were used for learning and testing the capabilities of ZEUS-3D code before the later works were performed.

ZEUS-3D performs MHD using a scheme known as the 'Consistent Method of Characteristics' (CMoC). This method has improved on the many methods that have come before as it calculates the momentum transport and magnetic induction simultaneously. Previous methods have decoupled these and worked them out separately which was found to often lead to errors (Clarke, 1996).

The equations of magnetohydrodynamics in a conservation partial differential equation form are:

$$\frac{\partial \rho}{\partial t} + \nabla \cdot (\rho v) = 0 \tag{2.102}$$

$$\frac{\partial s}{\partial t} + \nabla \cdot (sv)\, v = -\nabla p + (\nabla \times B) \times B \tag{2.103}$$

$$\frac{\partial e}{\partial t} + \nabla \cdot (ev) = -p \nabla \times v \tag{2.104}$$

and:

$$\frac{\partial B}{\partial t} = \nabla \times (v \times B) \tag{2.105}$$

where ρ is the density, v is the flow velocity, s is the momentum, p is the thermal pressure, e is the internal energy density and B is the magnetic induction (Stone & Norman, 1992b).

The form of Equation 2.105 differs from the others in that it is *surface* conservative rather than volume conservative. This form is desirable as the right hand side is a perfect curl so the divergence of it will be zero which ensures the conservation of

magnetic flux, $\nabla \cdot B = 0$ (Stone & Norman, 1992b).

As with the HD equations, the MHD equations are solved using the operator split method and separated into the source and transport steps. In the source step, s (momentum per unit volume), e (thermal energy per unit volume), gravity and dissipation are calculated. In the transport step the fluxes of the variables are transported across the zone boundaries.

The MHD equations are also solved on a staggered grid. The scalar variables, ρ and e, are 'zone-centered' and the vector variables, v and B, are 'face-centered'. This formulation is convenient as gradient components of zone-centered scalars are face-centered. Divergences of face-centered vectors are zone-centered and Curl components of face-centered vectors (J=$\nabla\times$B) are edge centered (Clarke, 1996) (see Figure 2.16).

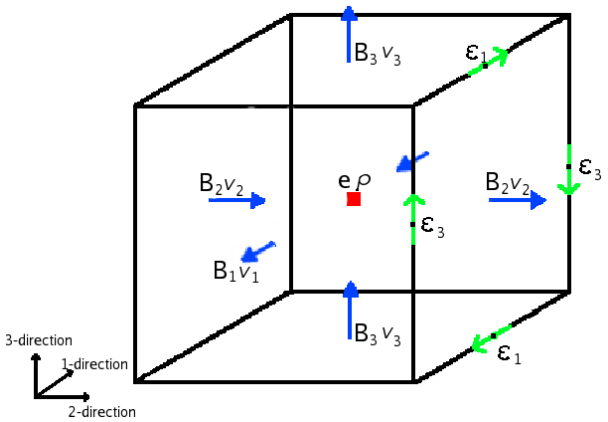

Figure 2.16: An example of a staggered grid zone in ZEUS-3D displaying the zone-centered scalar quantities of internal energy, e, and density, ρ, and the face-centered vector quantities of magnetic field, B, and velocity, v. Also shown (on one face for clarity) are the edge centered quantities of the electromotive force (emf), ϵ.

The magnetohydrodynamical algorithms of ZEUS-3D can generate toroidal, poloidal and ambient magnetic fields.

In ZEUS-3D, the magnetic field strength is set directly through the 'Plasma β' term,

$$Plasma\,\beta = \frac{P_{th}}{P_B} \tag{2.106}$$

where P_{th} is the thermal pressure and P_B is the magnetic pressure. A small Plasma β implies a strong magnetic field as the magnetic pressure would dominate over the thermal pressure. The relation between Plasma β and the actual magnetic field strength, B, in Gauss is defined in ZEUS-3D as,

$$B^2 = \frac{8\pi P}{\beta} \tag{2.107}$$

where P is the thermal pressure and β is the Plasma β. The field strengths in Gauss related to the Plasma β values used in the following test runs are displayed in Table 2.2.

Table 2.2: The magnetic field strength in Gauss for the various Plasma β values used in our test simulations.

Plasma β	B (Gauss)
1.0	1.44 μG
0.1	4.5 μG
0.01	14.4 μG
0.001	45.6 μG

2.7.1 Toroidal field

The ZEUS-3D toroidal field generator is controlled by three parameters, adjustable through the main input file:

- `betator:` This sets the minimum Plasma β of the toroidal magnetic field, or, in other words, the effective strength of the magnetic field.

- `rpeak:` This parameter sets the radial distance from the jet axis to the peak of the toroidal magnetic field profile with units in jet beam radii.

- `rsigma:` This parameter is the radial full-width at half-max (FWHM) of the toroidal magnetic field profile again in units of jet beam radii.

The effects of varying the `rpeak` and `rsigma` parameters on the toroidal magnetic field profiles can be clearly seen in Figure 2.17 which is plotted using the algorithms taken directly from the ZEUS-3D code. From Figure 2.17, it was decided to

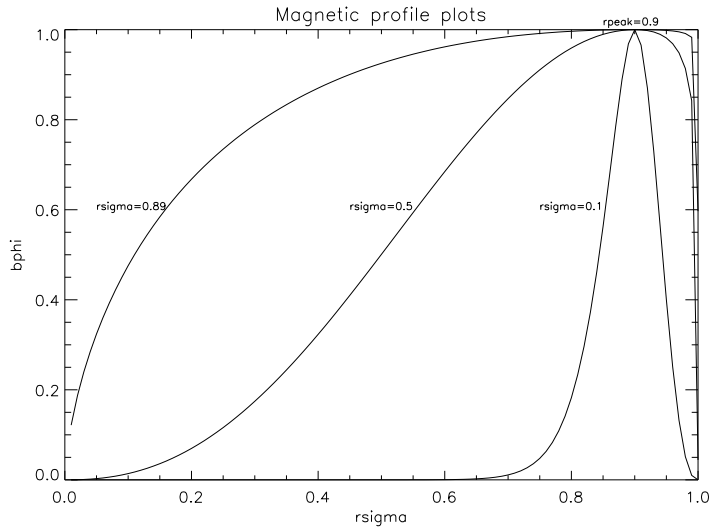

Figure 2.17: An example of toroidal magnetic field profiles. Along the x-axis, `rsigma`=0.0 signifies the center of the jet beam and `rsigma`=1.0 signifies the edge of the beam. Along the y-axis, `bphi` is proportional to the field strength ranging from maximum field strength at `bphi` = 1.0, to minimum field strength at `bphi` = 0.0.

fix `rpeak`=0.9 and `rsigma`=0.5 as they lead to a smooth profile with a maximum near the edge of the jet beam and falling almost linearly to zero at the center of the beam. This was also a similar toroidal field profile taken by Stone & Hardee (2000), thus enabling a comparison.

Figure 2.18 displays two plots with `rpeak` and `rsigma` fixed at 0.9 r_{jet} and 0.5 r_{jet} respectively and with the toroidal field strength, `betator`, set as 0.1 in Figure 2.18a, and 0.001 in Figure 2.18b. (The effective field strengths in Gauss can be seen in Table 2.2.) The jet propagation velocity in each case is 100 $\mathrm{km\,s^{-1}}$ and both the jet and ambient medium are fully molecular with the molecular cooling routines activated. The plot layout is described in the figure captions.

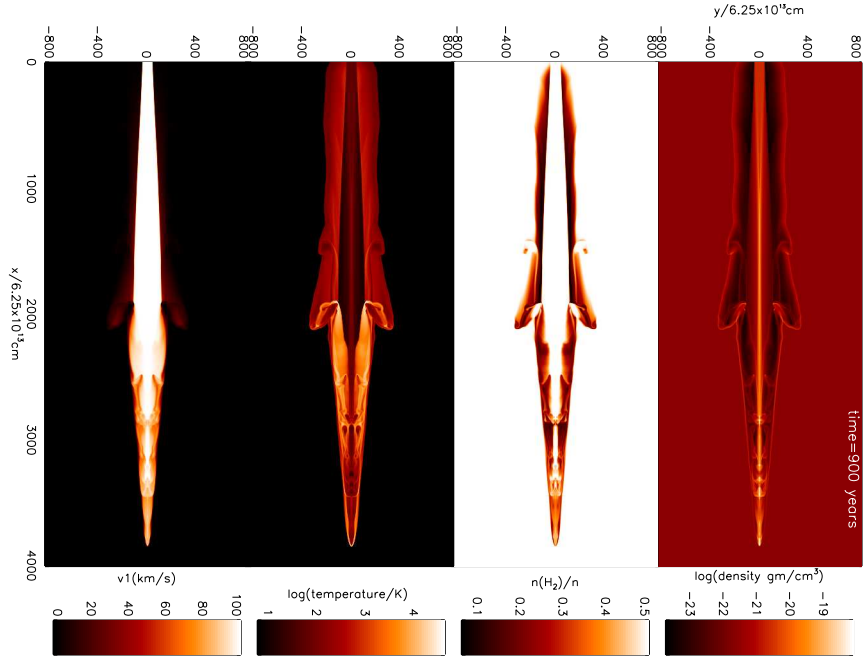

(a) `betator`=0.1

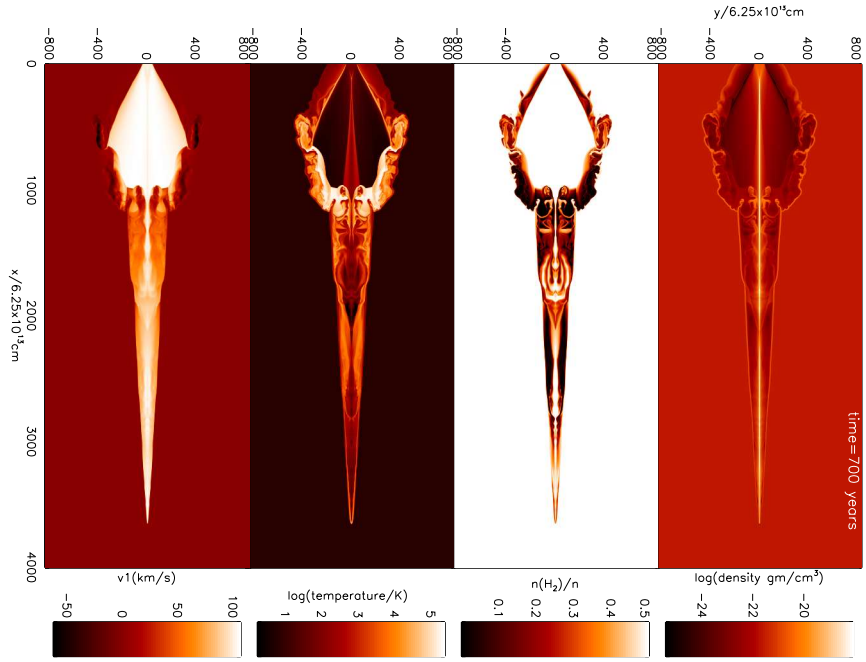

(b) `betator`=0.001

Figure 2.18: Plots of density, molecular fraction, temperature and the x-direction velocity of molecular cooled 100 $\mathrm{km\,s^{-1}}$ jets possessing a toroidal magnetic field with the parameters `rpeak` and `rsigma` fixed as 0.9 r_{jet} and 0.5 r_{jet} respectively with `betator`=0.1,(a), and `betator`=0.001,(b).

The toroidal field leads to a distinctive structure where the jet beam is forced against the axis leading to a sharp highly collimated nose-cone/bow shock. This was noted by Stone & Hardee (2000), who suggested that nose cone formation is sensitive to the geometry of the field and only occurs when the toroidal field peaks near the surface of the jet which creates 'hoop stresses' that are able to confine the nose cone. This phenomenon was also noted more recently in simulations by de Colle & Raga (2006). It is reasonable to assume that the nose cones are an artefact of the axisymmetry approximation and would be unstable in a full 3D simulations.

The strong field simulation of Figure 2.18b has created an unusual expanding cool cavity around the base of the jet that has a highly turbulent interface with the ambient medium. The simulations of Stone & Hardee (2000) also appear to have the onset of a similar expanded feature in one of their strong toroidal field runs. We can assume that this unphysical feature is another consequence of the 2D axisymmetry approximation.

The strong field of Figure 2.18b also leads to a velocity slightly higher than the constant 100 $\mathrm{km\,s^{-1}}$ jet input velocity. The extra acceleration is likely to be occurring due to the high ratio of magnetic to thermal pressure.

2.7.2 Poloidal field

A poloidal magnetic field was found to spread the jet away from the propagation axis. The stronger the field, the greater the spreading angle. The input parameters for the poloidal field generator in ZEUS-3D are similar to those of the toroidal case:

- `betapol:` This sets the Plasma β strength of the poloidal field.
- `zsigma:` This is the axial half-width at half-max (HWHM) of the leading edge of the poloidal magnetic field.
- `ibpol:` This behaves as a switch to select either one single poloidal flux loop or multiple flux loops on the grid. The positions of the multiple flux loops relative

to each other can be set by two parameters, `rnode` or `znode`. Here, we deal only with a single poloidal flux loop.

It was difficult to visualize the poloidal field and what the parameters inferred. We succeeded by plotting vectors of the two magnetic field components, B1 and B2, for a simulation with an extra large jet radius on an axisymmetric grid. This allows one to visualise the direction of field lines and understand the effect they have in modifying the flow. The result is displayed in Figure 2.19 and shows the poloidal field forms a closed loop structure.

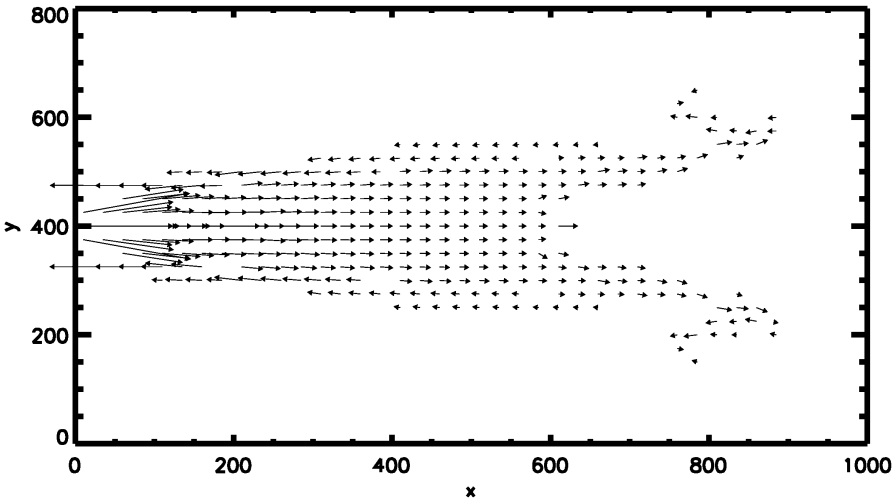

Figure 2.19: Magnetic field components B1 and B2 plotted as vectors on a large radius jet which spans 100 zones on the axisymmetric grid. Parameters: `betapol`=0.001, `zsigma`=2.5e14, 1 zone = 2.5e13 cm.

Two poloidal magnetic field runs are presented in Figures 2.20 and show a weak field with `betapol`=0.1, **left** and a strong field with `betapol`=0.001, **right**. In these simulations, `zsigma` has been fixed as 2.5×10^{17} cm, half the length of the grid. (A smaller value would have lead to the unphysical expansion evident in Figure 2.19.) Once again, the displayed simulations are based on a 100 km s^{-1} molecular jet propagating into a molecular environment.

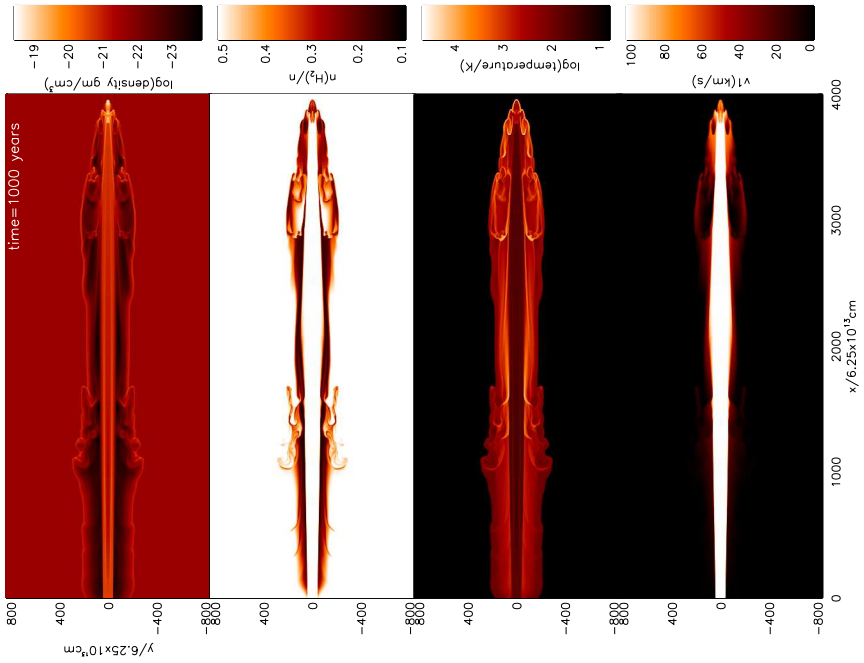

(a) `betapol`=0.1

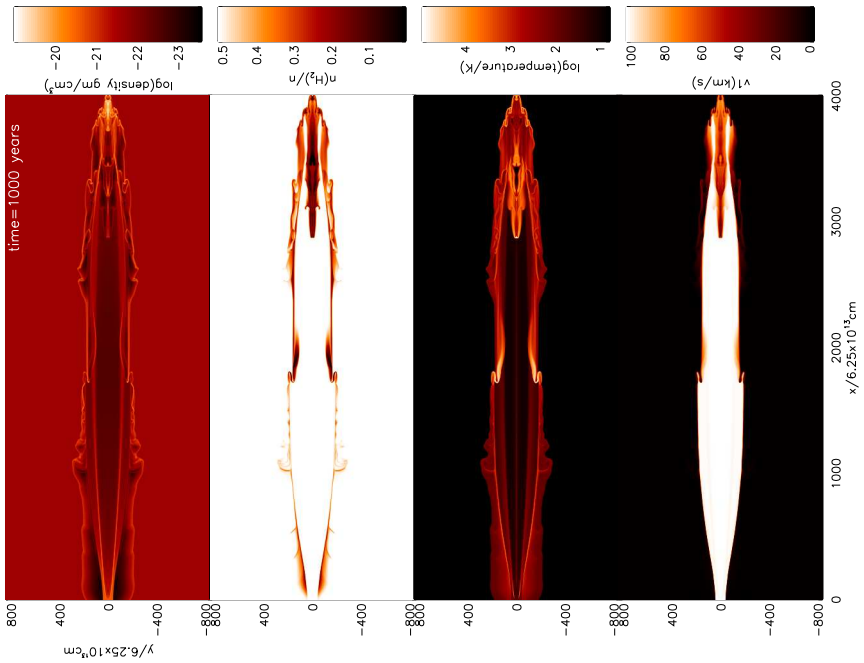

(b) `betapol`=0.001

Figure 2.20: Plots of density, molecular fraction, temperature and the x-direction velocity of molecularly cooled 100 km s^{-1} jets possessing a poloidal magnetic field with the parameters `zsigma` fixed as 2.5×10^{17} cm and `betapol`=0.1 (a), and `betapol`=0.001 (b).

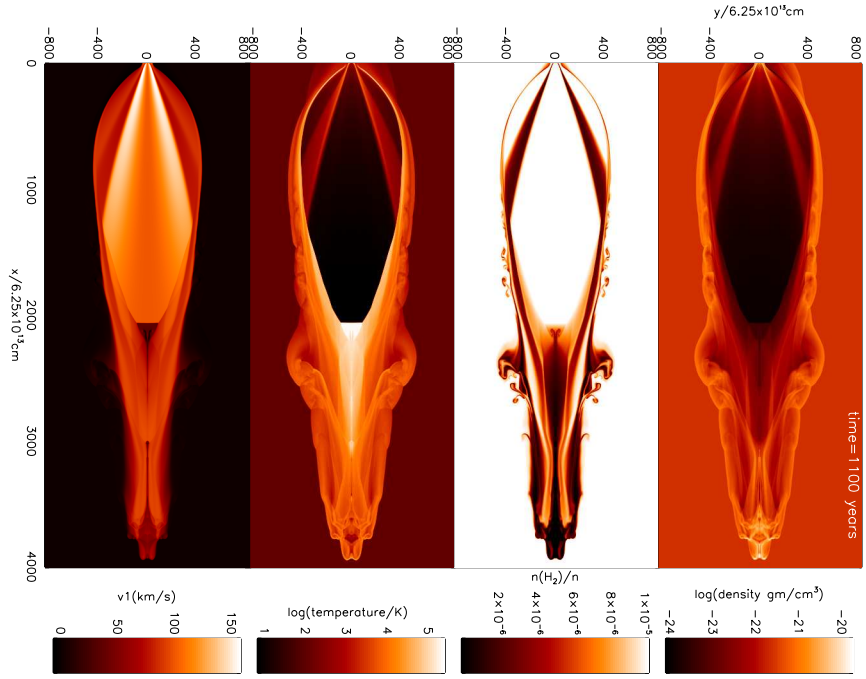

Figure 2.21: Plot of density, molecular fraction, temperature and x-direction velocity of an atomic 100 $\mathrm{km\,s^{-1}}$ jet in a poloidal magnetic with `zsigma`= 2.5×10^{17} and `betapol`=0.001.

As in the example of Figure 2.19, we see that the poloidal magnetic field encourages an expansion of the jet beam. The strong field of Figure 2.20b, has succeeded in pulling the jet beam away from the axis, which occurs after 2500 zones of propagation. The jet rejoins the axis at the end of the grid engulfing some shocked gas.

It will be noted in Chapter 3 that molecular cooling in molecular jets leads to outflow collimation. Is molecular cooling restricting the expansion effect of the poloidal field? We tested this hypothesis by performing a simulation of a 100 $\mathrm{km\,s^{-1}}$ *atomic* jet with a strong `betapol` of 0.001 to be compared directly with the *molecular* jet of Figure 2.20b. The result is presented in Figure 2.21 where we see a very large laterally expanding cool cavity propagating faster than the 100 $\mathrm{km\,s^{-1}}$ input speed. Therefore, molecular gas does keep the expansion in check through cooling which maintains a lower temperature and sound speed.

Overall, the limits of axisymmetry become apparent in these simulations where the effects of the magnetic fields on the jet beam are hampered by the existence of the symmetry axis. It suggests MHD jet propagation simulations would be better suited to full 3D grids despite the high computational overheads entailed by the combination of large spatial domains, molecular chemistry routines and MHD algorithms.

It should be noted here that the accuracy of the ZEUS-3D was brought into question by Falle (2002) who claimed, that under certain circumstances, ZEUS-3D can generate rarefaction shocks and other shock errors. The author suggested that rarefaction shocks may occur and were due to the operator splitting scheme of ZEUS-3D reducing the second-order accurate coding to first order accuracy, but they could be removed by setting the linear viscosity (see Section 2.3.6), qlin, to at least 0.25.

The author also noted that ZEUS-3D did not compare well to other upwind codes by producing apparent shock errors in some 1D MHD problems while using an adiabatic equation of state. Although the author acknowledged that these shock errors were absent in ZEUS-3D if using an isothermal equation of state, the non-conservative ZEUS-3D code should not be compared directly with the results of a conservative upwind code. The problem is negligible in our molecular cooling simulations as the flows are isothermal (Rosen & Smith, 2003).

It is believed that the rarefaction shocks only appear in certain specialised 1D shock problems. In Falle (2002), the shock fronts were resolved by about 30 zones. In the large scale multi-dimensional simulations presented in this thesis, the individual shock fronts would be resolved by less zones. Furthermore, we use an artificial viscosity, and thus limit the shock fronts to two zones in width (see Section 2.3.6). It would also be un-physical to use the suggested fix of setting the linear viscosity to 0.25 in our simulations as this would add viscosity over the entire computational domain and not just at the shock fronts. Additionally, we do not employ the base ZEUS internal energy equation as used by Falle (2002). Our energy equation is a modified version which allows for an effective energy loss required for the molecular cooling to occur. In our

simulations, the cooling is so dominant that even if rarefaction shocks were to occur, their influence on the simulations would be negligible as the energy dissipated in the rarefaction shocks is small and only important in energy-conserving adiabatic shocks.

2.8 Mass-Velocity

Mass-velocity distributions are frequently used to explore how momentum is transferred from the jet to the ambient medium. They are approximated by the the following power-law function, commonly referred to as the mass spectrum,

$$\frac{dm}{dv_r} \propto v_r^{-\gamma} \tag{2.108}$$

in which m is the spatially integrated outflow mass as a function of radial velocity, v_r. The exponent, γ, represents a negative slope of the resulting spectrum when displayed as a log-log plot.

Observationally, the mass, m, is deduced from the intensities of low-rotational optically thin CO spectral lines, e.g.Yu et al. (2000). Very often observations show broken power laws, consisting of two distinct sections; a shallow slope at low velocities connecting to a steeper slope at high velocities through a 'break-point'. Careful ambient cloud subtraction is necessary in order to correctly estimate the low velocity component (Yu et al., 2000; Arce & Goodman, 2001). This can be clearly seen in Figs. 13 and 14 of Yu et al. (2000) (Reproduced here as Figures 2.22 and 2.23) where two slopes with a break point are revealed after the ambient cloud subtraction. In bow shock theory, the break velocity may correspond to the projected component of the molecular dissociation velocity.

Mass-velocity plots from simulations are easier to obtain than those from observations as there is no confusion or uncertainty from factors such as optical depth, ambient cloud motion or overlap with other flows. Gamma values have been predicted from

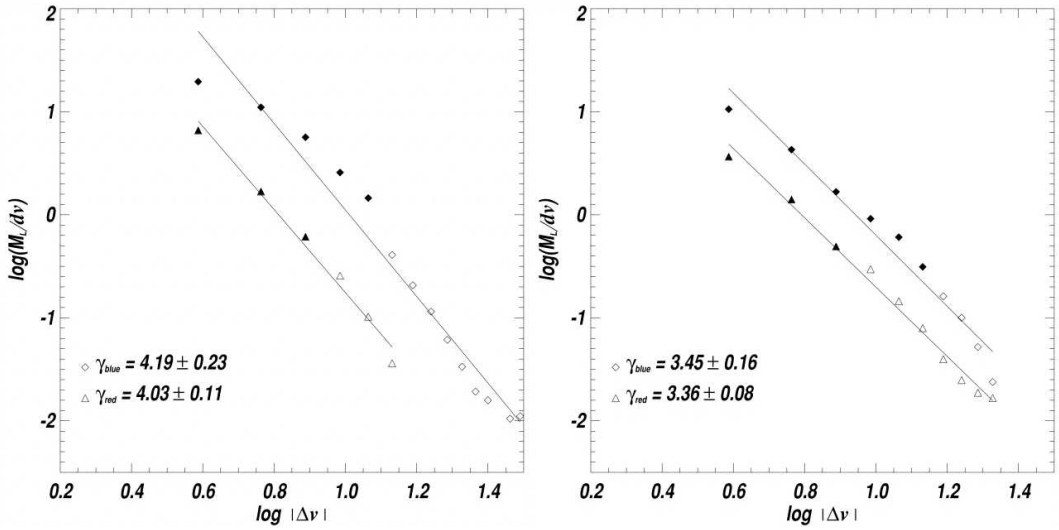

Figure 2.22: A reproduction of Figure 13a and 13b of Yu et al. (2000). It is an observational mass velocity plot of the west (left) and east (right) lobes of the OMC-2/3 outflow with no ambient cloud subtraction. Plotted are measurements from both red-shifted and blue-shifted material with mass from ^{13}CO shown filled points and mass from ^{12}CO shown as outline points.

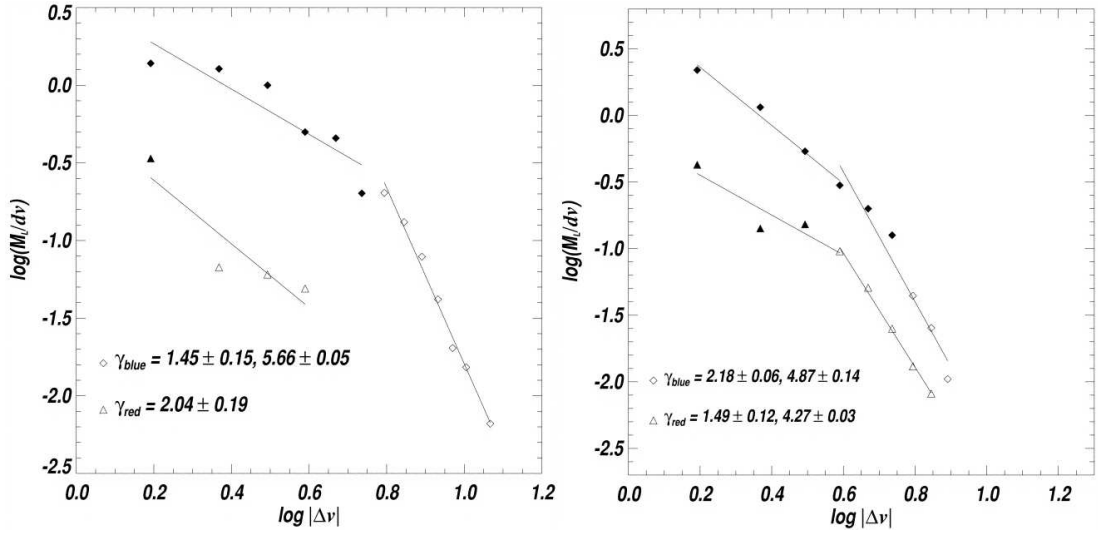

Figure 2.23: A reproduction of Figure 14a and 14b of Yu et al. (2000). The layout is the same as Figure 2.22 but the effects of ambient cloud material has been subtracted. It leads to steeper high velocity components.

various simulations and almost always found to be dependent on the viewing angle, e.g. Rosen & Smith (2004b). This is due to the fact that the viewing angle stretches or compresses the velocity range while holding constant the range of mass between the

two velocity extrema. As noted in Section 3.2.1, we did not find this viewing angle dependence to hold in general for our simulations. Recently, Smith & Rosen (2007) found that jet rotation leads to a lower value of γ.

Shallow spectra ($\gamma < 2$) were predicted in works by Smith et al. (1997), Downes & Cabrit (2003) and Keegan & Downes (2005). The latter performed long duration simulations to find that γ does not increase indefinitely but eventually levels out after 1500 years. Wind driven outflows, as opposed to jet driven outflows, were found to lead to smaller γ values in Lee et al. (2001).

Mass spectra with intermediate slopes ($2 < \gamma < 4$) were found by Downes & Ray (1999). They also noted an increase of γ with decreasing jet molecular abundance. This suggests that most jets may be atomic, a case explored in the following Chapters. Taking an atomic jet also allows us to easily reduce the jet contribution towards the total molecular mass in motion by a factor of 10^5 to effectively only count ambient material set in motion. (The total mass in motion is plotted as the dotted line on the mass-velocity profile plots.)

Steep mass spectra ($\gamma > 4$) along the full velocity range are not found in numerical simulations, but can be noted in some simulations at the higher radial velocity region of the spectra.

2.8.1 ZEUS-3D mass-velocity routine

Our mass-velocity routine operates by reading in the 2D-axisymmetric data and rotating it around the azimuthal direction to create a quasi-3D outflow. Due to the symmetry, we need only rotate half way, 180°, thus reducing the computation and integration times required. The final mass is simply doubled at the end. The semi-cylinder is then divided into a series of slices along the jet axis, z, and then segments by divisions along the radial direction, r. The projected velocity of each segment at the chosen viewing angle out of the plane of the sky, α, is calculated and placed into a series of

velocity bins. With this method, material from the jet beam is included and forms a sharp peak at the highest radial velocity, $|V_{rad}|$, extent of $v_{jet} \sin \alpha$.

A sample mass-velocity plot of the type we create from our simulations is displayed in Figure 2.24. Here, the dotted line represents *total* mass in motion on the grid whereas the solid line represents *molecular* mass in motion. The jet beam peak does not appear in this instance as we use an atomic jet (see Section 3.1).

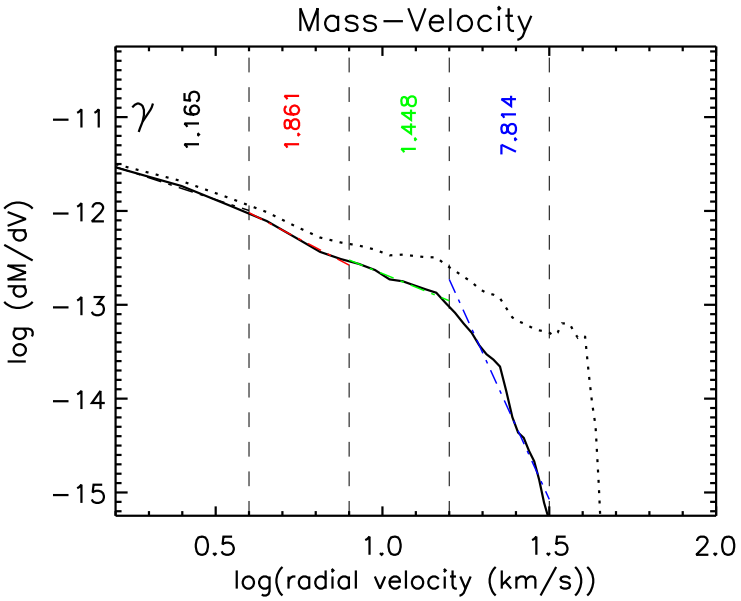

Figure 2.24: A typical mass-velocity figure that we obtain from our simulations in order to link simulation with observation. The log of mass/velocity is plotted against the log of radial velocity. By plotting in this manner, the negative slope of the resulting line plot is the γ value. The dotted line represents the total mass in motion whereas the solid represents molecular mass in motion. This particular mass-velocity plot is from a simulation containing a velocity gradient in the beam (see Section 4.6). The existence of a carefully controlled velocity gradient in the jet beam removes the high velocity mass peak from the plot and leads to a greater resemblance to observational mass-velocity plots which typically do not display the high velocity jet beam component.

In all the mass-velocity plots presented in the following chapters, we calculate the resultant mass-velocity γ values across four fixed velocity ranges: 2–4 $\mathrm{km\,s^{-1}}$, 4–8 $\mathrm{km\,s^{-1}}$, 8–16 $\mathrm{km\,s^{-1}}$ and 16–32 $\mathrm{km\,s^{-1}}$, referred to as velocity intervals 'A','B','C' and 'D' respectively. This leads to objective values of γ which are automatically calculated during the simulations and can be compared directly with other runs and viewing angles. The

values of the slopes determined over the four intervals are displayed on the diagrams.

In the first study in Chapter 3, we had yet to incorporate the routine directly into ZEUS-3D. The routine read the data from the HDF output files. Plotting a 'γ vs time' plot, which compares how the slope at the four velocity intervals varies with time, was not feasible due to the amount of full data sets required if suitably smooth plots were to be created. For the later study in Chapter 4, we therefore incorporated the entire routine into ZEUS-3D and thus were able to easily calculate the mass-velocity at any time without needing to depend on the HDF data dumps. The γ values of the four velocity intervals were output every 'year' of simulation time. Hence we were able to create high time-resolution plots showing how the γ values evolved with time.

Chapter 3

Velocity and Compositional Study of Protostellar Jets

Jets penetrate through obscuring gas cores to be detected in the extended environments of protostars (Reipurth & Bally, 2001). Although continuous jets are rarely uncovered, infrared and optical observations have revealed distinct chains of knots and aligned bow shocks which suggest that they are more or less continuously supplied by collimated supersonic jets (Stanke et al., 2002; Khanzadyan et al., 2004; McGroarty et al., 2004). These jets are of high thrust and so are capable of evacuating cavities by sweeping up and deflecting the ambient medium. They may thus be held responsible for forming bipolar nebulae and bipolar outflows (Bachiller, 1996). The bipolar outflows are collimated to various degrees and often extend to parsecs from the launching protostar (Richer et al., 2000; McGroarty et al., 2004).

One specific problem emphasized recently is that the rate of flow of jet momentum may not be sufficient to supply the bipolar outflows (Su et al., 2004). This may be related to basic questions concerning the content of the jets, their launch mechanism and the properties which allow them to propagate so far. To help find answers, numerical simulations have been executed which probe the relationship between the most probable

jet properties and the observed outflow properties. To study the penetration, we assume that a supersonic jet has already been established but has not yet entered the extended envelope (e.g. Smith, 2003). In this chapter, we present simulations which include radiative cooling and chemistry and examine the influence of the initial jet speed and molecular fraction.

Previous investigations of relevance have included a combination of radiative cooling, chemistry and magnetic field. Those restricted to atomic cooling processes include Blondin et al. (1990); Stone & Norman (1993, 1994); Biro & Raga (1994); Frank et al. (1998); Cerqueira & de Gouveia dal Pino (1999); Gardiner et al. (2000); Stone & Hardee (2000); Lee et al. (2001). On the other hand, powerful molecular jets occur in the earliest protostellar (and proto-planetary nebula) stages. Simulations which include molecular and atomic cooling, as well as some chemistry, are Raga et al. (1995); Suttner et al. (1997); Downes & Ray (1999); Völker et al. (1999); O'Sullivan & Ray (2000); Downes & Cabrit (2003); Rosen & Smith (2003, 2004a); Smith & Rosen (2005a). In general, the simulations have provided reasonable interpretations for many of the observed outflows as well as considerable insight into their dynamics and global evolution.

Each of the above-mentioned studies, however, considered a single nominal jet speed albeit with various pulsation and precession criteria. The chosen speed has ranged between 100 $\mathrm{km\,s^{-1}}$ (e.g. O'Sullivan & Ray, 2000) to 332 $\mathrm{km\,s^{-1}}$ (e.g. Stone & Hardee, 2000). The question that remains to be answered is thus: *can we constrain the jet speed from the outflow structure?*. This is critical to answer since we might expect that the jet speed systematically increases with time in proportion to the escape speed as a protostar builds up at, perhaps, constant density. On the other hand, the jet gas may switch from molecular to atomic as the mass available through accretion falls (e.g. Smith, 2000). Therefore, we present eleven simulations to cover these possibilities and so provide a basis from which to extract the signatures as jets gradually evolve from low speed to high speed and molecular to atomic. Then, for a quantitative comparison, we examine the mass spectra of the simulations.

The simulations are performed on a two-dimensional axisymmetric uniform grid with a jet (hydrogen nucleon) density of 10^3 cm^{-3} (see Table 3.1). With these assumptions, we are able to reach a much higher resolution of the radiative layers behind shock waves than in previous works which were in 3D with typical jet densities of 10^5 cm^{-3} (Rosen & Smith, 2003).

3.1 Method

For this study we used our modified version of ZEUS-3D with the molecular and atomic cooling functions activated (See Section 2.5). We initially checked the modified code against the adiabatic and atomic simulations presented by Stone & Hardee (2000), finding general agreement of the global flow pattern although individual features vary in the highly turbulent flow in and around the jet head (note that our cooling functions are more complete at lower temperatures). We set our initial and boundary conditions similar to those of Stone & Hardee (2000). Further fine-scale structure appears in our simulations due to the higher resolution. Stone & Hardee (2000) ran 2D axisymmetric simulations on a grid of 2000×400 zones while we take 4000×800 zones, maintaining the same initial jet radius, $\mathrm{R}_j = 2.5 \times 10^{15}$ cm and overall spatial dimensions.

Hence there are 40 zones per jet radius, 20 jet radii in the radial direction and 100 jet radii in the axial direction. Therefore, the actual extent of the grid is (2.5×10^{17} cm) $\times$ (5×10^{16} cm).

We model a heavy (i.e. ballistic) jet in all cases. The ambient medium density is set to 100 cm^{-3} and the jet density is set to 1000 cm^{-3} so the introduced jet is over-dense with respect to the ambient medium by the factor $\eta = \rho_j/\rho_a = 10$.

In our molecular simulations the molecular hydrogen abundance in both the jet and the ambient medium is set to 0.5 (fully molecular). The abundances of free carbon and oxygen are both set to 10^{-4}. The temperature of the ambient medium is set to 10 K and that of the jet is 100 K. In all cases the jet is over-pressured with respect to the

Table 3.1: Summary of parameters in the atomic v. molecular runs.

property	Atomic	Molecular
density, d_{amb} (gm/cm^3)	2.342×10^{-22}	2.342×10^{-22}
sp. energy, e_{amb} (ergs/K)	2.278×10^{-12}	1.933×10^{-13}
n(H_2/n)	1.000×10^{-5}	5.000×10^{-1}
sp. heat ratio, γ	1.6667	1.4286
temperature, T_{amb} (K)	100	10
temperature, T_{jet} (K)	1000	100
Mach number, M_{jet} :		
50 km/s	15.21	70.33
100 km/s	30.42	140.67
200 km/s	60.83	281.34
300 km/s	91.25	422.00

ambient medium by the factor $\kappa = P_j/P_a = 100$.

In our atomic simulations we retain all the cooling functions activated but greatly reduce the densities of molecular species. The molecular hydrogen fraction is now 10^{-5} and our abundances of carbon and oxygen are 10^{-6}. This ensures that the atomic radiative cooling approximation controls the cooling.

The four jet velocities chosen are:

- a very slow jet, 50 km s^{-1};
- a slow jet, 100 km s^{-1};
- an intermediate jet, 200 km s^{-1}:
- and a fast jet, 300 km s^{-1}.

The actual input parameter which ZEUS converts into a jet speed is the Mach number ($M_{jet} = V_{jet} / c_{jet}$). It depends on the sound speed in the jet c_{jet} which is significantly higher in the atomic jet (3.29 km s^{-1}) than in the molecular jet (0.711 km s^{-1}).

3.2 Results

Figures 3.1a to 3.4b contain visualizations of the eight basic atomic jet/atomic ambient and molecular jet/molecular ambient simulations at the four jet velocities. Each plot consists of four panels with a colour gradient scaling. We shall use the following naming convention in order to label the runs: 50A, 100A, 200A and 300A for the 50, 100, 200 and 300 $\mathrm{km\,s^{-1}}$ atomic runs, respectively, and 50M, 100M, 200M and 300M for the equivalent molecular runs.

An additional molecular jet/atomic ambient medium run will be labelled as MJAA (Figure 3.5a) and two additional atomic jet/molecular ambient medium runs will be labelled as AJMA for a 100 $\mathrm{km\,s^{-1}}$ jet (Figure 3.5b) and AJMA50 for a 50 $\mathrm{km\,s^{-1}}$ jet (Figure 3.6).

The main figures of Chapter 3 display the following information:

- The upper panels display the mass density plotted on a logarithmic scale. Also shown is the time in years corresponding to the displayed distributions, just before each jet has reached the end of the grid.

- The second panels display the temperature, again on a logarithmic scale.

- The third panels trace the molecular fraction or, more precisely, the ratio of hydrogen molecules to the total number of hydrogen nuclei ($\mathrm{n(H_2)/n}$). Note that the distribution of molecular fraction in both the atomic and molecular runs appears similar at first glance. Molecular cooling does actually take place in the atomic cases but the quantities of molecular material are many times smaller. As seen from the scale bars, the molecular density is 100,000 times less in the atomic cases.

- The lower panels display the axial component of velocity in $\mathrm{km\,s^{-1}}$. This clearly shows the expansion and extent of the jet beam.

High resolution electronic versions of the figures are available on the included optical disk.

The most dramatic contrast between the atomic and molecular runs occurs at the lowest speed of 50 km s^{-1} (Figures 3.1a and 3.1b). Here, the relatively low Mach number of the atomic jet is responsible for a high transverse jet expansion. This leads to the blow-torch structure at the jet inlet and the high density gradient along the jet axis (upper panel). The result is that the leading edge of the outflow decelerates with an average speed of advance of $\sim$ 26.4 km s^{-1}.

The termination shock of the atomic jet takes the form of a large Mach disc which generates warm atomic gas. This gas is slow to cool for the chosen density, thus (i) supporting the Mach disk and (ii) forming the wide low-density cavity of temperature 3,000 – 8,000 K (second panel). However, at considerably higher densities, further cooling mainly through gas–grain collisions will cool the gas down to $\sim$ 1,000 K on a timescale of 10^8/n years (Smith & Rosen, 2003), reducing the cavity size. The cavity also contains wisps of hot shocked gas within which small quantities of residual molecules are also destroyed (third panel). The displayed axial velocity illustrates the low advance speed of $\sim$ 20 km s^{-1}, as well as a back-flow (negative v1, see scale bar to the fourth panel) typical of under-dense jets.

On the other hand, the low speed molecular jet (with Mach number of 70) displays only moderate expansion (lower panel). As a consequence, the advance of the leading edge is maintained with an average speed of $\sim$ 38.6 km s^{-1}. However, the region where the jet terminates is complex. A nose develops where the jet material becomes focused towards the axis (such structure is also present in three dimensional Cartesian simulations of molecular jets (Rosen & Smith, 2003)). The strong molecular cooling does not allow a Mach disk to develop but leads instead to oblique shocks. The cavity is also narrow because of the maintained collimation and the high advance speed. Therefore, unlike the atomic case, no back-flow in the cavity arises (lower panel).

At 100 km s^{-1} (Figures 3.2a and 3.2b), the low-speed features are still apparent in a

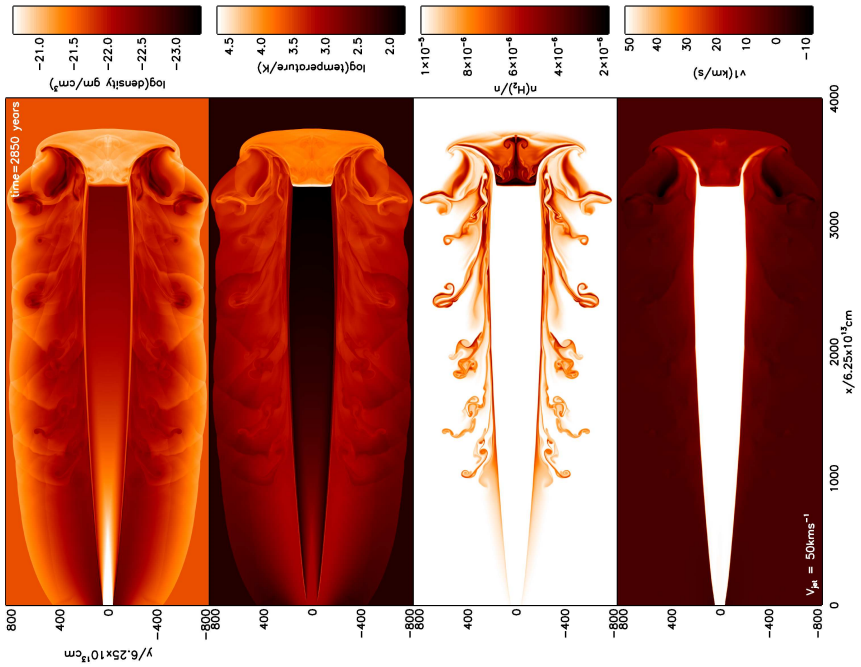

(a) 50 km s^{-1} atomic jet into atomic ambient medium (50A)

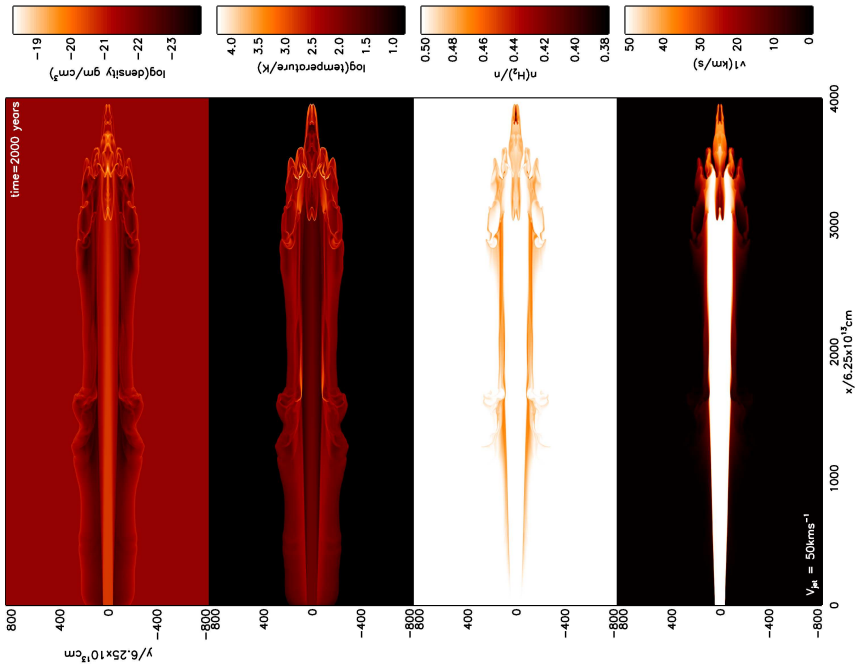

(b) 50 km s^{-1} molecular jet into molecular ambient medium (50M)

Figure 3.1: Cross-sectional distributions of physical parameters generated by, (a) an atomic jet of speed 50 km s^{-1} propagating into an atomic medium (50A) and, (b) a molecular jet of speed 50 km s^{-1} propagating into a molecular medium (50M). As labelled, the parameters shown are the mass density (gm cm^{-3}), temperature, molecular fraction and axial speed from top to bottom. The lower half of each distribution is the mirror image of the top half.

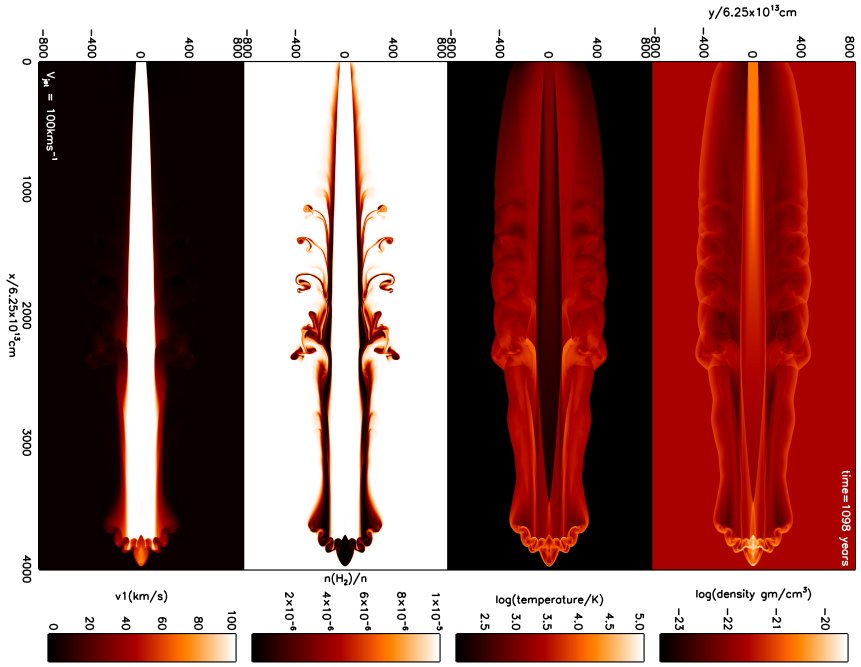

(a) 100 km s^{-1} atomic jet into atomic ambient medium (100A)

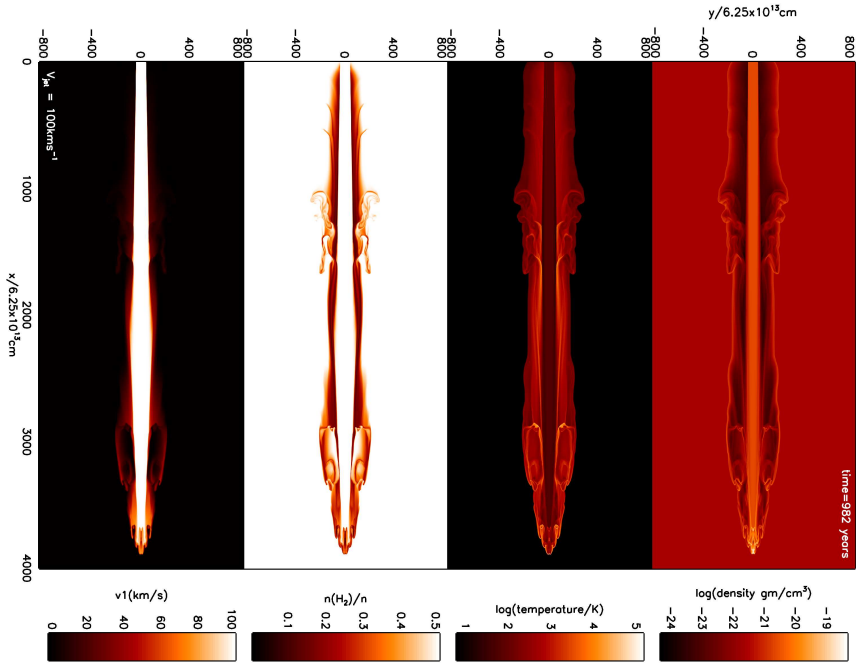

(b) 100 km s^{-1} molecular jet into molecular ambient medium (100M)

Figure 3.2: Cross-sectional distributions of physical parameters generated by, (a) an atomic jet of speed 100 km s^{-1} propagating into an atomic medium (100A) and, (b) a molecular jet of speed 100 km s^{-1} propagating into a molecular medium (100M). As labelled, the parameters shown are the mass density (gm cm^{-3}), temperature, molecular fraction and axial speed from top to bottom. The lower half of each distribution is the mirror image of the top half.

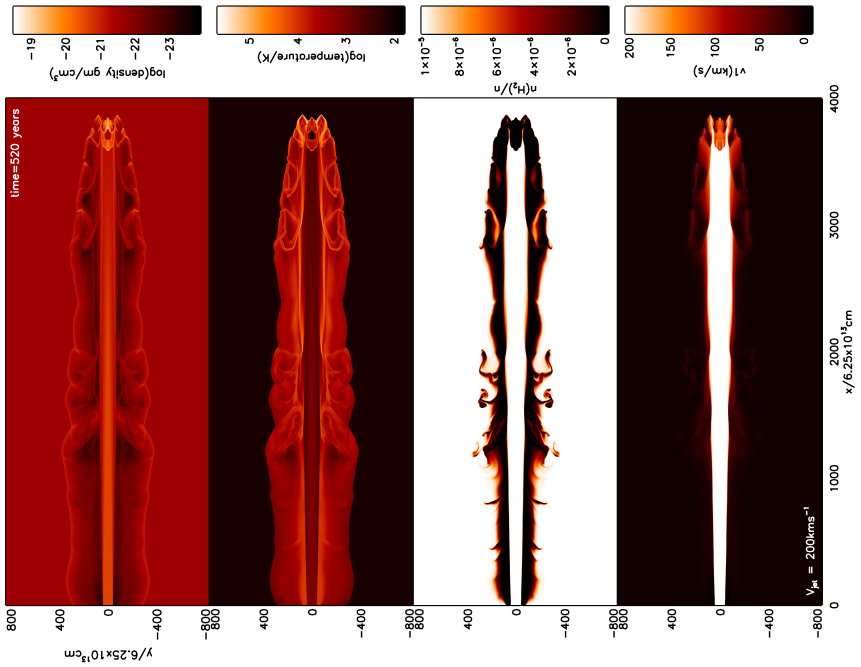

(a) 200 km s^{-1} atomic jet into atomic ambient medium (200A)

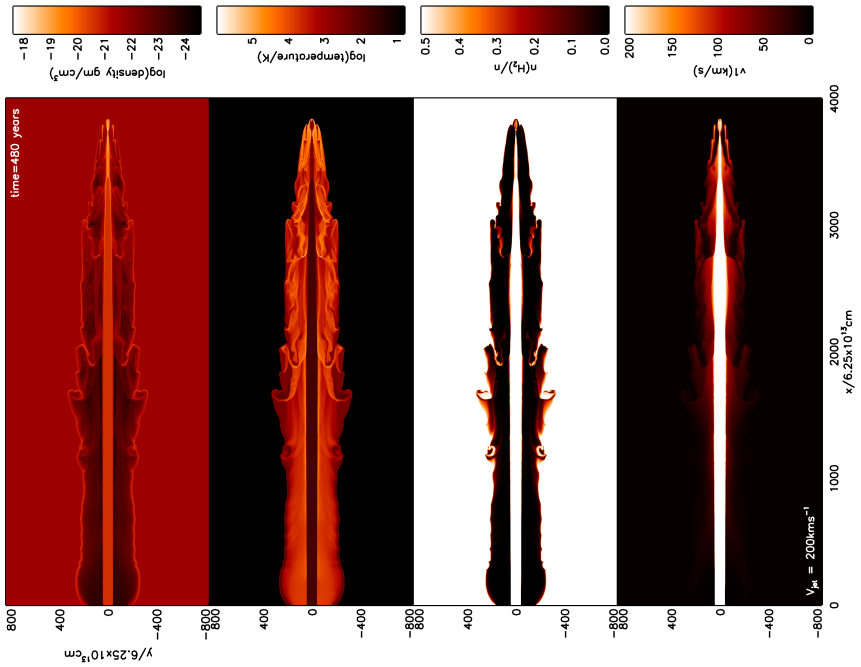

(b) 200 km s^{-1} molecular jet into molecular ambient medium (200M)

Figure 3.3: Cross-sectional distributions of physical parameters generated by, (a) an atomic jet of speed 200 km s^{-1} propagating into an atomic medium (200A) and, (b) a molecular jet of speed 200 km s^{-1} propagating into a molecular medium (200M). As labelled, the parameters shown are the mass density (gm cm^{-3}), temperature, molecular fraction and axial speed from top to bottom. The lower half of each distribution is the mirror image of the top half.

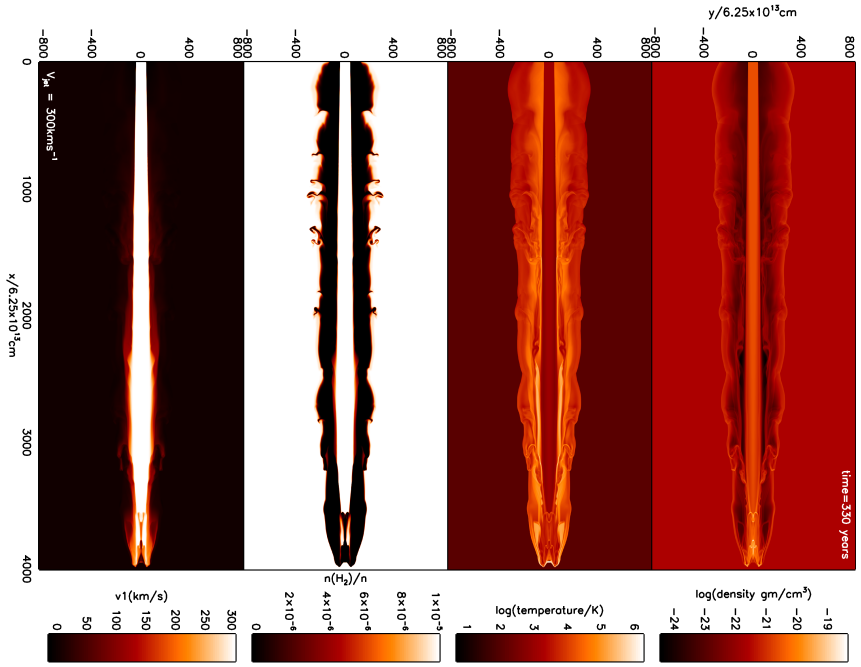

(a) 300 km s^{-1} atomic jet into atomic ambient medium (300A)

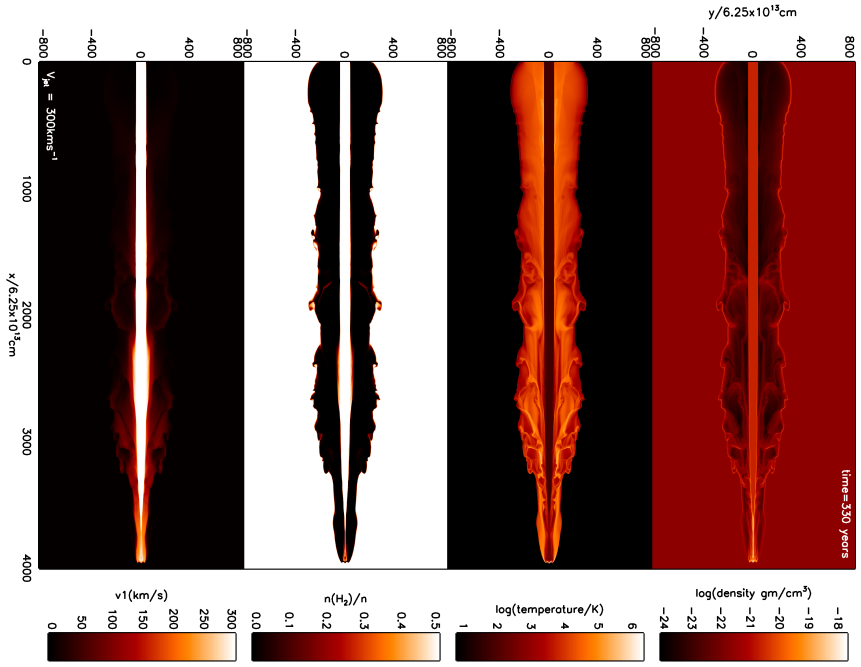

(b) 300 km s^{-1} molecular jet into molecular ambient medium (300M)

Figure 3.4: Cross-sectional distributions of physical parameters generated by, (a) an atomic jet of speed 300 km s^{-1} propagating into an atomic medium (300A) and, (b) a molecular jet of speed 300 km s^{-1} propagating into a molecular medium (300M). As labelled, the parameters shown are the mass density (gm cm^{-3}), temperature, molecular fraction and axial speed from top to bottom. The lower half of each distribution is the mirror image of the top half.

diluted form. The atomic simulation generates a cavity of roughly half the size of the lower speed case. The Mach disk is fragmentary and no back-flow occurs. The cavity in the molecular simulation is more pointed in shape. A prominent 'shoulder' occurs causing jet expansion followed by focusing. This results in a remarkable vortex-like structure in the cavity, as prominent in the molecular fraction panel. An oblique shock is present between the vortex and the jet (see top and second panels of Figure 3.2a) which results in the jet focusing.

At 200 km s^{-1} (Figures 3.3a and 3.3b), expansion of the atomic jet is not prominent and the average advance speeds of the atomic jet is only ten per cent higher than that of the molecular jet. Both cavities are narrow and the cavities now almost exclusively contain atomic gas in both cases. The main difference is that the refocusing shoulders remain in the molecular jet while the leading edge of the atomic jet is a blunt structure, inflated by warm shocked atomic gas.

At 300 km s^{-1} (Figures 3.4a and 3.4b), the collimation is slightly improved in both cases. High speed atomic jets also display a hotter sheath to the jet. However, while small-scale structure near the jet heads differ, the global outflow structures are quite similar.

We ran three additional simulations, one of a molecular jet propagating into an atomic medium at 100 km s^{-1} (MJAA, Figure 3.5a) and two of an atomic jet propagating into a molecular medium at 100 km s^{-1} (AJMA, Figure 3.5b) and 50 km s^{-1} (AJMA50, Figure 3.6). The standard parameters from Table 3.1 were used and they can be most closely compared to the other 100 km s^{-1} jets in Figures 3.2a and. 3.2b and to the 50A jet in Figure 3.1a. Of these additional simulations, AJMA and AJMA50 contain the most significant difference from the 100A and 50A runs, atomic jets moving through an atomic media. Although the jet has expanded, the cavity is very narrow. The Mach disk is replaced by oblique shocks as ambient molecular material gets trapped near the jet axis. The MJAA simulation has a narrower jet beam than the 100M run. The hotter cavity is responsible for confining a more uniform jet. The cavity itself is

slightly wider and conical.

To summarise, atomic jets are terminated by either a Mach disk or by deflection away from the jet axis. Molecular jets tend to be focussed towards the axis, by oblique shocks, producing shouldered structures and narrow advancing noses. Much of the global structure is related to the Mach number of the jet flow which determines the transverse expansion until the cavity pressure can provide resistance. Thus high Mach number jets generate narrow cavities. Note the similarity in the global structure of 200A and 50M including the width of the jets where the terminal Mach disks occur. This results from the similar jet Mach numbers of these two simulations. At jet speeds in excess of 100 km s^{-1} the entire cavity is filled with atomic gas. Below this value, the cavity can be occupied by both molecular and atomic material.

3.2.1 Distribution of mass with velocity

We calculated mass spectra for the atomic and molecular runs at the four jet speeds for five viewing angles, α, out of the plane of the sky: 15°, 30°, 45°, 60° and 90°. We examined the resultant mass-velocity power law slopes across the four fixed radial velocity ranges: 2–4 km s^{-1}, 4–8 km s^{-1}, 8–16 km s^{-1} and 16–32 km s^{-1}, hereafter referred to as velocity intervals 'A','B','C' and 'D' respectively. This leads to objective values of γ which can be compared directly with other runs and viewing angles. Table 3.2 contains the γ values for the runs at all the viewing angles and we display the mass spectra for the 45° viewing angle in Figure 3.7.

The power-law fits for the 16–32 km s^{-1} range (interval D) are not always useful as it is generally too fast at small viewing angles and low jet velocities. Intervals B and C provide consistent and comparable data. Note that the viewing angles of 15° and 90° do not follow completely systematic γ values whereas the intermediate angles, 30° to 60°, show systematic trends.

The mass spectra display expected features. The higher the jet velocity, the further

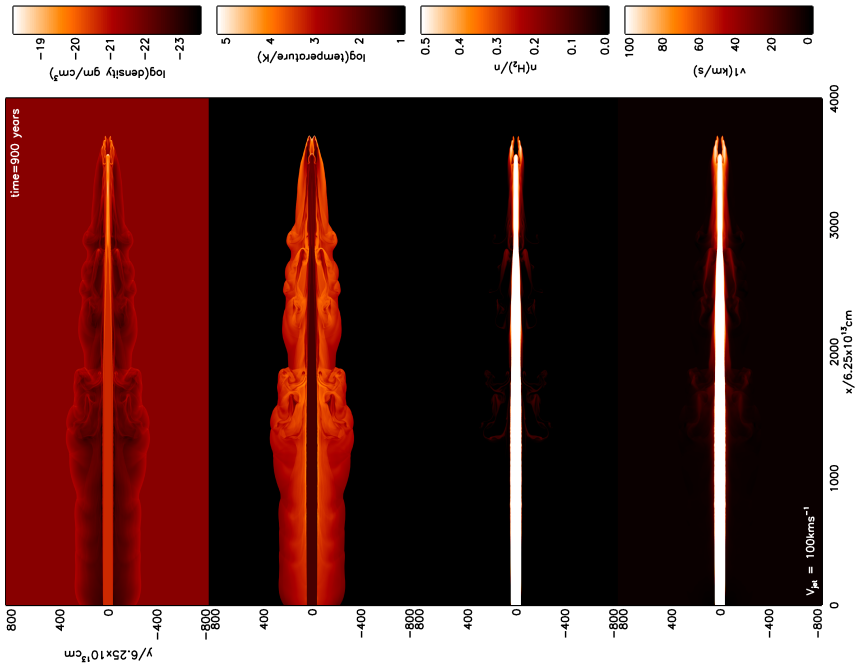

(a) 100 km s^{-1} molecular jet into atomic ambient medium (MJAA)

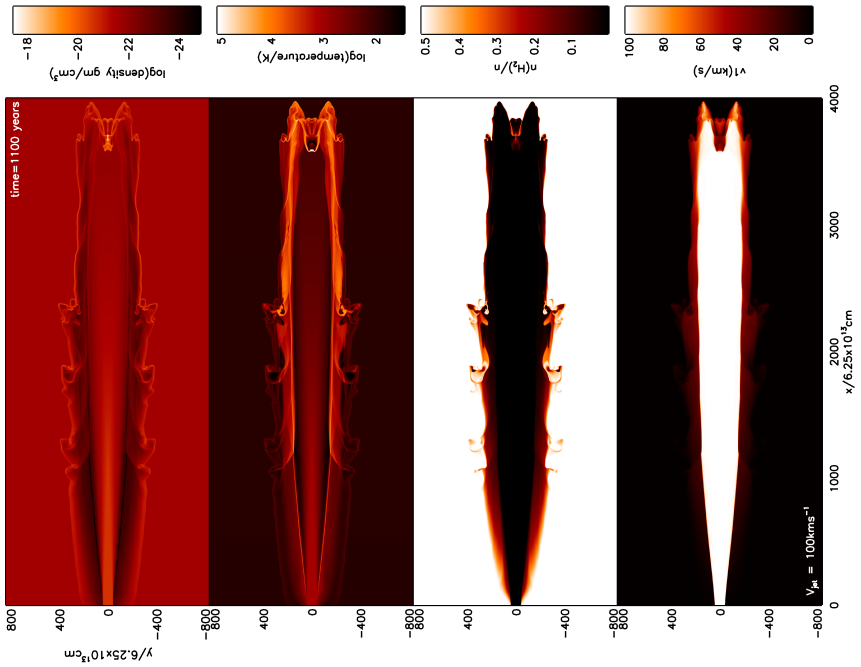

(b) 100 km s^{-1} atomic jet into molecular ambient medium (AJMA)

Figure 3.5: Cross-sectional distributions of physical parameters generated by, (a) a molecular jet of speed 100 km s^{-1} propagating into an atomic medium (MJAA) and, (b) a molecular jet of speed 100 km s^{-1} propagating into an atomic medium (AJMA). As labelled, the parameters shown are the mass density (gm cm^{-3}), temperature, molecular fraction and axial speed from top to bottom. The lower half of each distribution is the mirror image of the top half.

Table 3.2: The estimated 'gamma' values for the molecular and atomic runs at a viewing angle of 45° out of the plane of the sky. 'A' represents the range 2–4 km s^{-1}, 'B' represents the range 4–8 km s^{-1}, 'C' represents the range 8–16 km s^{-1} and 'D' represents the range 16–32 km s^{-1}. The '$\varkappa$' entries replace nonsensical results where the local conditions caused a poor line fit.

Angle		γ:	A	B	C	D		A	B	C	D
	Run						Run				
15°	50A		1.527	4.318	$\varkappa$	3.647	50M	0.781	0.585	2.978	$\varkappa$
	100A		1.423	3.176	0.551	$\varkappa$	100M	2.062	0.826	1.416	$\varkappa$
	200A		0.611	2.001	1.649	$\varkappa$	200M	1.516	1.083	1.804	1.292
	300A		0.148	1.270	3.309	0.718	300M	$\varkappa$	2.079	1.481	2.085
30°	50A		1.800	1.432	4.936	$\varkappa$	50M	1.138	0.595	0.226	$\varkappa$
	100A		1.440	2.676	0.573	0.701	100M	1.907	1.988	0.134	0.986
	200A		0.982	1.928	1.563	1.511	200M	1.894	1.372	1.379	1.395
	300A		0.174	1.478	3.230	1.597	300M	$\varkappa$	2.170	1.346	1.739
45°	50A		2.61	0.191	6.84	$\varkappa$	50M	1.116	0.588	0.164	$\varkappa$
	100A		1.51	1.97	1.04	0.541	100M	1.418	1.317	0.539	1.046
	200A		1.39	2.02	1.39	1.42	200M	1.761	1.617	1.070	1.054
	300A		0.344	2.03	3.16	1.00	300M	$\varkappa$	1.932	1.675	1.915
60°	50A		1.634	1.169	$\varkappa$	2.290	50M	1.138	0.703	0.973	0.259
	100A		2.102	1.452	0.870	0.537	100M	1.516	1.328	1.146	0.282
	200A		1.163	2.239	1.083	1.405	200M	0.922	1.280	1.370	1.830
	300A		0.734	2.290	2.371	0.919	300M	0.952	1.264	1.607	1.437
90°	50A		0.0957	2.325	2.071	3.641	50M	1.351	0.713	0.758	$\varkappa$
	100A		1.309	2.218	0.573	1.573	100M	1.977	0.891	0.836	0.473
	200A		0.962	2.033	0.892	1.564	200M	0.597	0.689	1.553	1.425
	300A		1.556	1.688	2.066	1.020	300M	0.993	1.054	1.058	1.593

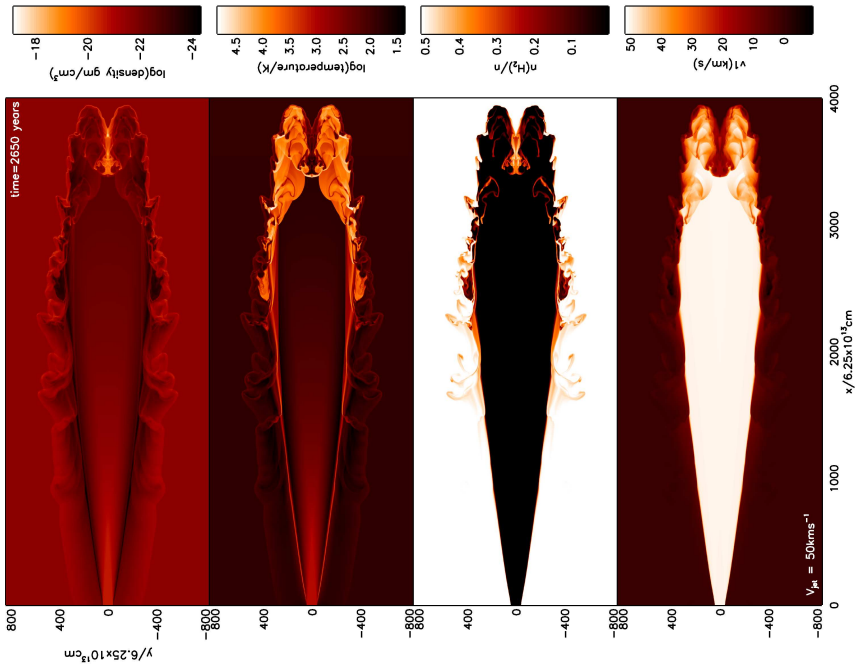

Figure 3.6: Cross-sectional distributions of physical parameters generated by an atomic jet of speed 50 km s^{-1} propagating into a molecular medium (AJMA). As labelled, the parameters shown are the mass density (gm cm^{-3}), temperature, molecular fraction and axial speed from the upper to lower panels.

the maximum $|V_{rad}|$ extent. However, this does not imply that the mass spectrum becomes shallower. As shown in Figure 3.7, the opposite is often the case within intervals B and C. This is probably due to the more aerodynamic shapes of the higher speed flows which lead to proportionally less of the ambient medium being accelerated to high speeds. However, a moderately high γ value is not an indication of high speed since various exceptions are recorded in Table 3.2.

Furthermore, the higher the viewing angle, the higher the maximum radial velocity. For example, the maximum point of M100 at 15° is 28 km s^{-1} while at 90° it is 100 km s^{-1} as would be expected from the jet radial component $v_{jet} \sin \alpha$. We might thus expect the slope to become shallower. However, inspection of the Table reveals that it is true for 200A in velocity field C and 300A in velocity field A and C at 15° viewing angle, but not generally.

A further trend is that mass spectra of the atomic runs possess a convex shape

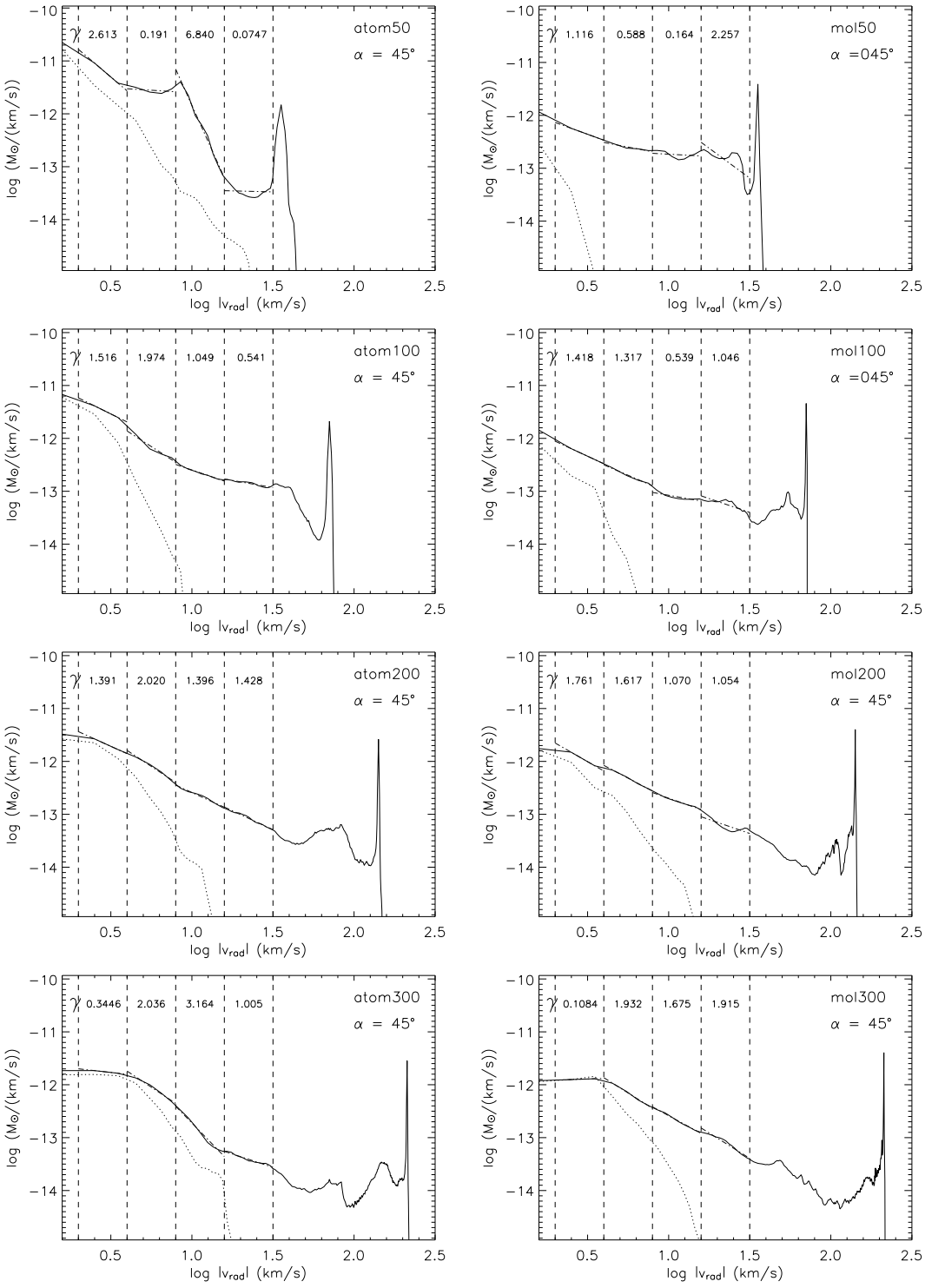

Figure 3.7: Mass spectra of the eight runs at a viewing angle of 45°. Both the redshifted and blueshifted emission are displayed, the redshifted material being represented the dotted line. The vertical dashed lines mark the divisions of the velocity intervals mentioned in Table 3.2. A dot-dashed line is fitted to the mass-velocity spectrum within each velocity interval and the value of the slope of each line is printed near the top of each plot.

(steepening towards higher radial speeds) whereas the molecular runs give a slight concave distortion within interval B. This may be related to the results of Rosen & Smith (2004a) who noted that for some of their simulations the power-law may be better fitted with an exponential (1/e) curve.

The most pronounced shape is associated with run 50A which has a 'speed hump' at the true (deprojected) velocity of 12.6 $\mathrm{km\,s^{-1}}$. At the 45° viewing angle in Figure 3.7 it produces a double peaked mass spectrum. The most likely cause of this intermediate velocity spike is the extremely wide extended 'working surface' created by the 50A jet as seen in Figure 3.1a. In fact, all the atomic runs possess a larger working surface than the molecular runs and this could be responsible for the slight convex shapes.

A detailed study of all the mass spectra demonstrates that the atomic outflows tend to produce larger values of γ than molecular outflows. This is particularly strong for the low speed runs (Figure 3.8, left) while the mass spectra for high speed runs roughly converge (see Figure 3.8, right). The mean value of all the slopes in velocity interval B of the molecular runs is 1.2 and for the atomic runs is 1.99. Repeating for velocity interval C gives 1.18 for the molecular runs and 2.12 for the atomic.

Mass spectra for runs MJAA and AJMA are displayed in Figure 3.9. They indicate that it is the ambient medium which mainly determines the value of γ. Overplotting MJAA and AJMA also clearly shows that AJMA possesses a greater amount of overall mass in motion. The expanded jet and the blunter leading edge in the AJMA run leads to a considerably larger volume of accelerated gas.

To further compliment the analysis we created two additional mass-velocity plots of the AJMA and AJMA50 runs (Figure 3.10). Here, we display the molecular mass rather than the total mass. As the jet beam is atomic, its contribution is reduced by a factor of 10^5. Furthermore, material impacting the leading bow shock is also dissociated. This effectively leaves only ambient material entrained through the wings of the advancing bow shock. In both cases shown, it leads to a significantly steeper molecular mass-velocity slope. A γ-value of ~ 4 is reached in the $16-32$ $\mathrm{km\,s^{-1}}$ interval. Figure 3.10

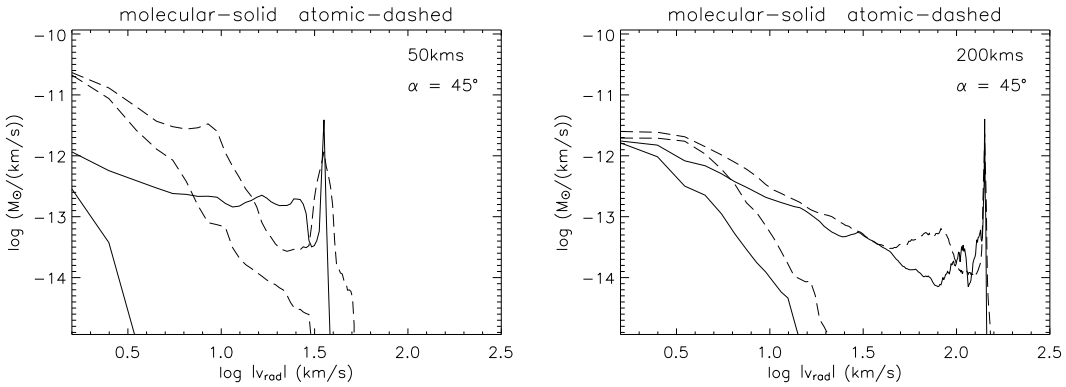

Figure 3.8: Mass spectra at 45^o viewing angle out of the sky plane depicting the molecular run with a heavy solid line and the atomic run with a heavy dashed line combined on the same plot for direct comparison purposes. **Left panel:** 50km s^{-1} case. **Right panel:** 200km s^{-1} case. The lighter solid and dashed lines represent redshifted material.

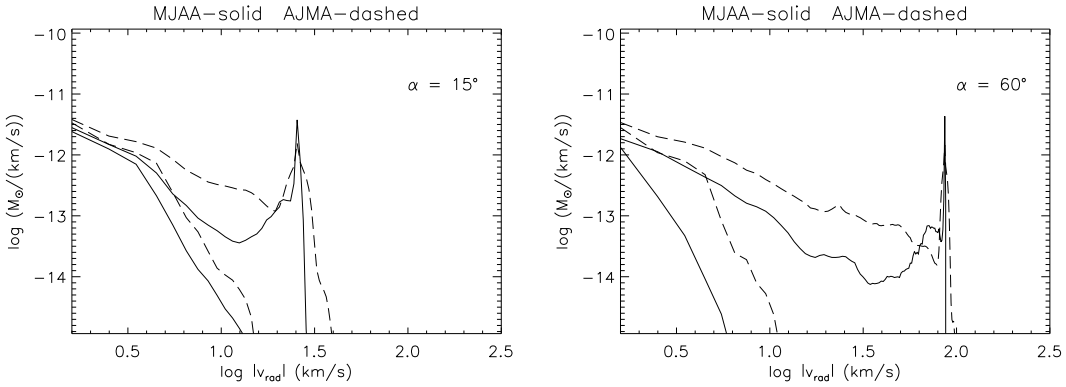

Figure 3.9: Superimposed mass spectra of the MJAA (solid line) and AJMA (dashed line) runs at the indicated orientations of the jet axis out of the sky plane. The lighter solid and dashed lines represent redshifted material.

also shows that the γ of the molecular mass is slightly larger than the γ of the total mass. A similar result was found in simulations by Downes & Cabrit (2003) and later by Rosen & Smith (2004a).

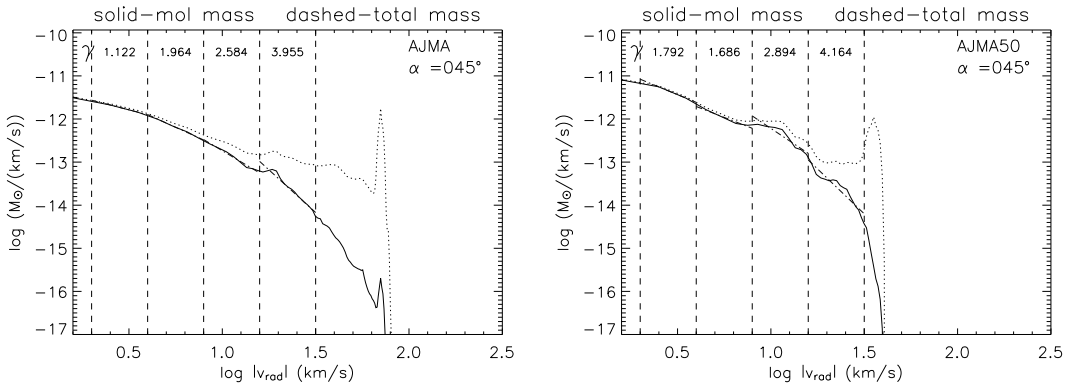

Figure 3.10: Molecular mass spectra at a 45° viewing angle out of the sky plane for the two AJMA runs. The dotted line shows the original total mass result and the solid line signifies the molecular mass-velocity spectrum.

3.3 Analysis and Discussion

3.3.1 Collimation

The most significant result is that molecular jets into molecular media generate highly collimated outflows at all jet speeds. This is due to a combination of two factors. Firstly, the fact that the molecular jets have a lower sound speed, and therefore a higher Mach number than their atomic counterparts, implies that molecular jets display little transverse expansion. The Mach number of 100A is only 30 whereas 100M is 140 (see Table 3.1). Table 3.1 also highlights that a fundamental difference between the atomic and molecular runs is the temperature of the jet and the ambient medium. The choice of temperature would change the Mach number and hence the cavity shape. Secondly, the molecular cooling through the leading edge and in the cavity reduces the extent of the cavity which remains inflated by a small fraction of warm atomic gas, corresponding to the dissociated fraction from the leading edge.

In the atomic cases, as the speed is raised the outflow structure becomes steadily more collimated. This is due to the differing grid crossing times coupled with the natural lateral expansion of the jet at the sound speed, c_s. We would expect the longer the crossing time, the greater the lateral expansion. In 50A the crossing time is over 2,850

years and the expansion is very noticeable compared to the 300A case which crosses the grid in a mere 330 years. Lateral expansion times follow the Mach expansion rule of $1/\mathrm{M}_{jet}$. A visual estimation shows that at 3,000 zones in the axial direction, the 50A jet has expanded 175 zones in the y-direction. This ratio is 17.1 which agrees with the Mach number from Table 3.1 of 15.21.

The molecular cooling jets do not exhibit a large lateral expansion despite similar crossing times. Although the 50M 2,000 year crossing time is faster than 50A, the cavity width retains fairly uniform collimation and is similar to that of the 300M jet. A similar calculation shows a 55 zone expansion after 3,000 zones which suggests a Mach number of 55. The actual Mach number is in fact 70.

The runs with high molecular content are seen to reach greater densities than the atomic runs. The molecules permit the compressed gas to cool thus decreasing the pressure and so increasing the inward pressure gradient, causing the material to collapse. Our molecular cooling routines would allow the gas to cool as low as 1 K but the dust has a fixed temperature, set to 20 K, which quite effectively heats gas (by collisions) falling far below that temperature. On the other hand, cooling in the atomic runs is only significant above 200 K and is most effective for temperatures above 10,000 K. It should be noted that the simulations in this thesis are of perfectly collimated jets with a zero degree initial opening angle. If we were to take a non-zero opening angle in the form of a shear or a spray angle it would lead to the creation of a complete range of cavity shapes independent of the initial Mach number and depending only on the initial opening angle.

3.3.2 Refocusing

An oblique internal shock is evident in the density plot of 100A which leads to the jet recollimation close to the front. Recollimation shoulders are evident to some degree in all 8 standard runs. These are small 'kinks' along the interface of the jet beam with

the shocked ambient medium which hint at the presence of internal shocks within the jet cavity. In the molecular runs, the shoulders lead to a tight focusing of the jet beam towards the axis while the ambient medium is deflected away from the axis by the oblique wings of a bow shock.

3.3.3 Molecular fraction

In the molecular cases, as the speed is raised, an increasing fraction of molecules are destroyed. In 50M there is very little molecular destruction. The greatest dissociation occurs in a very small region at the head of the jet where it is most likely being compressed against the axis. But even at this point, the molecular fraction only falls to 0.38 (from 0.5).

The cavity of 100M is also mostly molecular, mainly between 0.2 to 0.5. At a region around 3,000 zones in the axial direction some ambient material appears to have just been entrained by a large vortex.

A transition occurs between 100 and 200 $\mathrm{km\,s^{-1}}$ as the 200M cavity is almost entirely atomic but with some hints of entrainment. An interesting feature, also at 3,000 zones in the axial direction, is where ambient molecular material is being folded in and is now being dispersed.

The atomic runs show the molecular fraction changing in a way that appears similar to the molecular runs in that the molecular fraction decreases with velocity. However, the scaling of the atomic runs is in fact five orders of magnitude smaller. It is still interesting to note that such low fractions of molecular material also get destroyed. Note that at 200M and 300M there is still no significant reformation of molecules given the density and time scale (reformation requires roughly 10^{17}/n seconds).

3.4 Conclusions

We have explored how outflow structure depends on the jet speed, building on previous works which simulated protostellar outflows generated by 100 $\mathrm{km\,s^{-1}}$ molecular jets. We have assumed that the jet is initially highly collimated without precession in direction, pulsation or imposed spray angle. Each of these dynamical effects leads to distinct predictions.

We find that molecular jets into molecular media tend to produce highly collimated outflows because of their high Mach numbers. The transverse expansion of the jet at the sound speed depends on the initial jet temperature. The enveloping cavity is mainly filled with cool molecular gas for jet speeds at or under 100 $\mathrm{km\,s^{-1}}$ but is otherwise occupied by atomic gas.

The collimation is sensitive to the jet speed when atomic jets are launched into atomic media. The warm ballistic jets explored here are free to expand laterally which leads to wide cavities at low jet Mach numbers.

In all the molecular cases, the leading bow shock is acute with oblique shocks deflecting jet material towards the axis while external shocks deflect the ambient gas off the axis. The result is that the high pressure cavity gas remains adjacent to the jet, producing further oblique shocks which focus the jet gas towards the axis well before the leading edge. Extremely high rises in pressure occur at the working surfaces of high Mach number jets. In the molecular jets, the high pressure is only maintained within shock layers. The layers are maintained by ram pressure as the jet ploughs into ambient material. The aerodynamic shape results in two shock layers: a leading bow shock layer and a trailing highly oblique shock that provides jet focussing towards the axis.

On the other hand, in the atomic cases a transverse Mach disc is formed to terminate the low-speed jets. At speeds above 100 $\mathrm{km\,s^{-1}}$, the shock structure is more complex with jet deflection away from the axis.

This analysis suggests that we could tell whether a jet is atomic or molecular from its collimation only if the velocity is fairly low, < 100 km s^{-1}. High velocity (~ 300km s^{-1}) molecular jets could be confused with high velocity atomic jets as the molecules get destroyed in the molecular jet and the atomic jets high speed effectively maintains the collimation.

For all the simulations presented here we find similar (total) mass spectra properties for the 100 km s^{-1} case, i.e. quite shallow distributions. Therefore, higher jet speeds do not help to fully interpret observational statistics by producing steep mass spectra. In general, mass spectra trends with jet velocity or orientation are very weak. At high speeds there is little difference between atomic and molecular mass spectra. At low speeds, they are distinguishable with atomic jets producing significantly steeper mass spectra. However, atomic mass spectra are not directly observable with atomic line emission dominated by narrow ranges of physical conditions.

Molecular mass spectra may be directly related to the observed flux-velocity CO profiles such as those shown in Figures 2.22 and 2.23. Very rarely, however, has a prominent spike in CO profiles been observed which would be the signature of a molecular jet (Smith et al., 1997). Therefore, we presented here two examples of molecular outflows driven by atomic jets, finding not only that the jet velocity spike disappears but that the molecular mass spectrum steepens significantly above ~ 16 km s^{-1}.

Given these results, we conclude that other factors are required to provide the observed range of outflow properties. The present results provide the background for the next study which will examine the effect of density gradients and discontinuities in the ambient medium.

Chapter 4

Environmental Influence on the Propagation of Protostellar Jets

Bipolar outflows are associated with the early stages of the formation of stars with strong evidence for a direct connection to the inflow process through accretion disks (Calvet, 2004). Many bipolar outflows have been studied since their first discovery a quarter of a century ago as traced in rotational emission lines of carbon monoxide (Snell et al., 1980; Bally & Lada, 1983). Currently, there is an observational bias towards large established flows but new technology at millimetre and near-infrared wavelengths is revealing a wealth of smaller and younger outflows, such as in the DR21/W75 region (Davis et al., 2007). Small regions are also often observed in the optical as Herbig-Haro (HH) objects which are created where strong shocks form within the outflow, or at the leading edge where the outflow impacts against the surrounding medium (e.g. Bally et al., 2006).

A protostellar outflow usually takes a bipolar configuration with molecular gas receding from both sides of an obscured central object. Outflows are capable of maintaining high collimation over distances exceeding parsecs although quite uncollimated distributions are often found (Richer et al., 2000). Total outflow masses above 100 $M_{\odot}$ are

possible (e.g. Garay et al., 2007), implying that the material does not originate from the driving source but from the surrounding cloud. To drive such an outflow requires a source of considerable sustained momentum output.

There are currently three distinct theories which attempt to explain how such large amounts of material are set in motion. One involves a wide angle wind emanating from the accretion disk which sweeps up the ambient medium into a shell and is itself deflected in a momentum conserving fashion (e.g. Shu et al., 1991; Lee et al., 2001; Shang et al., 2006). The second scenario is the gradual entrainment of ambient material through a turbulent viscous mixing layer set up by Kelvin-Helmholtz instabilities as a jet streams past (Canto & Raga, 1991). The third scenario is called the 'prompt entrainment' model. Here, a large bow shock is driven by a supersonic jet which is launched and collimated by magnetic fields (e.g. Raga & Cabrit, 1993; Smith et al., 1997; Rosen et al., 1999).

All the scenarios can explain some observed features but none is completely satisfactory. One of the main problems associated with directed jet models is that they cannot produce the observed outflow widths. In the directed jet model, strong molecular cooling and a high Mach number limits the transverse expansion and the width is usually determined by the leading bow shock. In a uniform medium, if the axial propagation increases linearly with time, the transverse expansion increases only as $t^{1/3}$ (Lee et al., 2002). Problems with the wide-angle wind models are that they cannot create bow-shock like features or the high degree of collimation of some observed flows (Lee et al., 2002). Additionally, the wind scenario cannot explain the fact that the highest radial velocities are found furthest from the driving source (Masson & Chernin, 1993).

It can be argued that both the jet and wind mechanisms may play cooperative roles (Shang et al., 2006). Perhaps over time as the accretion rate falls, the jet may weaken and the wind becomes the dominant driving mechanism. Alternatively, a wide-angle precession in the jet direction will also simulate most features of a wide-angle wind (Rosen & Smith, 2004a).

We examine here the issues associated with the jet scenario. It is assumed that momentum is channeled from near the young star system via a jet into the surrounding ambient medium. The efficiency of momentum transfer has been a topic of recent debate and suggests that it may be too low to supply the bipolar outflows (Su et al., 2004). Cunningham et al. (2006) performed simulations investigating fossil cavities – outflows where the driving source has recently switched off. One of their findings is a scaling law which could be used to predict the momentum input into observed cavities from their sizes and velocities. As in the previous chapter, we calculate the physical structure of the flow and the momentum transferred as measured by the distribution of CO mass, $m(CO)$, with radial velocity, v_r. The CO mass spectrum is quantified by fitting the equivalent power-law sections of the form $m(CO) \propto v_r^{-\gamma}$ even when the power law is not appropriate.

It has been found from observations that numerous outflows appear to follow a so-called 'Hubble Law', meaning that their velocity increases linearly with distance from the driving source ($v \propto d$). This has also been noted in jet simulations of Smith et al. (1997) and Downes & Ray (1999). The latter noted that the Hubble Law effect is associated with the bow shock and is a global phenomenon only if the bow shock acts as the interface with the ambient medium for the entire flow. In the wind model, the higher velocity further from the source could also be caused by an ambient medium whose density decreases in a power-law profile of the form $1/r^2$ (Shu et al., 1991).

It becomes clear that outflows contain as much information about the medium they disturb as the object which drives them. Hence, we need to develop means to decipher their signatures before we can gain insight into the deeply embedded young stellar object (YSO) at their heart. We wish to distinguish the launch-induced properties from the environment-induced properties. Here, we will investigate numerically the influence the environment has on the outflow. This follows up on previous works which have explored the influence of the driving source in terms of jet precession, pulsation, shear, speed and rotation, all into a uniform ambient medium (Smith & Rosen, 2005a;

Moraghan et al., 2006; Smith & Rosen, 2007).

There are two issues that require our attention. Firstly, do we observe HH objects and molecular shocks because they are the present points of impact within and at the end of an impulsive jet? Or, do we only observe the locations where the outflow temporarily interacts with dense structures in the ambient medium? To probe this, we present three simulations containing clumps or filaments in the ambient medium for the jet to collide with. The clumps are represented here as thick sheets, aligned transverse to the jet axis (as the assumed cylindrical symmetry approximation allows).

Secondly, outflows from the youngest forming stars must still excavate through dense protostellar envelopes. These envelopes are believed to possess power-law density profiles. We ask here if there are specific signatures which can be related to the nature of the envelope. To probe this, we run simulations over a large power-law parameter space. We present four simulations to highlight the trends of changing the various parameters.

Three dimensional simulations of atomic jets into ambient media with power-law density profiles as well as large clumps have been presented by de Gouveia dal Pino & Birkinshaw (1996) and de Gouveia Dal Pino (1999). Due to the high jet sound speed, the jet is poorly collimated. They noted that the expanding jet may oscillate in velocity. They also remarked that a jet interacting with clumps may inject a considerable amount of shocked jet material sideways into the ambient medium, providing a means to transfer momentum through turbulent mixing with the ambient medium.

4.1 Method

Expanding on the work of Chapter 3, we have modified the ZEUS-3D code to incorporate an inhomogeneous ambient medium whose density falls off as a power-law with distance from the source (the left hand side of the grid). Comparable simulations have previously been performed by de Gouveia dal Pino & Birkinshaw (1996) and Carvalho

& O'Dea (2002) but only for radiatively cooled atomic flows and adiabatic extragalactic jets, respectively. Along similar lines, O'Sullivan & Lery (2002) simulated an inhomogeneous ambient medium by inserting a step along the grid where the ambient medium changes from a molecular core composition to one of an interstellar medium.

We also add sheets of dense molecular gas perpendicular to the jet axis. Many simulations of turbulence in star-forming regions (including those with molecular cooling and chemistry (e.g. Pavlovski et al., 2004)) show that molecular clouds would be filled with filaments and sheets of denser material. Our modified code somewhat approximates such a system by allowing the simple inclusion of 'clumps' or slabs within the ambient medium.

Here, the entire jet and cocoon collides head on and must tunnel through the sheets. This thick shell approach may emulate head on collisions with large clumps, the crossing through of other outflows and their bow shocks, or, assuming outburst episodes, may represent bow shocks from a previous ejection event from the same source or 'fossil cavities'.

Simulations performed by Rossi et al. (2000) followed a similar approach of a jet colliding head-on with a density enhancement in 2D axisymmetry. Their work differed by dealing with radiative extra galactic jets and the enhanced density slabs representing Giant Molecular Clouds (GMCs).

The sound speed in the ambient medium is sufficiently low (~ 0.7 km s^{-1}) so that little dispersal of the envelope or sheets occurs. Therefore, we do not include any external force to maintain either the envelope density or the shell density profile. Strictly speaking, however, the sheets would correspond to the temporary features expected in a turbulent medium. The longevity of the sheets was carefully tested by modeling the ambient medium alone for thousands of years to investigate if there was a drifting of the higher density material to the lower. It was found to be negligible for the grid crossing times of all our jets. This can also be verified on the figures presented here which display the density profile of the ambient medium at the times indicated.

We follow the same overall grid dimensions as Chapter 4, i.e., 2.5D axisymmetric simulations on a grid of 4,000×800 zones covering $(2.5\times10^{17}\mathrm{cm})\times(5\times10^{16}\mathrm{cm})$ in extent. The initial jet radius is $\mathrm{R}_j = 2.5\times10^{15}$cm, leading to 40 zones per jet radius, 100 jet radii in the axial direction and 20 jet radii in the radial direction. Again, magnetic fields have been omitted as we are only focusing on the effect of the ambient medium on the outflow.

For this study, we focus on one particular set of initial jet conditions: the 100 $\mathrm{km\,s^{-1}}$ atomic jet into a molecular ambient medium (the AJMA jet of Chapter 4). The jet is over-dense with respect to the ambient medium by a factor of $\eta = \rho_j/\rho_a = 10$. The molecular hydrogen abundance in the ambient medium is set to 0.5 (fully molecular) and in the jet beam the molecular fraction is reduced to 10^{-5} with the carbon and oxygen abundances remaining as 10^{-4}. This ensures that only the atomic radiative cooling approximation controls cooling in the jet.

By taking an atomic jet, we are able to explain bipolar outflows which possess high values of the mass-velocity power law index, γ (Moraghan et al., 2006). However, we thereby exclude the presence of high velocity CO along the main jet axis, as is sometimes observed (see Downes & Ray, 1999). Although molecule formation can occur in the encoded physics, the jet material remains atomic due to the low density. On the other hand, the lack of a detectable high velocity jet component in most mass-velocity observations may be attributed to the absence of molecules in the jet beam itself. However, it could also be explained if the molecular jet beam possesses velocity variations and, thus, the jet contribution is spread over the full velocity range (see Section 4.6). In reality, it is possible that the jet may heat and liberate CO from ices on dust or grain surfaces, where the CO had previously frozen to the surfaces at low temperatures below 20K, and densities of $\sim 10^4\,\mathrm{cm^{-3}}$ typical of starless cores (Carolan et al., 2008).

Table 4.1: Summary of the parameters of our setup.

property	Jet	Ambient
density, (gm cm^{-3})	2.342×10^{-21}	2.342×10^{-22}
sp. energy, (ergs cm^{-3})	2.278×10^{-10}	1.933×10^{-12}
n(H_2)/n	1.0×10^{-5}	0.5
sp. heat ratio, γ	1.66667	1.42857
temperature, (K)	1,000	100
Sound speed, (km s^{-1})	3.29	0.71
Mach number, M_{jet}	30.42	140.67

Our ambient medium density profile nearly follows the form of a King profile:

$$d\,(i) = \frac{d_a}{1 + \left(\frac{x(i)}{\Psi}\right)^{\chi}}, \tag{4.1}$$

where $d(i)$ and $x(i)$ are the density and position, respectively, along the x-direction (the jet axis) expressed in zones, d_a is the initial ambient medium density (see Table 4.1), Ψ is the size of a relatively uniform 'core' or plateau region at the beginning of the grid and χ is the power-law exponent. We found that the χ and Ψ parameters are intrinsically linked and must both be carefully controlled in order to obtain sensible profiles. Figure 4.1 displays the four profiles used in the envelope simulations presented here and Table 4.2 lists the parameter space covered.

Table 4.2: Summary of the parameters for the ambient medium density profiles. χ represents the power-law exponent and Ψ represents the size of the 'core' region defined by Equation 4.1.

Profile	χ	Ψ(cm)	Ψ(zones)
1	4.0	1.250×10^{17}	2,000
2	1.0	6.250×10^{16}	1,000
3	1.5	3.125×10^{16}	500
4	2.0	3.125×10^{16}	500

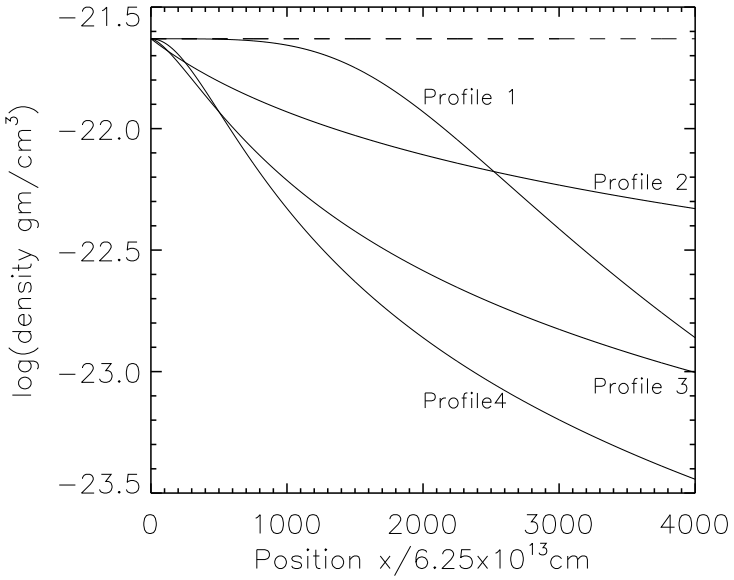

Figure 4.1: Plot showing the four ambient medium density profiles used in our protostellar core simulations superimposed for comparison purposes and labeled Profile 1 – 4, the parameters of which being displayed in Table 4.2.

4.2 Results: composite figures

The multifaceted visualisations of the main runs shown in Figures 4.2 to 4.8 present the following information.

- The first panel displays the total mass density in g cm^{-3} on a logarithmic scale with the corresponding scale bar to the right. The simulation 'age' is shown in years.
- The second panel displays the temperature in degrees Kelvin, again on a logarithmic scale with the scale bar displayed on the right. The figure is flipped by 180° to aid in visualising the entire outflow.
- The third panel shows the molecular fraction or, in other words, the ratio of hydrogen molecules to the total number of hydrogen nuclei (n(H_2)/n). It is on a linear scale from 0 (completely atomic) to 0.5 (fully molecular).
- The fourth panel displays the pressure in erg cm^{-3} on a logarithmic scale.

- The fifth and sixth panels display the axial (v1) and radial (v2) velocities, respectively, in km s^{-1}. Interestingly, negative v2 velocities can be seen signifying motion towards the jet axis. This shows turbulent mixing/entrainment along the cocoon.

- The seventh panel is a graph of the density profile of the undisturbed ambient medium (solid line) along the full axial extent of the grid (x-axis in the plots). The 'log(density)' axis label signifies mass density in g cm^{-3} on a logarithmic scale. The corresponding jet beam (dashed line) density profile is shown at a radial distance of 0 (y-axis in the plots). The χ and Ψ parameters for each core simulation are printed to help aid identification.

- The bottom detached panel is a plot of the γ values as a function of *time*. The line thickness represents the radial velocity intervals, ranging from the thickest line for the fastest ('16–32 km s^{-1}' and '8–16 km s^{-1}') intervals to the thinest line for the slowest ('4–8 km s^{-1}' and '2–4 km s^{-1}'). They are additionally colour coded in the electronic version against the final instantaneous mass spectrum display to the right. These plots were obtained with the aid of an additional modification to the ZEUS-3D code. This modification calculates and outputs the mass-velocity spectrum at intervals of one year during the simulation. Animations of the data thus allow us to precisely follow the evolution of the mass-velocity profile as the outflow propagates across the grid.

- The instantaneous end-of-run mass spectra are plotted in the bottom right panel. All the spectra are displayed for a 45° viewing angle out of the plane of the sky. The y-axis scale is in units of the logarithm of solar mass per kilometer per second, $\log(M_\odot/(km/s))$.

  The solid line shows the molecular mass in motion while the dotted shows the total grid mass in motion, both representing blueshifted material towards our line of sight. The vertical dashed lines divide the spectra into the four radial velocity regions: 'A', 16–32 km s^{-1}; 'B', 8–16 km s^{-1}; 'C', 4–8 km s^{-1} and 'D', 2–4 km s^{-1}.

The slope of the molecular mass spectra within the intervals is printed near the top of each plot. These values are additionally colour coded to the lines of the γ versus time plot. The sharp peaks in the total mass spectra represent the jet beam material at a radial velocity, $|V_{rad}|$, or $v_{jet} \sin \alpha$, whose log value is 1.85 for our 100 km s^{-1} jets.

High resolution electronic versions of the figures are available on the included optical disk.

The simulations were initially run at low resolution to explore a wide area of parameter space. Several resolutions were then employed to check that convergence in the results was occurring within the expectations for a turbulent flow. The surprisingly strong and rapid temporal variability in γ was noted. Selected runs were then re-run at high resolution to provide the figures displayed here as Figures 4.2 to 4.8.

Ambient density 'clump' simulations are shown in Figures 4.6, 4.7 and 4.8. They consist of various configurations of slabs or sheets within the ambient medium.

4.3 Propagation out of cores

4.3.1 Flow structure

The initial density profile of the ambient medium follows a sequence as shown in Figure 4.1. It is apparent that the sequence corresponds to a trend in the turbulent density structure from Figure 4.2 to Figure 4.5, as follows:

1. The jet flowing through the plateau core of Figure 4.2 generates a turbulent interface in the *inner region*. However, a smooth shell is produced around the leading bow which has exited the plateau.

2. The smooth shallow gradient taken in Figure 4.3 yields the opposite result. The expanding jet interacts stronger with the *outer regions*, and the turbulent interface is

Table 4.3: Comparison of the mass and momentum values of our runs at their end of grid configurations. In the eighth and tenth columns, 'momentum' is abbreviated to 'mom'. The values for the 'Uniform' run are taken from the AJMA simulation of Figure 3.5b in Chapter 3.

Run	Entire grid mass ($M_\odot$)	Total moving over 3 km/s ($M_\odot$)	H_2 mass over 3 km/s ($M_\odot$)	Total mass momentum ($M_\odot$km/s)	H_2 momentum ($M_\odot$km/s)	H_2 mass/ Total mass	H_2 mom/ Total mom	Injected mass/ Total moving mass	Uniform H_2 mom/ Run H_2 mom
Profile 1	1.31(-4)	1.04(-5)	1.88(-6)	4.85(-4)	1.37(-5)	0.182	0.028	0.704	0.37
Profile 2	9.99(-5)	1.02(-5)	1.17(-6)	4.87(-4)	8.78(-6)	0.115	0.018	0.712	0.23
Profile 3	5.59(-5)	7.99(-6)	6.11(-7)	4.36(-4)	3.94(-6)	0.076	0.009	0.822	0.11
Profile 4	4.82(-5)	7.55(-6)	4.99(-7)	4.35(-4)	3.40(-6)	0.066	0.008	0.870	0.09
Multiple Clump	7.22(-4)	3.11(-5)	1.96(-5)	6.35(-4)	1.78(-4)	0.63	0.28	0.33	4.75
Single Clump	4.01(-4)	1.86(-5)	8.49(-6)	5.26(-4)	7.26(-5)	0.46	0.14	0.43	1.94
Extended Clump	1.21(-3)	3.25(-5)	2.28(-5)	5.38(-4)	1.62(-4)	0.70	0.30	0.27	4.32
Uniform	2.39(-4)	1.51(-5)	5.08(-6)	5.32(-4)	3.75(-5)	0.34	0.07	0.53	1

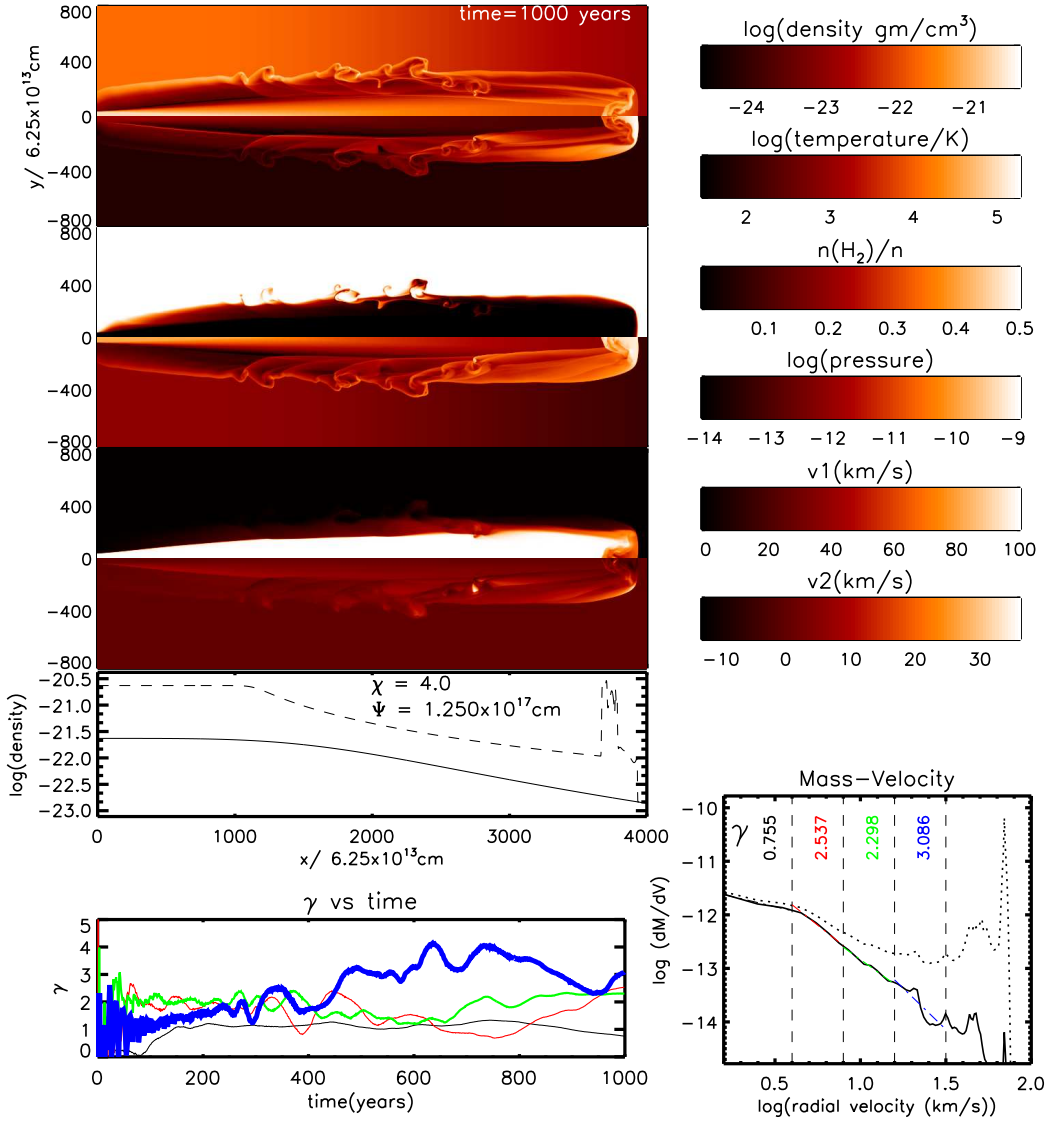

Figure 4.2: The outflow structure for the plateau density profile, Profile 1, simulation given in Table 4.2 and illustrated in Figure 4.1. See Section 4.2 for full figure explanation.

located in the leading half of the flow. The turbulence is portrayed in the velocity components as well as the density.

3. The structure of Figure 4.4 is generated by a moderate density gradient. The density shell contains only weak turbulence but does contain a large vortex.

4. The steep density profile of Figure 4.5 produces a very smooth interface. There is no sign of turbulence or large vortices.

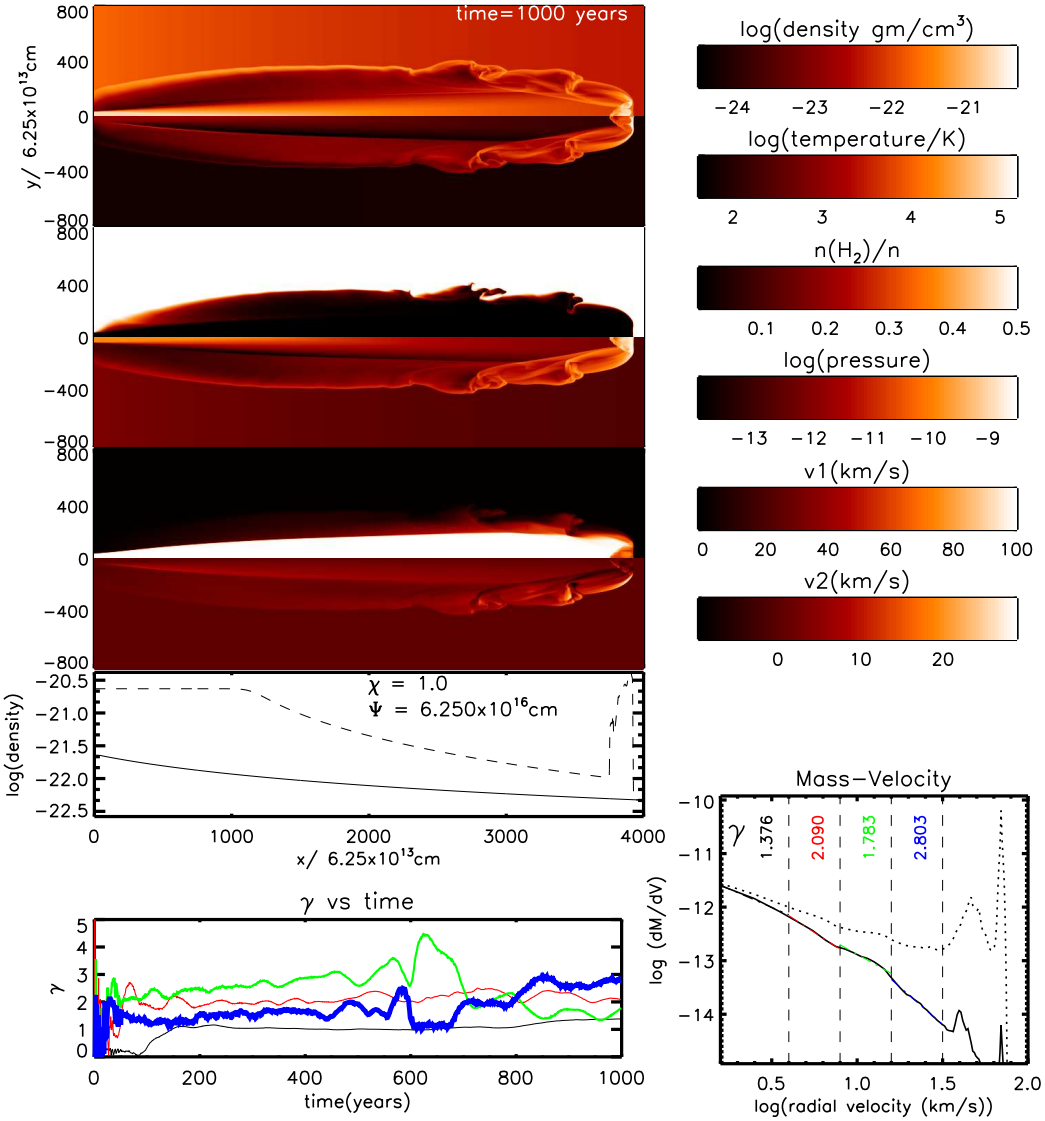

Figure 4.3: The outflow structure for the plateau density profile, Profile 2, simulation given in Table 4.2 and illustrated in Figure 4.1. See Section 4.2 for full figure explanation.

These effects are correlated with the density, temperature and pressure profiles. Turbulence is not created in Figure 4.5 corresponding to Profile 4 because a hot atomic cavity can expand laterally into the lower density surroundings. The rapidly falling ambient pressure and the wide cavity protects the jet from pressure feedback from the ambient gas. As a result the jet continues to propagate ballistically (see the conical

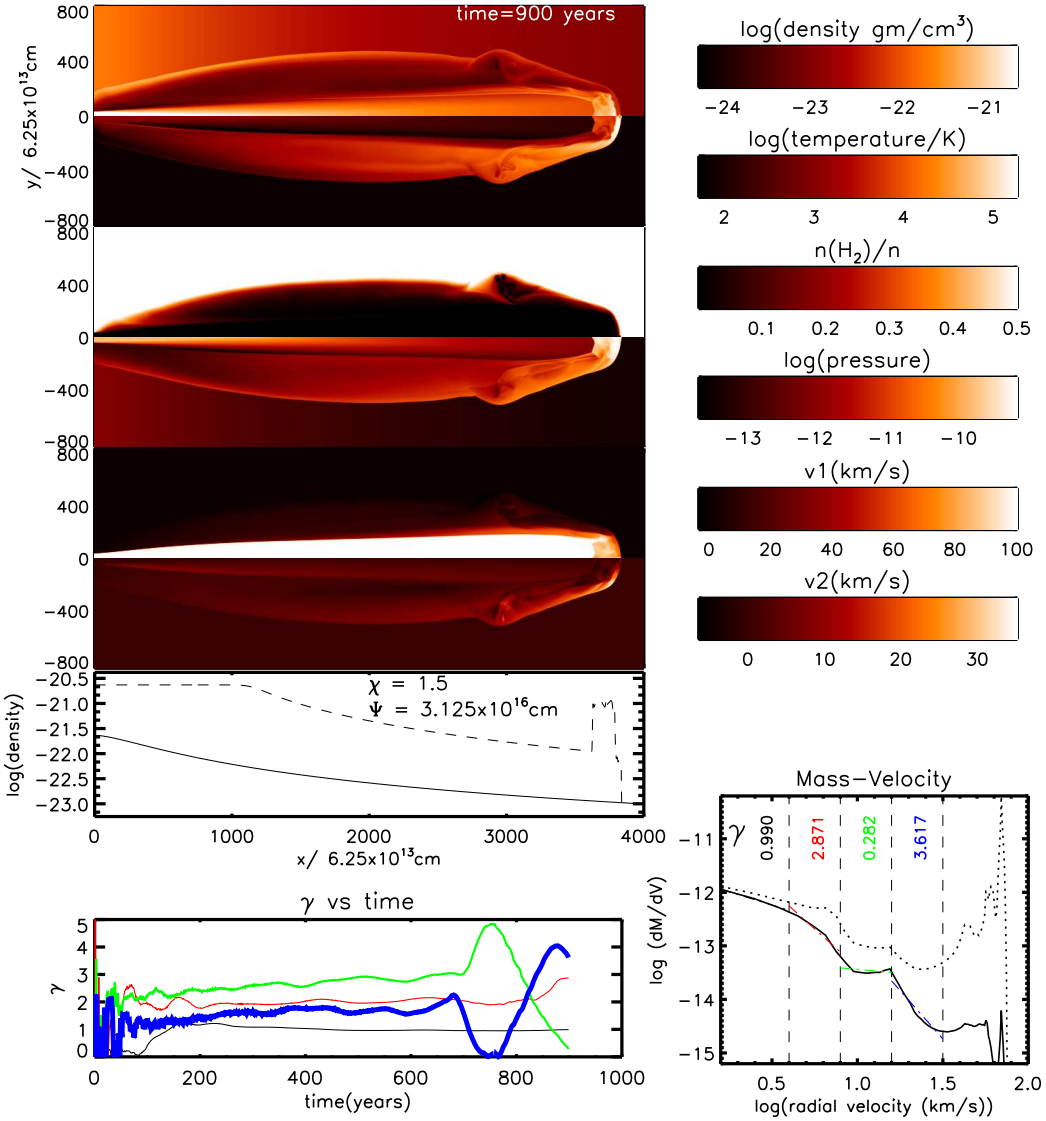

Figure 4.4: The outflow structure for the plateau density profile, Profile 3, simulation given in Table 4.2 and illustrated in Figure 4.1. See Section 4.2 for full figure explanation.

structure of the axial velocity, v1), expanding laterally at a small constant rate. The jet and ambient material flows into the cavity at speeds approaching 40 km s^{-1}. The cavity is filled with hot low-density atomic gas at around 10^5 K.

In contrast, with a shallow gradient, the ambient and jet pressures become comparable (Figure 4.3). The jet is slightly deflected towards the axis and the highest pressure of all four simulations occurs at the impact location or terminal shock. The cavity

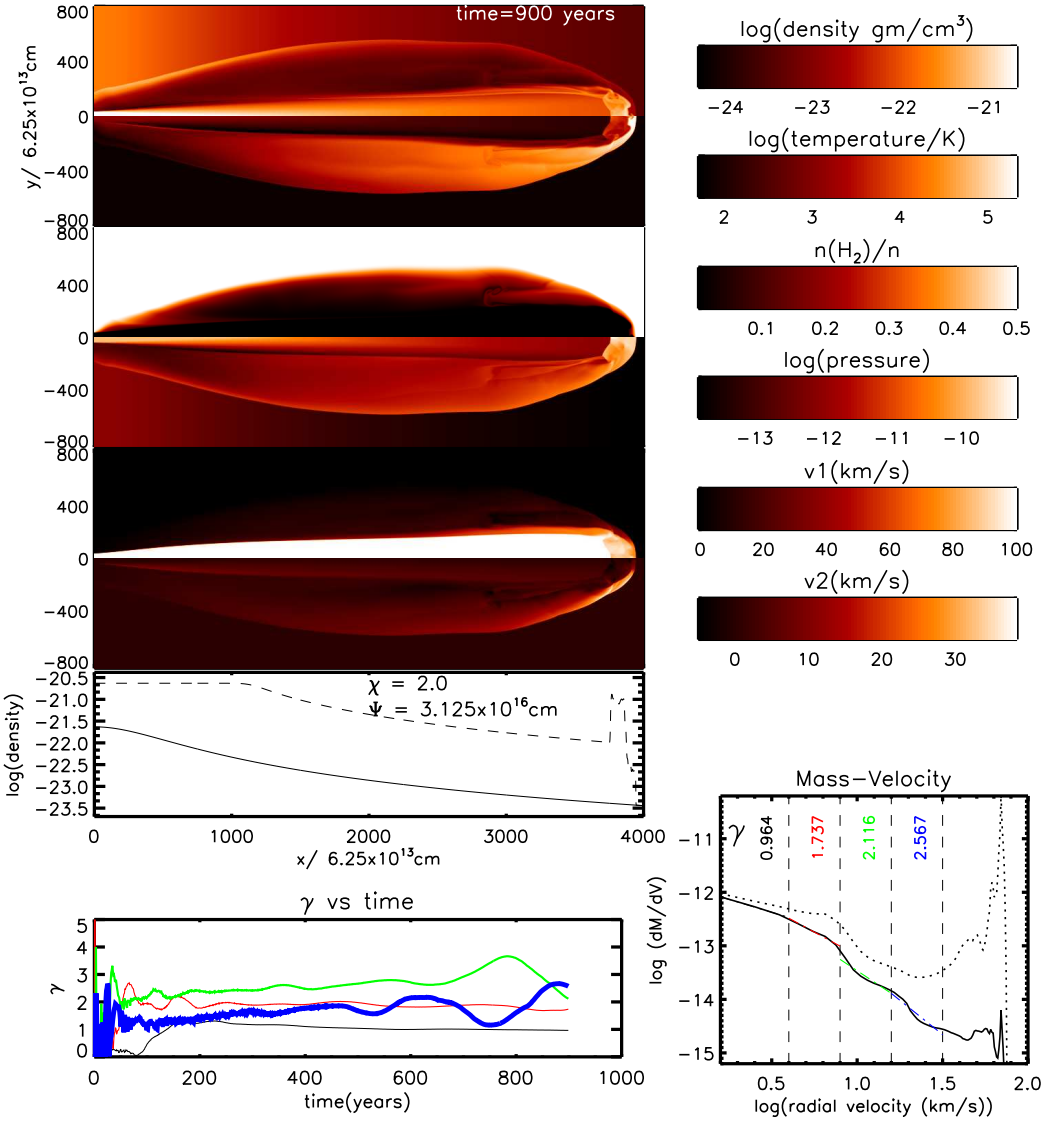

Figure 4.5: The outflow structure for the plateau density profile, Profile 4, simulation given in Table 4.2 and illustrated in Figure 4.1. See Section 4.2 for full figure explanation.

contains warm atomic gas at $\sim 10^4$ K.

Returning to the plateau core (Figure 4.2), the turbulence takes the form typical of a mixing layer brought on by the Kelvin-Helmholtz instability. This was also revealed in the simulation AJMA where a uniform environment was taken. This demonstrates that a turbulent cocoon is not only caused by a 'clumpy' ambient environment.

An intrinsic feature associated with all the jets presented here is that after propa-

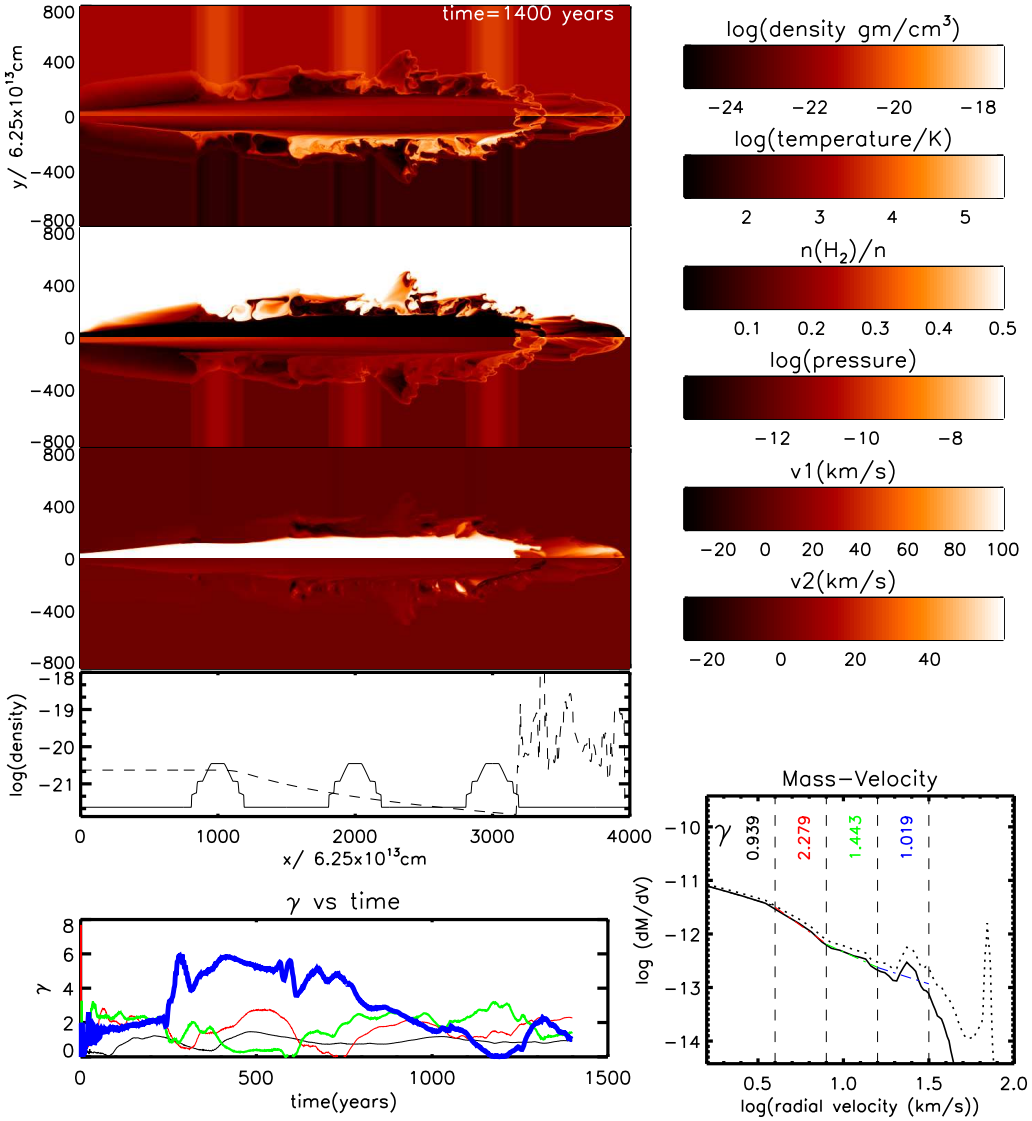

Figure 4.6: The outflow structure for the Multiple Clump discontinuity simulation. See Section 4.2 for full figure explanation.

gating about 1,000 zones, the jet density begins to fall (observe the dashed lines on the graphical profiles of the seventh panels). This is due to the propagation of a rarefaction wave from the jet beam surface to the central jet beam axis at the sound speed. As the jet beam is supersonic, this sound signal travels inward with a Mach angle of about 3°. The differing rates of the decreasing ambient density between the runs do not have a noticeable effect on the central jet expansion. It does however effect the expansion rate of the cocoon with Profile 3 and 4 having a smaller length to width ratio compared to

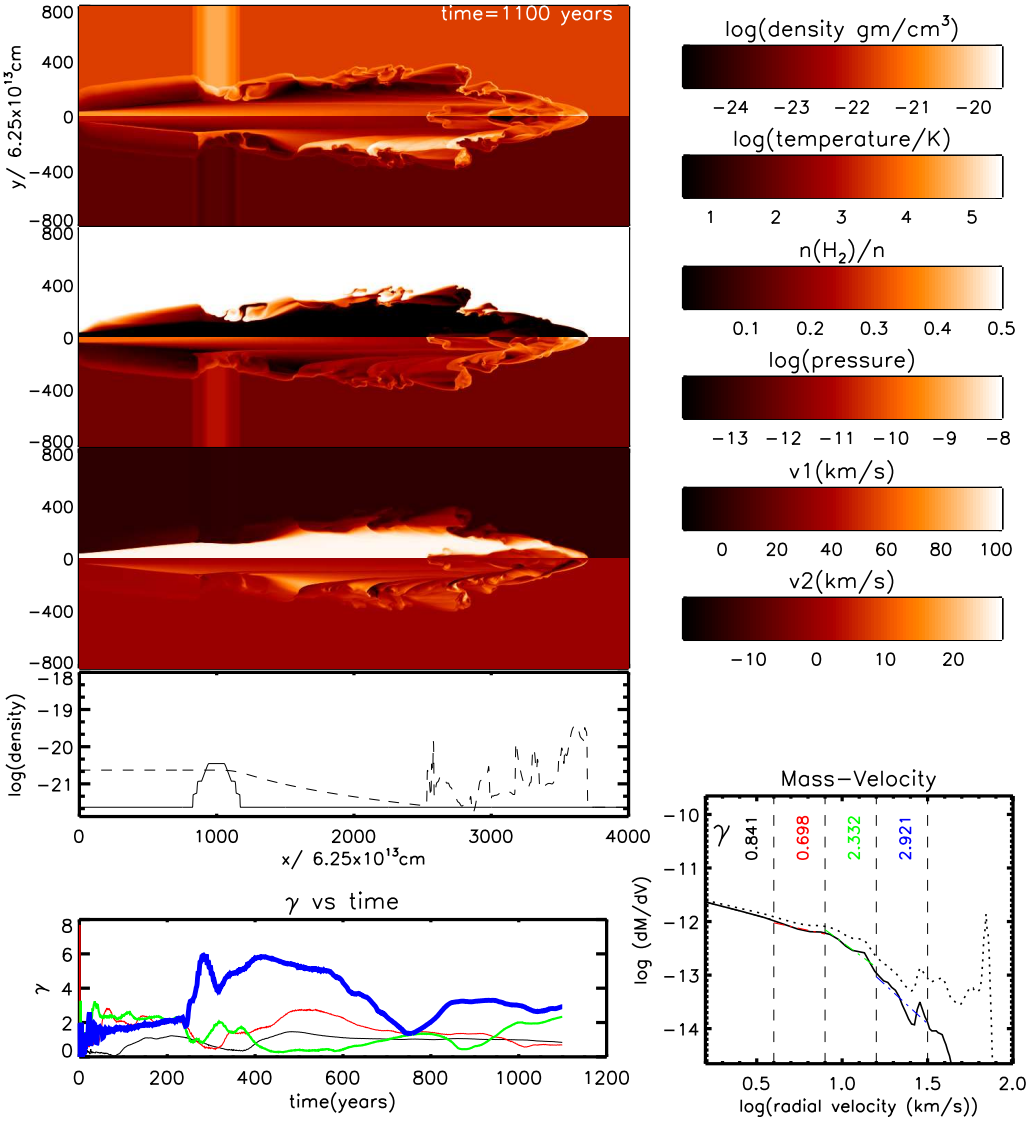

Figure 4.7: The outflow structure for the Single Clump discontinuity simulation. See Section 4.2 for full figure explanation.

Profiles 1 and 2.

The molecular fraction panels of Figures 4.2 and 4.3 show a clear division between shocked jet beam and shocked bow shock material. Entrainment is seen to occur in discrete clumps via fluid dynamic instabilities along the flanks (along with entrainment and strong dissociation around the front leading edge). In contrast, the broader bow shock wings of Figures 4.4 and 4.5, intercept and partially dissociate a higher fraction of the ambient molecular gas over wide areas. Thus, our steep profile run in Figure 4.5

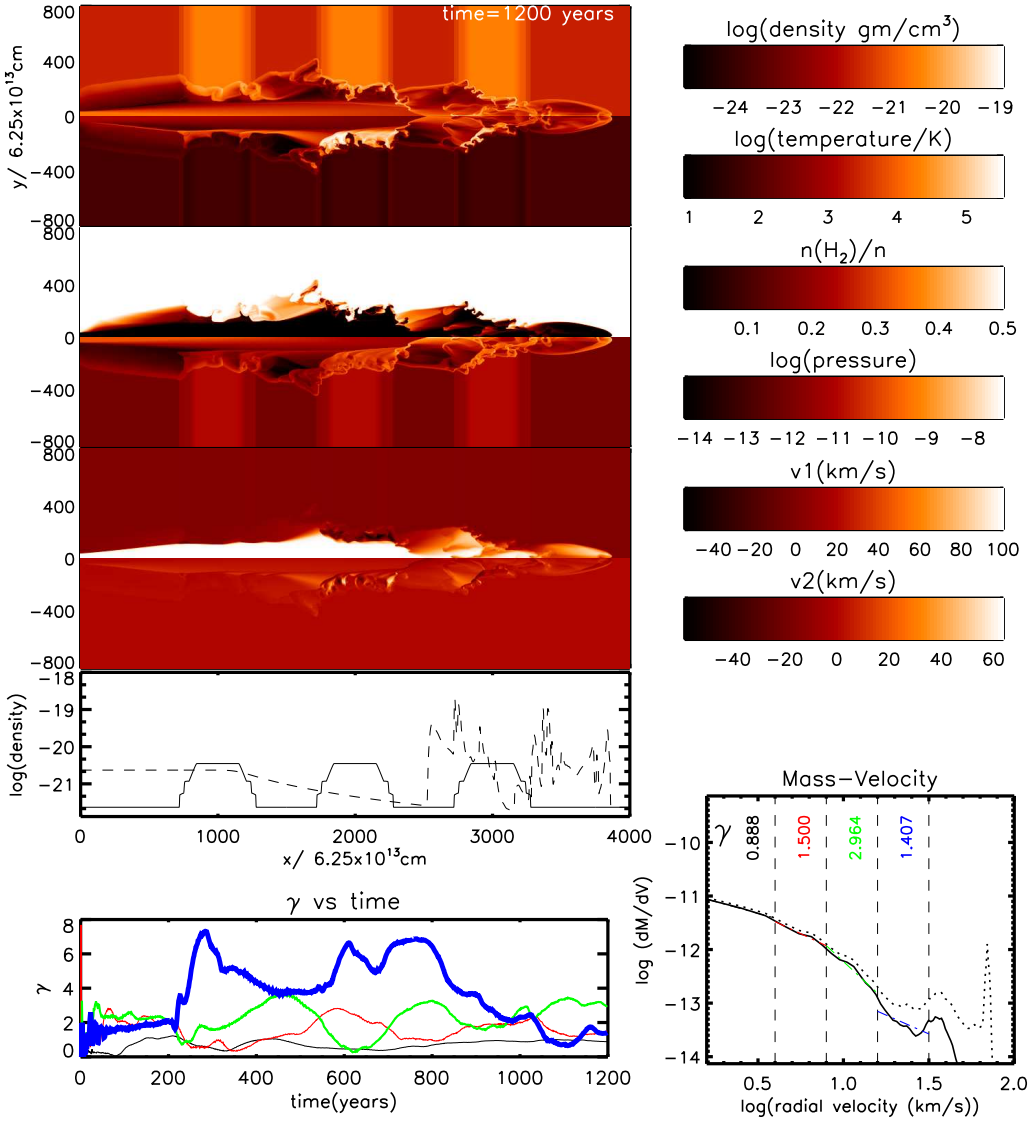

Figure 4.8: The outflow structure for the Extended Clump discontinuity simulation. See Section 4.2 for full figure explanation.

resembles the shape of the simple bow shock models of Raga & Cabrit (1993) suggesting pure bow shock entrainment. Finally, note that the radial extent of the shocked jet beam material in the cocoon remains roughly constant for each profile.

Are steeper profiles more efficient at setting mass in motion? Although the steeper profiles generate broader shocks that intercept a large volume of molecular gas, Table 4.3 demonstrates that both the total moving mass and moving molecular mass actually decreases for steeper profiles. Hence, less mass is being swept up despite the cavity

volume appearing larger. Similarly, the same is true for the momentum values. It is clearly a trade off between cocoon width and the ambient medium density. Lower ambient densities lead to a wider flow but with less mass to entrain. Higher densities lead to a more collimated outflow where the mass entrainment is mainly through the terminal bow shock.

Corrected for outflow age and moving from Profile 1 to 4 we find:

- The entire grid mass drops by about 2.5 orders of magnitude yet the total moving mass fraction only decreases by about 20%.

- The total mass momentum decreases by 45% yet the molecular momentum decreases by a much larger amount, 120%.

This suggests that the steeper the profile, the less efficient the sweeping up of molecular ambient material becomes. The cavity increasingly consists of processed atomic jet beam material. Less molecular mass is entrained despite the larger inflated bow shocks.

The fraction of injected-mass/total-moving-mass increases as the profiles become steeper. In all the runs, jet beam material is injected onto the grid at a steady rate of 7.295×10^{-9}M$_\odot$/year, but less grid moving mass leads to larger fractions. With these smoothly varying profiles, however, the fraction remains in a small range between 0.7–0.8.

Note that the 'moving mass' is defined with a lower limit of 3 km s^{-1} since it would be difficult to distinguish between general cloud turbulent motion and outflow motions at lower velocities.

4.3.2 Mass spectra analysis

The time evolution of the mass spectra as well as the final mass spectra are displayed on the figures for each run. The chosen angle to our line of sight is 45°. The major result is the strong and rapid variability of the characterising γ indices for radial speeds exceeding $\sim$ 4 km s^{-1}. However, for low radial speeds (thin black line on evolution plots), the indices remain quite constant and relatively flat (close to unity). This implies that most of the mass set in motion possesses speeds of a few km s^{-1}. Most of the momentum is contained in the gas moving at speeds exceeding $\sim$ 4 km s^{-1}.

The time scale of the variation corresponds to that associated with large scale changes to the leading bow shock. The jet dynamical timescale, r_{jet}/v_{jet} is $\sim$ 8 years while the bow dynamical timescale is taken as $r_{bow}/v2_{max}$ where we take the bow size as $r_{bow} = 10^{16}$ cm and the maximum transverse speed $v2_{max} = 30$ km s^{-1} to give $\sim$ 100 years.

All the runs possess a small CO mass–velocity peak lying between a radial velocity of 45–55 km s^{-1}. This is due to entrained ambient material in the working surface behind the bow shock. At certain times the working surface material gets expelled into the cavity as a vortex. This phenomenon can be seen to have just occurred in Figure 4.4 where the shedded vortex has slowed to a radial velocity of 16 km s^{-1}. Its strength in the mass-velocity plot dampens as it propagates to slower v_{rad} before finally being absorbed within the low velocity mass reservoir. The vortex shedding events also appear on the γ evolution plots in the intervals 'C' and 'D' which display corresponding peaks and troughs at simultaneous evolution times.

The γ values for material with radial speeds 16–32 km s^{-1} generally display the strongest variability, γ reaching values in excess of 4 for short periods. The variability is correlated with the turbulence. In the plateau core, strong variability is present after just a few hundred years. With the shallow gradient (Figure 4.3), the variations start after 500 years, coinciding with the development of the vortices. Note that at

first, this generates a quite flat index of $\gamma \sim 1$ at 600–700 years, caused by the initial development of a large vortex. Once the vortex is transferred to the cavity interface where turbulence then develops, the spectrum then steepens. Note that this behaviour appears to be present but less dramatic in the following runs with steeper density profiles. While there is less turbulence in these runs, there is a mild interaction with the jet.

The mass spectra referred to above are the CO mass spectra, related to observations. Note the *total mass* spectra (dotted line) are much flatter. Not only does the jet contribute to this (see the spike on the dotted lines on the right-hand panels) but the atomic flow into the cavity generates a very flat profile. Hence, to obtain a steep profile we require an atomic jet or a means to dissociate the molecules before they enter the cavity.

Furthermore, there is no obvious general trend in the simulations for steepening or flattening with time – depending on the precise conditions, and the particular time of observation, almost any mass spectrum can be observed. The average overall γ value can be seen to generally slowly increase over time beneath the fluctuations of the fastest two γ intervals ('C' and 'D') in the intermediate and steep profiles (See Figures 4.4 and 4.5). The slower two γ intervals, ('A' and 'B') tend to remain constant but the more turbulent the cocoon becomes (i.e. in a less steep density gradient run), the fluctuations translate back to the slower intervals and lead to a general rise in those intervals. A noticeable example of this can be seen after 600 years of propagation in the shallow envelope run of Figure 4.3 where γ in interval 'A' is increasing slowly.

The long-duration simulations of Keegan & Downes (2005) found that for velocities over 20 $\mathrm{km\,s^{-1}}$, there were substantial variations of γ, while for velocities below 20 $\mathrm{km\,s^{-1}}$, the γ value became constant. This is in agreement with our results where we find little variation in our slow 'A' and 'B' radial velocity intervals.

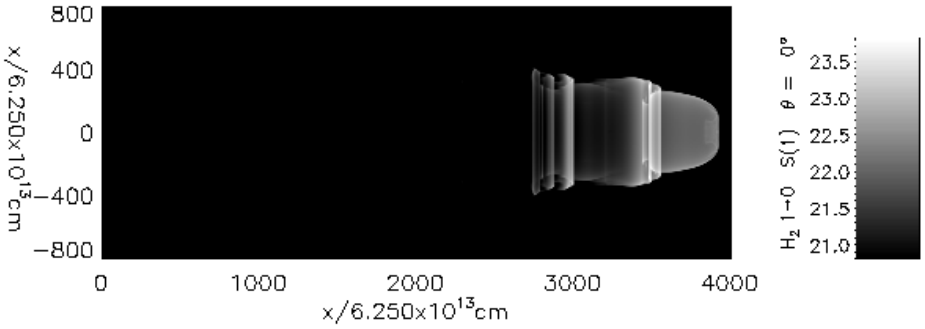

Figure 4.9: H_2 1-0 emission maps displayed in the plane of the sky for the shallow gradient run (Profile 2), Figure 4.3.

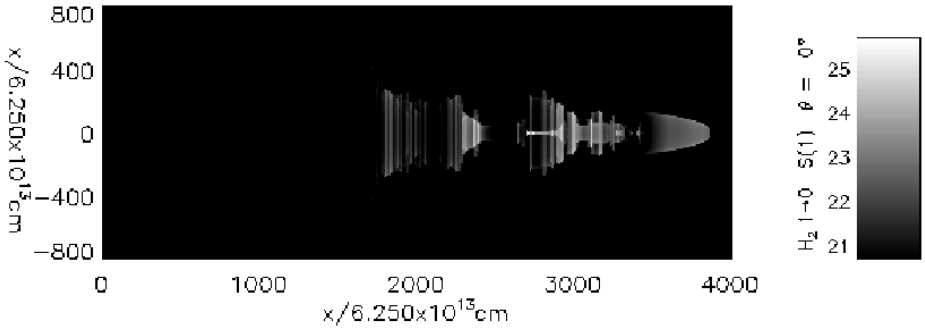

Figure 4.10: H_2 1-0 emission maps displayed in the plane of the sky for the extended-clump run, Figure 4.8.

4.4 H_2 emission

In an attempt to create further links to observations we plotted integrated H_2 1→0 S(1) emission maps of our runs at the end of grid times displayed in the main figures. We present two of the emission maps here in Figures 4.9 and 4.10. The 2.5D axisymmetry approximation leads to the apparent annuli or tube like structures that are visible.

The Profile 2 run is presented in Figure 4.9. All the ambient medium density profile runs were found to create similar smooth emission near the front half of the cocoon surface though the intensity of the flux drops as the profiles become steeper.

Figure 4.10 is the emission map of the extended clump run which will be described in the next section. In the density discontinuity runs, the majority of flux is located at the front bow-shock and through the later two high density shells.

4.5 Propagation through sheets

4.5.1 Flow structure

We may expect that impacts with dense sheets would disrupt the bow shock and cavity sufficiently to alter the mass spectrum. We display three such simulations here, all with sheets fifteen times denser than the ambient medium. The density profiles are again displayed in the seventh panel of the following figures. Although the sheets are 1.5 times the initial jet density, they are somewhat denser than the impinging jets at the point of impact due to jet expansion. Figures 4.6 and 4.7 display flows in which three sheets and one sheet, respectively of thickness 1.25×10^{16} cm cut across the grid. The results of a simulation with three sheets of thickness 3.125×10^{16} cm is displayed in Figure 4.8. Note that the sheets are not pressure confined and the edges of the sheets expand at the sound speed due to a rarefaction wave. In 1,000 years, the wave will propagate 10 zones, as shown.

Prominent effects occur along the flanks of the outflow. Impacts with the clumps lead to temperatures over 200,000 K along the edges. As expected, this leads to strong turbulence, especially notable in the distribution of the molecular fraction. The turbulence entrains the molecular mass which reaches high velocities.

The presence of the clumps clearly pinches or focuses the outflows, suppressing the low density cavity from lateral expansion and forcing material towards the axis as seen by the negative radial velocities (e.g. at the second clump in Figure 4.8). A similar effect was found in the 3D simulations by Cerqueira & de Gouveia Dal Pino (2001) of jets propagating into ambient media of increasing density and pressure. The authors noted that the low-pressure cocoon gets compressed and the leading bow-shock structure gets destroyed.

The clumps have invoked a much more turbulent cavity/ambient medium interface. This has led to a greater amount of molecular material in motion than compared to a

similar uniform ambient medium simulation. However, the increases shown in Table 4.3 are commensurate with the additional mass available on the grid to be accelerated. Nevertheless, the higher *fractions* of H_2 momentum and moving mass result from the expected increase in transfer efficiency of these quantities in flows which are not driven by ballistic (overdense) jets.

The sheets thus produce a significant molecular/total moving mass fraction (0.70 for the Extended Clump run compared to 0.18 for the plateau core (Profile 1)). Furthermore, the majority of the total momentum derives from molecular momentum with significantly higher molecular/total momentum fractions when compared to the 'core' runs (0.3 for the Extended Clump rum compared to 0.03 for the plateau core).

Each of the clump simulations possess different outflow crossing times (displayed on the figures). Surprisingly, the outflow of the extended 3-clump simulation (Extended Clump) crosses the grid faster than in the narrow 3-clump simulation (Multiple Clump). Thus the focussing can be more important than the inertia of the sheets. Despite the Extended Clumps run possessing the greatest grid mass, and both the greatest moving total and H_2 masses, the Multiple Clump run possesses the greatest momentum. This suggests that if clumps are too large they would have a detrimental effect on momentum transfer. The η value (ρ_j/ρ_a) drops accordingly from the initial over-dense 1.5 value. For both the Multiple Clump and Extended Clumps runs, η in the first clump equals 0.66, at the second clump η equals 0.13 and in the third clump η equals 0.04. The jet thus becomes a 'light jet' within the clumps ($\rho_j/\rho_a < 1$).

4.5.2 Mass spectra analysis

Collisions with the sheets lead to large fluctuations in γ. The evolution plots of Figures 4.6, 4.7 and 4.8 show an abrupt increase in the highest velocity γ interval, interval 'D', as the jet impinges on the first clump. Hence, the highest velocity bow-shock material is rapidly decelerated by the high density sheet. This steepening propagates back

to the slower velocity intervals while being damped by the greater quantity of material at the lower velocities (visible in available movies), in a more extreme fashion to the vortex shedding events discussed for the core profile runs.

Comparing the γ vs time plots of Figures 4.6, 4.7 and 4.8 we see that the collision with a single clump is sufficient for a persistent fluctuation of the high velocity component γ profile. The suppression of the high velocity γ component remains in the Multiple Clump run where the front of the jet fails to have sufficient time to reform a stable high velocity bow shock. However, the difference in this case is that the further collisions feed back to the slower velocities intervals and lead to fluctuations in those γ components instead.

Overall, the presence of sheets can lead to higher γ values compared to the core simulation values. The high velocity γ component reaches as high as 6 to 7.5 for the initial collision in the clump runs whereas the core runs do not rise above a γ of 5.

4.6 Velocity profile

The jet beam velocity profile simulation was an attempt to remove the jet beam contribution to the mass-velocity plots. In the previous mass-velocity plots of this chapter, the total-mass (dotted line) resulted in a peak at high radial velocities due to the jet beam material. It was noted that this peak is not usually detected in observational mass-velocity measurements.

Here we set an initial jet beam velocity of 100 km s^{-1} which decreases linearly with time to 0 km s^{-1} by the time the jet had reached the end of the grid. This configuration of a jet beam velocity gradient completely removes the jet beam component from the mass-velocity profile by 'smearing' it out over the entire mass-velocity range. The resulting simulation is presented in Figure 4.11 (Here, due to a computer upgrade, we also performed a higher resolution run of 8,000 $\times$ 1,000 zones). The seventh panel displays the jet beam velocity profile. It shows that the maximum velocity at the jet

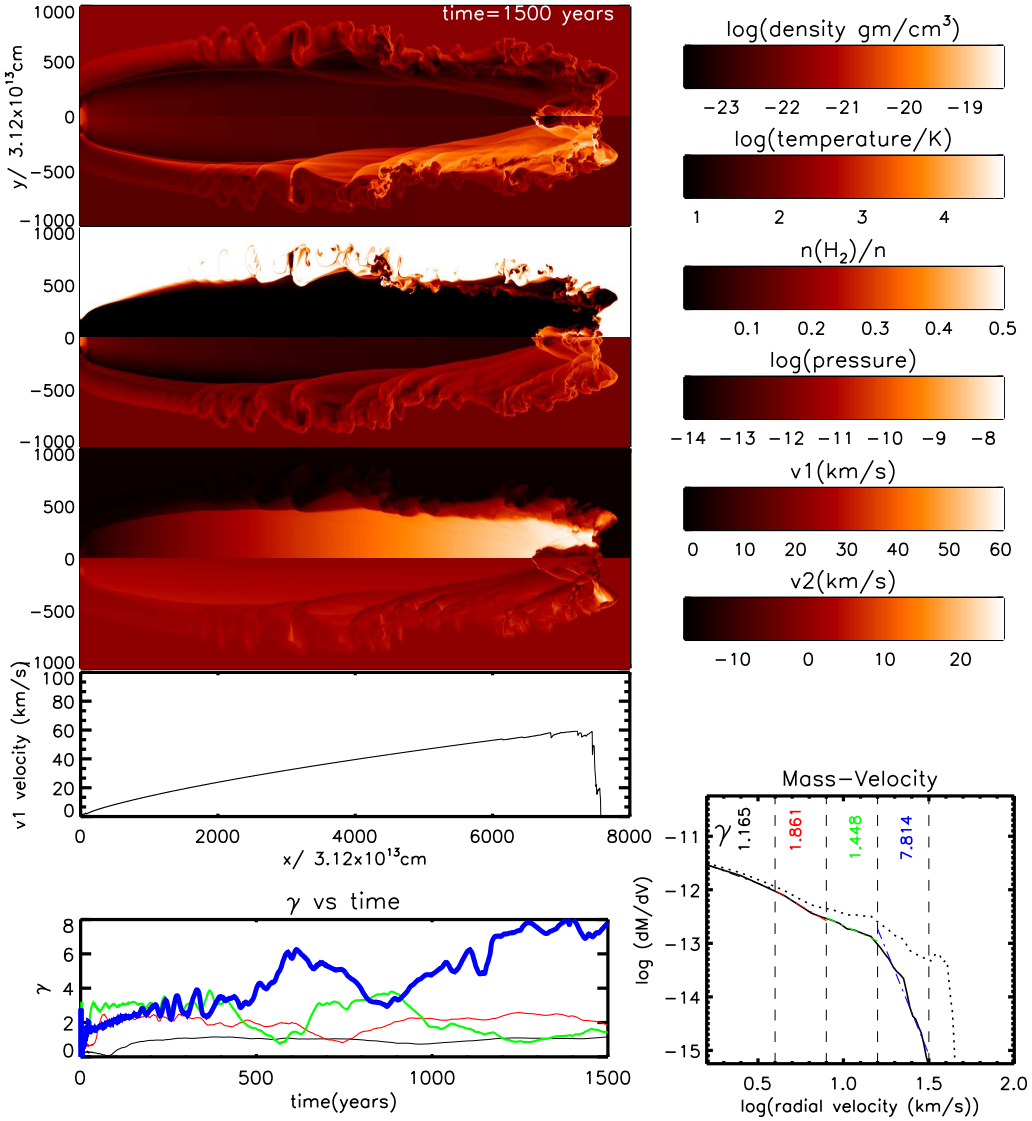

Figure 4.11: The outflow structure of a uniform ambient medium simulation where the jet beam velocity linearly decreases from an initial value of 100 km s^{-1} to 0 km s^{-1}. See Section 4.2 for full figure explanation except for the seventh panel which now shows the velocity profile of the jet beam. Here the resolution was increased to 8,000×1,000 zones.

beam head is 60 km s^{-1} showing that the initial injection of 100 km s^{-1} material has naturally decelerated.

The mass-velocity plot of Figure 4.11 resembles that of the observational example of Figure 2.23 with a breakpoint at the radial velocity of 16 km s^{-1} between a high γ of almost 8 and a low γ of about 1.5.

In reality, such jet beam velocity profiles could be imagined if the ejection rate from the protostar were to decrease with time.

4.7 Conclusions

Information about the cold environments which harbour young stars can be extracted from millimetre observations, employing dust and molecular tracers. However, the young stars drive bipolar outflows which alter the environment and possess distinct observational signatures. These signatures contain information about the interaction with the environment as well as the driving star. Our purpose here has been to use the high resolution afforded by two-dimensional hydrodynamic simulations to explore the interaction.

Protostellar cores have been simulated here as smooth density profiles. With uniform or gradual density decreases, possibly corresponding to the youngest protostars, the outflow structures are narrow with turbulent entrainment of clumps along the flanks. Steeper density profiles, which may correspond to more evolved young stars, are dominated by the leading bow shocks which entrain by ploughing through ambient gas.

The environments may also be pervaded by a pattern of dense filaments or sheets. Outflow maps may be dominated by the locations where the outflow impacts or cuts through sheets, where the majority of the material is accelerated and excited. Here, we have shown that a collimated outflow can become turbulent after passing through a shell.

The mass spectra corresponding to the molecular component vary substantially in time, especially at radial speeds exceeding 15 km s^{-1}. The γ index increases sharply as a jet impinges on a sheet, followed by a gradual return to a shallower spectrum. The index also strongly varies in simulations dominated by the shedding of large vortices.

Our mass spectra provide a link to observationally obtained mass spectra. In general, our γ values lie between 0.8 to 4 with steeper slopes towards the high velocity end, in keeping with observations. We thus find general agreement with published values. The simulations suggest that the preponderance of observed outflows with high γ values is evidence that the jets penetrate highly non-uniform media.

The mass spectra generated by interactions with shells display relatively small differences between molecular mass and total mass profiles. Hence, in flows dominated by transverse interactions, the molecular mass is representative of the total mass. However, in the case of core-type density distributions, there are always large discrepancies between CO-derived line profiles and the underlying total mass distribution. The difference is mainly at speeds in excess of 20 km s^{-1} and is thus related to the leading edge of the bow shock where molecules suffer wholesale dissociation.

The total mass in these outflows (see column 2 of Table 4.3) are many orders of magnitude less than observationally obtained values. One reason is that our simulated outflows are relatively young. Real outflows have dynamical timescales of the order 10^4 to 10^5 years. Scaling our 1,000 year 10^{-5} $M_\odot$ outflows by 100 and doubling for bi-polarity, we still obtain relatively less massive outflows. We have also assumed low jet densities in order to better resolve radiative cooling and molecular chemistry. The densities of jets associated with Class 0 protostars may be 1,000 times higher.

It should also be noted that a strong magnetic pressure in the jet would promote jet expansion, generating wide outflows. The magnetic field in the ambient medium may also cushion the shock waves, leading to significantly less dissociation. Recent axisymmetric MHD jet simulations were performed by de Colle & Raga (2006). These confirmed previous findings that the tension created by a toroidal magnetic field tends to collimate the spine of the jet and produces a nose cone. Considering this morphology, we may expect shallower mass-velocity plots and lower γ values as cavity material is focused close to the high speed jet beam thus leading to an increase in high velocity components combined with less ambient medium entrainment from the bow shock.

Our simulations suggest that observational break points in mass spectra are controlled by large vortex features in the cavity. Sharp break points at low radial velocities do not occur in our simulations. The time evolution plots suggest break points, such as shown in Figure 4.5, are transient features created by large vortex shedding events where a build up of material in the working surface gets expelled into the cocoon. Figure 4.3 shows no noticeable break point.

Figure 4.6 shows a break point at a radial velocity of 25 $\mathrm{km\,s^{-1}}$ where a small velocity peak exists. As we see in animations, this velocity peak will propagate back to the slower mass-velocity intervals with time, effectively dragging the apparent break point back with it.

Sharp break points may indicate that the outflow impacts with ambient clumps, or episodic outflows are generating new large vortices. We may thus predict particularly bright Herbig-Haro objects from such mass spectra. Looking for large differences between high and low velocity γ in studied outflows, we find large differences for NGC2264G and G192.16, both associated with strong shock activity (Shepherd et al., 1998).

We conclude that mass spectra of protostellar outflows cannot be used to derive information about the driving source due to a strong dependence on the ambient medium. Even the total momentum delivered into the ambient molecular medium can vary by an order of magnitude, according to the nature of the interaction which is stronger for higher densities (lighter jets) and more clumpy density distributions, as expected. Steep ambient medium density profiles are extremely inefficient at transferring momentum both compared to a 'clumpy' environment and a uniform one.

The study presented here unites the results of other studies which have focussed on specific simulations. Recent work by Banerjee et al. (2007) of turbulence in molecular clouds has shown, in 2D slab jet simulations, that a transient jet can completely disperse a higher density clump of material through which it moves, thus effectively transferring momentum. Work by Yirak et al. (2008) simulated the interaction of the outflow on

randomly placed small (smaller than the jet diameter) clumps on 2D grids. They found that the small scale clumps can compare to recent observations of Herbig-Haro objects. Carvalho & O'Dea (2002) noted less structure in the cocoon due to lack of turbulence in their declining density atmosphere runs, as we have found in our steep profile runs.

Final conclusions and future work

Conclusions

To summarise, we investigated the phenomenon of protostellar jets and outflows through numerical simulations. We focused upon two complimentary aspects.

The first examined whether the properties of the outflow had a dependence on the properties of the jet. We proceeded by simulating jets of various velocities and compositions. We created mass-velocity plots in order to create a link to observations. Generally, simulated mass-spectra have had difficulty matching the wide range of mass-spectra found from observations. We mostly obtained shallow mass-spectra ($\gamma \sim 1$–2) which were independent of jet velocity, but found steep mass-spectra could be obtained through an atomic-jet/molecular-medium combination.

The second aspect was an investigation into the effects that the ambient environment would impose upon the protostellar jet/outflow. We created realistic protostellar environments consisting of density gradients and density discontinuities. Once again, we plotted and analysed the mass-spectra of the simulations. We found that non-uniform media lead to steeper mass-spectra, in line with those obtained from observations. We also found that the mass-spectrum of an outflow can vary substantially during its dynamical evolution.

Let us return now to the observations presented in Chapter 1, namely, HH1/2 (Figure 1.6) and HH211 (Figure 1.8).

It is reasonable to assume that the significant dissimilarities of the HH1 and HH2 bowshock are due to differing ambient environments on both sides of the central protostar. This shows the importance of the effect of the ambient medium upon the outflow. The disrupted appearance of the HH2 bowshock could resemble the turbulent structure obtained in our density discontinuity runs, such as Figure 4.7 (bearing in mind the limitations of our 2.5D simulations).

The greyscale H_2 1–0 S(1) 2.122μm emission of HH211 in Figure 1.8 shows limb brightening along the outflows bowshocks with some brightening from internal knots. Our H_2 1–0 S(1) emission plot of an ambient density profile run in Figure 4.9 shows the emission is dominated by the terminal bowshock, as with HH211. Figure 4.10 of a density discontinuity run shows emission where a collision with ambient medium density enhancements occurred. Perhaps this is a possibility to explain the existence of the knots of HH211. Overall, it warrants further study.

Future work

Many routes of future study can taken from here.

The work of investigating simulated mass-velocity profiles could be continued and expanded upon by incorporating more physics such as pulsed or periodic jet beams, the addition of MHD, and ultimately, the addition of the third spatial dimension.

Interesting work is currently being performed with magnetically driven laboratory jets on scales of tens of millimeters (e.g. Ciardi et al., 2008). Our density discontinuity simulations would be particularly suitable to be compared directly to laboratory jet simulations where the laboratory jet could collide and tunnel through very thin sheets of material.

For now, two ideas which are currently being pursued will be described below.

Colour-colour diagrams of outflows

Any type of simulation can be performed through the wide range of available input parameters. However, it is important that they have a relevance or link with observations. This can be achieved by applying observational constraints to simulations and/or displaying the simulated data in the form obtained by observations. Besides the previously seen mass-spectra and molecular emission maps, another diagnostic routinely used by observers are colour-colour diagrams.

Colour-colour diagrams are mainly produced for star forming regions in order to determine the evolutionary stages of young stars. The Infrared Array Camera (IRAC) on the Spitzer Space Telescope is particularly suitable for creating colour-colour plots as it provides simultaneous images at four wavelengths, 3.6, 4.5, 5.8 and 8μm. Colour-colour plots can be produced from combinations of these four wavelengths.

If applied to an extended source, such as a protostellar outflow, a cluster of points would appear on the colour-colour plane where regions of the outflow possessing different properties are spread out. Such plots have been created before (e.g. Smith et al. (2006)).

We could extend the work by creating colour-colour plots from our simulated outflows and compare and contrast them with the positions where observational data lies. Already, coding to create synthetic maps from our simulations based on the Spitzer IRAC bands has been written by Smith & Rosen (2005b). Observational data is plentiful. Currently, post-processed IRAC data of at least 19 regions containing outflows are publicly available from the Spitzer Science Center data archive.

The coming years will see a plentiful supply of new data from the next generation of telescopes, building upon the success of Spitzer by specialising in the infrared and sub-millimeter regions of the spectrum to probe the cool dense regions of molecular clouds, outflows, proto- and pre-stellar cores. These telescopes include the European Herschel Space Observatory, which will cover the far-Infrared to sub-millimeter wavelengths and

currently due for launch in 2009. The Atacama Large Millimeter Array (ALMA) due for completion in 2012 will use interferometry to detect sub-millimeter and millimeter wavelengths at high spatial resolutions. The successor to the Hubble Space Telescope, the James Webb Space Telescope (JWST) will be another an infrared space telescope due for launch in 2013. Finally, the proposed European Extremely Large Telescope (E-ELT) is to have near-infrared capability and may be completed by 2017.

The study of the current Spitzer data would enable us to disentangle the features and conditions occurring in real outflows through their positions on a colour-colour diagram with the help of the detail available from fully resolved numerical simulations.

Full-scale self-consistent protostellar jet simulations

Another tempting project would return and focus on the numerical aspect by performing full-scale *self-consistent* jet simulations.

Typically, protostellar jet simulations have come in two forms, either Jet launching simulations or Jet propagation simulations. The jet launching simulations concentrate only on the region close to the accretion disk and a relatively high resolution is required to simulate the complex MHD launching and collimation processes that are necessary to launch a jet. Due to these heavy computational requirements, they typically only cover a region of a few tens of Astronomical Units (AU) around the star. On the other hand, jet propagation simulations (the type in this thesis) assume that the jet has already been launched and collimated and only simulate the propagation of the collimated beam over much larger time and length scales of tens of thousands of AU.

What is required is to link the jet launching and jet propagation simulations together into a single large self-consistent jet simulation. Such complete self-consistent simulations have not been performed before due to computational limitations.

Now, however, the computer power capable of handling such large simulations is be-

coming available. Since the beginning of 2008, the Irish Center for High-End Computing (ICHEC) have added an IBM Blue Gene/L and IBM Blue Gene/P supercomputer to their repertoire. The more powerful IBM Blue Gene/P is the first of this class of powerful supercomputer to be installed in Europe and is capable of performing calculations at a rate of 13.9 Tflops (Previously, ICHEC's most powerful system was their distributed memory 'Walton' cluster with a maximum performance of 4.55 TFlops).

A modern AMR code would be necessary in order to handle the changes of scale from from sub AU zone sizes near the launching point to multiple AU zone sizes downstream in the jet propagation region. The inclusion of MHD and molecular chemistry routines would handle the launching and dynamical evolution of the jet and outflow.

Such full scale simulations would obtain the first complete overall picture protostellar outflows from the launching stage at a few AU out to the terminal bow-shock tens of thousands of AU away. Interesting phenomena and new dynamical physics may arise from the large changes of scale such as jet turbulence switching between laminar and turbulent states and the growth and dissipation of shock waves. It may also be possible to investigate whether the creation of 'knots' from velocity variations and other features are scale dependent or independent and be able to identify different regimes and transitions as a function of initial jet and environmental parameters. The ultimate goal would be to constrain the actual launching mechanism by studying the morphology of the jet and outflow which develops on the larger scales.

To conclude, there has never been a better time for studying star formation and protostellar jets. Technological advancements in the modern telescopes and detectors will be capable of probing deeper and deeper into molecular clouds with unprecedented resolution. The continuing improvements in computers and numerical codes are opening the door to simulations of considerable complexity and realism. It is likely that the next decade will see many great advancements in this field, answering the key mysteries of star formation which astronomers have been slowly piecing together over the last century. For now, hopefully, this thesis has added one more small piece to the puzzle.

Bibliography

Abbett W. P., Fisher G. H., 2003, ApJ, **582**, 475

Agúndez M., Cernicharo J., Guélin M., 2007, ApJ, **662**, L91

Anderson J., 1995, Computational Fluid Dynamics. (John David Anderson: McGraw-Hill International Editions, 1995)

Andre P., Ward-Thompson D., Barsony M., 1993, ApJ, **406**, 122

Arce H. G., Goodman A. A., 2001, ApJ, **551**, L171

Bacciotti F., Ray T. P., Mundt R., Eislöffel J., Solf J., 2002, ApJ, **576**, 222

Bachiller R., 1996, ARA&A, **34**, 111

Bagchi J., Gopal-Krishna Krause M., Joshi S., 2007, ApJ, **670**, L85

Bally J., Heathcote S., Reipurth B., Morse J., Hartigan P., Schwartz R., 2002, AJ, **123**, 2627

Bally J., Lada C. J., 1983, ApJ, **265**, 824

Bally J., Sutherland R. S., Devine D., Johnstone D., 1998, AJ, **116**, 293

Bally J., Testi L., Sargent A., Carlstrom J., 1998, AJ, **116**, 854

Bally J., Walawender J., Luhman K. L., Fazio G., 2006, AJ, **132**, 1923

Banerjee R., Klessen R. S., Fendt C., 2007, ApJ, **668**, 1028

Banerjee R., Pudritz R. E., 2007, ApJ, **660**, 479

Bell M. B., Feldman P. A., Travers M. J., McCarthy M. C., Gottlieb C. A., Thaddeus P., 1997, ApJ, **483**, L61

Bethell T. J., Chepurnov A., Lazarian A., Kim J., 2007, ApJ, **663**, 1055

Biro S., Raga A. C., 1994, ApJ, **434**, 221

Blandford R. D., Payne D. G., 1982, MNRAS, **199**, 883

Blondin J. M., Fryxell B. A., Konigl A., 1990, ApJ, **360**, 370

Bok B. J., Reilly E. F., 1947, ApJ, **105**, 255

Bonnell I. A., Bate M. R., Zinnecker H., 1998, MNRAS, **298**, 93

Calvet N., 2004, in Dupree A. K., Benz A. O., eds, Stars as Suns : Activity, Evolution and Planets Vol. **219** of IAU Symposium, Outflows and Accretion in Young Stellar Objects. p. 599

Canto J., Raga A. C., 1991, ApJ, **372**, 646

Carolan P. B., Redman M. P., Keto E., Rawlings J. M. C., 2008, MNRAS, **383**, 705

Carvalho J. C., O'Dea C. P., 2002, ApJS, **141**, 371

Cerqueira A. H., de Gouveia dal Pino E. M., 1999, ApJ, **510**, 828

Cerqueira A. H., de Gouveia Dal Pino E. M., 2001, ApJ, **560**, 779

Chen H., Myers P. C., Ladd E. F., Wood D. O. S., 1995, ApJ, **445**, 377

Ciardi A., Ampleford D. J., Lebedev S. V., Stehle C., 2008, ApJ, **678**, 968

Clarke D. A., 1996, ApJ, **457**, 291

Coffey D., Bacciotti F., Ray T. P., Eislöffel J., Woitas J., 2007, ApJ, **663**, 350

Coffey D., Bacciotti F., Woitas J., Ray T. P., Eislöffel J., 2004, ApJ, **604**, 758

Cunningham A. J., Frank A., Quillen A. C., Blackman E. G., 2006, ApJ, **653**, 416

Cunningham A. J., Frank A., Varniere P., Mitran S., Jones T. W., 2007, ArXiv e-prints, http://arxiv.org/abs/0710.0424, **710**

Davis C. J., Kumar M. S. N., Sandell G., Froebrich D., Smith M. D., Currie M. J., 2007, MNRAS, **374**, 29

Davis C. J., Smith M. D., Eislöffel J., 2000, MNRAS, **318**, 747

de Colle F., Raga A. C., 2006, A&A, **449**, 1061

de Gouveia Dal Pino E. M., 1999, ApJ, **526**, 862

de Gouveia dal Pino E. M., Benz W., 1993, ApJ, **410**, 686

de Gouveia dal Pino E. M., Birkinshaw M., 1996, ApJ, **471**, 832

Downes T. P., Cabrit S., 2003, A&A, **403**, 135

Downes T. P., Ray T. P., 1999, A&A, **345**, 977

Dwek E., Galliano F., Jones A. P., 2007, ApJ, **662**, 927

Eisner J. A., Carpenter J. M., 2006, ApJ, **641**, 1162

Falle S. A. E. G., 2002, ApJ, **577**, L123

Ferreira J., 2007, in Ferreira J., Dougados C., Whelan E., eds, Lecture Notes in Physics, Berlin Springer Verlag, Vol. **723** of Lecture Notes in Physics, Berlin Springer Verlag,, "MHD Disc Winds". p. 181

Frank A., Ryu D., Jones T. W., Noriega-Crespo A., 1998, ApJ, **494**, L79

Froebrich D., 2005, ApJS, **156**, 169

Garay G., Mardones D., Bronfman L., Brooks K. J., Rodríguez L. F., Güsten R., Nyman L.-Å., Franco-Hernández R., Moran J. M., 2007, A&A, **463**, 217

Gardiner T. A., Frank A., Jones T. W., Ryu D., 2000, ApJ, **530**, 834

Guilloteau S., Dutrey A., Pety J., Gueth F., 2008, A&A, **478**, L31

Gullbring E., Hartmann L., Briceno C., Calvet N., Muzerolle J., 1998, in Donahue R. A., Bookbinder J. A., eds, Cool Stars, Stellar Systems, and the Sun Vol. **154** of Astronomical Society of the Pacific Conference Series, Color Anomalies of Weak Lined T Tauri stars. p. 1709

Hamilton C. M., Johns-Krull C. M., Herbst W., Mundt R., Bailer-Jones C. A. L., 2005, in Protostars and Planets V, "H-Alpha Line Profiles of KH 15D: What Do They Reveal?". p. 8516

Haro G., 1952, ApJ, **115**, 572

Haro G., 1953, ApJ, **117**, 73

Hartmann L., 2001, Accretion Processes in Star Formation. Lee Hartmann, Cambridge University Press, January 2001.

Hayashi C., 1966, ARA&A, **4**, 171

Henyey L. G., Lelevier R., Levée R. D., 1955, PASP, **67**, 154

Herbig G. H., 1950, ApJ, **111**, 11

Herbig G. H., 1951, ApJ, **113**, 697

Herbst W., Eislöffel J., Mundt R., Scholz A., 2007, in Reipurth B., Jewitt D., Keil K., eds, Protostars and Planets V "The Rotation of Young Low-Mass Stars and Brown Dwarfs". pp 297–311

Herbst W., Herbst D. K., Grossman E. J., Weinstein D., 1994, AJ, **108**, 1906

Hester J. J., Stapelfeldt K. R., Scowen P. A., 1998, AJ, **116**, 372

Heyer M. H., Brunt C., 2007, in Elmegreen B. G., Palous J., eds, IAU Symposium Vol. **237** of IAU Symposium, "Turbulence in the molecular interstellar medium". pp 9–16

Hirano N., Liu S.-Y., Shang H., Ho P. T. P., Huang H.-C., Kuan Y.-J., McCaughrean M. J., Zhang Q., 2006, ApJ, **636**, L141

Hollenbach D., McKee C. F., 1989, ApJ, **342**, 306

Hollenbach D. J., Werner M. W., Salpeter E. E., 1971, ApJ, **163**, 165

Hollis J. M., Lovas F. J., Remijan A. J., Jewell P. R., Ilyushin V. V., Kleiner I., 2006, ApJ, **643**, L25

Jiang Z., Tamura M., Hoare M. G., Yao Y., Ishii M., Fang M., Yang J., 2008, ApJ, **673**, L175

Joy A. H., 1945, ApJ, **102**, 168

Keegan R., Downes T. P., 2005, A&A, **437**, 517

Khanzadyan T., Gredel R., Smith M. D., Stanke T., 2004, A&A, **426**, 171

Korycansky D. G., Zahnle K. J., Mac Low M.-M., 2000, Icarus, **146**, 387

Lada C. J., 1987, in Peimbert M., Jugaku J., eds, Star Forming Regions, Vol. **115** of IAU Symposium, "Star formation - From OB associations to protostars". pp 1–17

Lagadec E., Zijlstra A. A., Matsuura M., Menzies J. W., van Loon J. T., Whitelock P. A., 2008, MNRAS, **383**, 399

Larson R. B., 2003, Reports of Progress in Physics, **66**, 1651

Lee C., Mundy L. G., Stone J. M., Ostriker E. C., 2002, ApJ, **576**, 294

Lee C., Stone J. M., Ostriker E. C., Mundy L. G., 2001, ApJ, **557**, 429

Lee C.-F., Ho P. T. P., Palau A., Hirano N., Bourke T. L., Shang H., Zhang Q., 2007, ApJ, **670**, 1188

Lepp S., Shull J. M., 1984, ApJ, **280**, 465

Lim A. J., Raga A. C., Rawlings J. M. C., Williams D. A., 2002, MNRAS, **335**, 817

Mac Low M.-M., Klessen R. S., 2004, Reviews of Modern Physics, **76**, 125

Marcelino N., Cernicharo J., Agúndez M., Roueff E., Gerin M., Martín-Pintado J., Mauersberger R., Thum C., 2007, ApJ, **665**, L127

Marilli E., Frasca A., Alcalá J. M., Catalano S., Covino E., 2005, Memorie della Societa Astronomica Italiana, **76**, 358

Massey P., Waterhouse E., DeGioia-Eastwood K., 2000, AJ, **119**, 2214

Masson C. R., Chernin L. M., 1993, ApJ, **414**, 230

McCaughrean M. J., Rayner J. T., Zinnecker H., 1994, ApJ, **436**, L189

McGroarty F., Ray T. P., Bally J., 2004, A&A, **415**, 189

McKee C. F., Storey J. W. V., Watson D. M., Green S., 1982, ApJ, **259**, 647

Mellema G., Frank A., 1997, MNRAS, **292**, 795

Mignone A., Bodo G., Massaglia S., Matsakos T., Tesileanu O., Zanni C., Ferrari A., 2007, ApJS, **170**, 228

Mitchell G. F., Johnstone D., Moriarty-Schieven G., Fich M., Tothill N. F. H., 2001, ApJ, **556**, 215

Moraghan A., Smith M. D., Rosen A., 2006, MNRAS, **371**, 1448

Myers P. C., Bachiller R., Caselli P., Fuller G. A., Mardones D., Tafalla M., Wilner D. J., 1995, ApJ, **449**, L65+

Nelson R. P., Langer W. D., 1999, ApJ, **524**, 923

Neufeld D. A., Kaufman M. J., 1993, ApJ, **418**, 263

Noriega-Crespo A., Moro-Martin A., Carey S., Morris P. W., Padgett D. L., Latter W. B., Muzerolle J., 2005, in Wilson A., ed., ESA Special Publication Vol. **577** of ESA Special Publication, Spitzer observations and analysis of the Class 0 source IRAS 23011+6126 and its outflow. pp 453–454

Norman M. L., 2000, in Revista Mexicana de Astronomia y Astrofisica Conference Series, "Introducing ZEUS-MP: A 3D, Parallel, Multiphysics Code for Astrophysical Fluid Dynamics". pp 66–71

Norman M. L., Winkler K.-H. A., 1985, "Supersonic jets". Los Alamos: Los Alamos National Laboratory, 1985

Norman M. L., Winkler K.-H. A., Smarr L., Smith M. D., 1982, A&A, **113**, 285

O'Connell B., Smith M. D., Froebrich D., Davis C. J., Eislöffel J., 2005, A&A, **431**, 223

O'Sullivan S., Lery T., 2002, in Henney W. J., Steffen W., Binette L., Raga A., eds, Revista Mexicana de Astronomia y Astrofisica Conference Series MHD Jets in Inhomogeneous Media. pp 98–102

O'Sullivan S., Ray T. P., 2000, A&A, **363**, 355

Palla F., Stahler S. W., 1999, ApJ, **525**, 772

Pavlovski G., 2004, PhD thesis, (Queen's University Of Belfast, N.I), http://www.astro.soton.ac.uk/ gbp/mythesis.html

Pavlovski G., Smith M. D., Mac Low M., Rosen A., 2004, Ap&SS, **292**, 69

Pavlovski G., Smith M. D., Mac Low M.-M., 2006, MNRAS, **368**, 943

Pavlovski G., Smith M. D., Mac Low M.-M., Rosen A., 2002, MNRAS, **337**, 477

Plewa T., 2003, in Turcotte S., Keller S. C., Cavallo R. M., eds, 3D Stellar Evolution Vol. **293** of Astronomical Society of the Pacific Conference Series, "The FLASH code: from design to applications". pp 22–26

Raga A., Cabrit S., 1993, A&A, **278**, 267

Raga A. C., Binette L., Canto J., Calvet N., 1990, ApJ, **364**, 601

Raga A. C., Taylor S. D., Cabrit S., Biro S., 1995, A&A, **296**, 833

Reipurth B., Bally J., 2001, ARA&A, **39**, 403

Reipurth B., Heathcote S., Roth M., Noriega-Crespo A., Raga A. C., 1993, ApJ, **408**, L49

Remijan A. J., Hollis J. M., Snyder L. E., Jewell P. R., Lovas F. J., 2006, ApJ, **643**, L37

Richer J. S., Shepherd D. S., Cabrit S., Bachiller R., Churchwell E., 2000, Protostars and Planets IV, p. 867

Romanova M. M., Kulkarni A., Long M., Lovelace R. V. E., Wick J. V., Ustyugova G. V., Koldoba A. V., 2006, Advances in Space Research, **38**, 2887

Rosen A., Hardee P. E., Clarke D. A., Johnson A., 1999, ApJ, **510**, 136

Rosen A., Smith M. D., 2003, MNRAS, **343**, 181

Rosen A., Smith M. D., 2004a, MNRAS, **347**, 1097

Rosen A., Smith M. D., 2004b, A&A, **413**, 593

Rossi P., Capetti A., Bodo G., Massaglia S., Ferrari A., 2000, A&A, **356**, 73

Schwartz R. D., 1975, ApJ, **195**, 631

Shang H., Allen A., Li Z.-Y., Liu C.-F., Chou M.-Y., Anderson J., 2006, ApJ, **649**, 845

Shapiro P. R., Kang H., 1987, ApJ, **318**, 32

Shepherd D. S., Watson A. M., Sargent A. I., Churchwell E., 1998, ApJ, **507**, 861

Shu F., Najita J., Ostriker E., Wilkin F., Ruden S., Lizano S., 1994, ApJ, **429**, 781

Shu F. H., Lizano S., Ruden S. P., Najita J., 1988, ApJ, **328**, L19

Shu F. H., Ruden S. P., Lada C. J., Lizano S., 1991, ApJ, **370**, L31

Smith H. A., Hora J. L., Marengo M., Pipher J. L., 2006, ApJ, **645**, 1264

Smith M. D., 1986, MNRAS, **223**, 57

Smith M. D., 2000, Irish Astronomical Journal, **27**, 25

Smith M. D., 2003, Ap&SS, **287**, 195

Smith M. D., 2004, "The origin of stars". Michael D. Smith. London (UK): Imperial College Press

Smith M. D., O'Connell B., Davis C. J., 2007, A&A, **466**, 565

Smith M. D., Rosen A., 2003, MNRAS, **339**, 133

Smith M. D., Rosen A., 2005a, MNRAS, **357**, 579

Smith M. D., Rosen A., 2005b, MNRAS, **357**, 1370

Smith M. D., Rosen A., 2007, MNRAS, **378**, 691

Smith M. D., Suttner G., Yorke H. W., 1997, A&A, **323**, 223

Snell R. L., Loren R. B., Plambeck R. L., 1980, ApJ, **239**, L17

Soker N., 2005, A&A, **435**, 125

Soker N., 2007, ArXiv Astrophysics e-prints

Springel V., 2005, MNRAS, **364**, 1105

Stahler S. W., Palla F., 2005, "The Formation of Stars". Steven W. Stahler, Francesco Palla, Wiley-VCH, January 2005.

Stanke T., McCaughrean M. J., Zinnecker H., 2002, A&A, **392**, 239

Stone J. M., 1997, in Reipurth B., Bertout C., eds, Herbig-Haro Flows and the Birth of Stars Vol. **182** of IAU Symposium, "Asymmetric Modes of the Kelvin-Helmholtz Instability in Protostellar Jets". pp 323–333

Stone J. M., Hardee P. E., 2000, ApJ, **540**, 192

Stone J. M., Mihalas D., Norman M. L., 1992, ApJS, **80**, 819

Stone J. M., Norman M. L., 1992a, ApJS, **80**, 753

Stone J. M., Norman M. L., 1992b, ApJS, **80**, 791

Stone J. M., Norman M. L., 1993, ApJ, **413**, 210

Stone J. M., Norman M. L., 1994, ApJ, **420**, 237

Su Y.-N., Zhang Q., Lim J., 2004, ApJ, **604**, 258

Sutherland R. S., Bicknell G. V., 2007, ApJS, **173**, 37

Sutherland R. S., Dopita M. A., 1993, ApJS, **88**, 253

Suttner G., Smith M. D., Yorke H. W., Zinnecker H., 1997, A&A, **318**, 595

Tachihara K., Rengel M., Nakajima Y., Yamaguchi N., André P., Neuhäuser R., Onishi T., Fukui Y., Mizuno A., 2007, ApJ, **659**, 1382

Torbett M. V., 1984, ApJ, **278**, 318

Völker R., Smith M. D., Suttner G., Yorke H. W., 1999, A&A, **343**, 953

van Dishoeck E. F., Glassgold A. E., Guelin M., Jaffe D. T., Neufeld D. A., Tielens A. G. G. M., Walmsley C. M., 1992, in Singh P. D., ed., Astrochemistry of Cosmic Phenomena Vol. **150** of IAU Symposium, "Panel Discussion : the CO/H_2 Abundance Ratio". p. 285

van Leer B., 1977, Journal of Computational Physics, **23**, 276

Wrobel L., Brebbia C., 1991, Computational Modelling of Free and Moving Boundary Problems. (Walter de Gruyter, 1991)

Yamauchi Y., Moore R. L., Suess S. T., Wang H., Sakurai T., 2004, in Sakurai T., Sekii T., eds, The Solar-B Mission and the Forefront of Solar Physics Vol. **325** of Astronomical Society of the Pacific Conference Series, "Macrospicules, Coronal Heating, and SolarB". p. 301

Yirak K., Frank A., Cunningham A., Mitran S., 2008, ApJ, **672**, 996

Yu K., Billawala Y., Smith M. D., Bally J., Butner H. M., 2000, AJ, **120**, 1974

Zanni C., Ferrari A., Rosner R., Bodo G., Massaglia S., 2007, A&A, **469**, 811